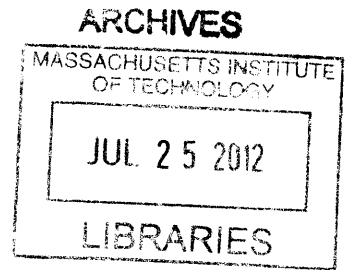# Nanoengineered Surfaces for Improvements in Energy Systems: Application to Concentrated Solar and Geothermal Power Plants

by

Alexander W. Rehn

B.S., Nuclear, Plasma, and Radiological Engineering
University of Illinois at Urbana-Champaign, 2010

Submitted to the Department of Nuclear Science and Engineering
in Partial Fulfillment of the Requirements for the Degree

of

Master of Science in Nuclear Science and Engineering

at the

Massachusetts Institute of Technology

June 2012

Signature of Author _____
Alexander W. Rehn
Department of Nuclear Science and Engineering
June 8, 2012

Approved by _____
Thomas J. McKrell, Ph.D.
Research Scientist, Department of Nuclear Science and Engineering
Thesis Supervisor

Approved by _____
Jacopo Buongiorno, Ph.D.
Associate Professor, Department of Nuclear Science and Engineering
Thesis Reader

Accepted by _____
Mujid Kazimi, Ph.D.
TEPCO Professor of Nuclear Engineering
Chairman, Department Committee on Graduate Theses

Nanoengineered Surfaces for Improvements in Energy Systems: Application to Concentrated Solar and Geothermal Power Plants

by

Alexander W. Rehn

Abstract

The main drawback to renewable energy systems is the higher cost of production compared to competitors such as fossil fuels. Thus, there is a need to increase the efficiency of renewable energy systems in an effort to make them more cost competitive. In this study, the use of nanosurfaces is evaluated for its benefits in improving the efficiency of a concentrated solar tower power system by increasing the energy retained by the receiver surface, and for reducing the fouling on geothermal heat exchangers. The samples tested for the solar receiver application were Inconel 617, Inconel 617 with a 150 nm layer of platinum, Inconel 617 with a 150 nm layer of platinum and a 550 nm layer of nickel oxide, oxidized nickel, and silicon carbide. The experimental results indicated that the platinum was an ineffective diffusion barrier, nickel oxide displays solar selective properties, and silicon carbide would be the best choice for a surface among the samples tested. This indicates that at the operating temperatures for this receiver at 700 °C, a black body surface is more effective than a practical solar selective surface. The nanosurfaces tested for the antifouling application in geothermal systems were subjected to chemistry conditions similar to that in a Dry Cooling Tower at a geothermal plant in Larderello, Italy. Each sample's performance was measured by determining each samples weight change and surface characterization after exposure in an experimental loop. The best performing coatings, all of which showed negligible weight gain, were the Curran 1000 coating from Curran International, the Curran 1000 coating with nanographene, and the Curralon coating with PTFE. Upon further analysis, the Curran 1000 with nanographene was identified as the most promising coating option.

Table of Contents

List of Figures and Tables

1. Introduction

One of the greatest challenges society currently faces is identifying and implementing solutions to the energy crisis that is developing across the world. Energy consumption per capita has steadily risen over the last half century while the world population has continued to skyrocket reaching over 7 billion people in 2011. Meanwhile, concerns have risen about the environmental impacts of burning fossil fuels which have produced the overwhelming majority of energy used in the last century. Therefore, society is faced with the task of producing more energy than has ever been produced before while diminishing use of the main energy sources of the past. Thus, there has been a renewed interest in alternative energy sources including nuclear, hydro, wind, solar, and geothermal energy. Nuclear energy currently produces about 13.5% of the world's electricity consumption according to the Nuclear Energy Institute, but even as a group renewable energy (all alternative energy sources except nuclear) is not a significant fraction of the market.

The events at the Fukushima Daiichi Nuclear Power Plant in Japan in March of 2011 have also exasperated the growth of this energy crisis. Nuclear energy was identified as one of the potential options to combat energy growth while limiting environmental impacts because of its ability to produce large quantities of base load power without emitting carbon dioxide. However, the events at Fukushima has raised concerns about the safety of nuclear energy, and caused Germany to announce they are pressing forward with renewable energy rather than nuclear energy while the future of nuclear energy in Japan is unclear. The uncertainty in their energy futures highlights the battle that has been growing between nuclear energy and renewable energy for the last few decades. To reduce the consumption of fossil fuels, nuclear and renewable energy production must be utilized to supplement the loss of production. Nuclear energy has been demonstrated by countries such as France to be able to provide for the energy demands of a large industrial nation. However, renewable energy has yet to demonstrate the same capability. Thus, the uncertainty in the energy futures of two of the most industrious nations in the world stresses the importance of developing renewable energy technology.

The development of renewable energy into a viable energy alternative for society requires considerable development in a few key areas. Most notably, the cost effectiveness of renewable

energy systems must be improved to provide energy at prices similar to those of other alternatives. Currently, renewable energy costs 3 to 10 times more than its competitors (depending on the energy system) which makes it unviable for society. For renewable energy to become a major part of the market, utilities must select a renewable energy system for production of electricity over other alternatives, and this will not occur while these systems produce expensive electricity. Similar improvements are necessary to increase the total energy renewable energy is capable of producing. It is not yet clear whether renewable energy can be scaled up in production the way fossil fuels or nuclear energy can be. The dependence on factors out of human control such as wind, sunlight, or tides makes renewable energy unreliable and incapable of providing base line energy for society. A society completely reliant on renewable energy will require massive energy storage capability that current technology is not able to provide. However, without energy storage technology renewable energy still has the potential to be part of the solution by providing supplemental energy to another base line energy source. These are the challenges renewable energy faces, but there are also many areas for improvement and with development it is possible renewable energy will grow into a major energy source.

One source of improvement for renewable energy systems involves the incorporation of modern advances in technology such as nanotechnology into their design and operation. These improvements can either increase the amount of energy produced by these systems or reduce the cost of the system. In the case of nanotechnology, the application of nanosurfaces can potentially increase the efficiency of the plants thus increasing the total energy produced by the system. Nanotechnology refers to the development and design of structures that are less than 100 nanometers in size. In the case of nanosurfaces, the surfaces of a material have structures with dimensions on the nanoscale or contain nanoparticles. The goal is to design these nanosurfaces to provide a beneficial property to the surface that could otherwise not be achieved.

Two examples of the application of nanosurfaces to renewable energy systems are the use of a nanosurface on a solar thermal receiver to increase the energy absorption and minimize energy losses in a solar power tower system, and the application of a nanosurface on a heat exchanger in a geothermal plant to reduce the fouling from contaminants in the water. One of the developing

plant designs in solar energy systems is the solar power tower plant design which uses a field of mirrors to direct concentrated sunlight onto a receiver which is a metal surface. The receiver is cooled using a fluid that runs a thermodynamic cycle to produce power. The advantage of this plant design is that the fluid can be raised to higher temperatures which allows for increases in thermodynamic efficiencies. This requires that the receiver operate at an extremely high temperature, typically above 700 °C, at which point energy losses due to radiation become substantial. Therefore, the application of a nanosurface to the receiver surface that will retain a high energy absorptance while limiting the emissive energy losses have been investigate here.

A major challenge in operating a geothermal power plant is the fouling of heat exchangers due to the contaminants in the geothermal water used. Geothermal plants utilize the heated water deep within the ground to produce steam for the turbine, but the extraction of this water involves the extraction of some of the ground as well. As the water moves through the plant the containments in the water slowly corrode the pipes and heat exchangers which leads to the deposition of the contaminants on the pipes due to the chemistry in the system. For heat exchangers, this is referred to as fouling, and it drastically reduces the capacity of the heat exchanger which significantly reduces its efficiency. It is common practice for geothermal plants to shut down for maintenance on these heat exchangers where high pressure water is used to clean the deposition off in a process known as water lancing. This process results in both lost energy production and increased cost for operation for the plant. Thus, the application of a nanosurface to the heat exchanger surface to reduce the deposition on and fouling of the heat exchangers in a geothermal power plant will be investigated.

The topics investigated in this study are tailored for specific renewable energy systems, but are also relevant and applicable to nuclear energy systems. The future nuclear reactor designs utilizing high temperatures will require the management of radiative heat transfer to and from materials to regulate material temperature which could be an application for the nanosurfaces investigated for the solar receiver. The antifouling potential of nanosurfaces on heat exchangers could also be applied at a nuclear power plant to enhance safety and reliability.

2. Background

A basis for the type of technology and underlying physical principles involved must be established before a reasonable approach to the problems can be detailed and solutions formulated. This section outlines the mechanics of the electrical generating systems to which the nanosurfaces will be applied, and the physics behind which the nanosurfaces will operate and ultimately be judged by. The specific operating constraints to which the nanosurfaces must adhere will also be established.

2.1 Solar Energy

Solar energy is the most abundant form of energy that is accessible on the earth. Life would never have been able to grow on earth without such an abundant form of energy. For the most part, solar energy is easily accessible as seen by the vast amount of plant life on earth. However, the needs of the modern world require energy in the form of electricity, and solar energy does not convert easily into electricity. The energy in the solar spectrum, which can be seen in Figure 1 (ASTM Int'l), is not very concentrated but it is quite abundant in its supply. Therefore, some solar energy generating stations concentrate solar energy to produce a reasonable amount of electricity.
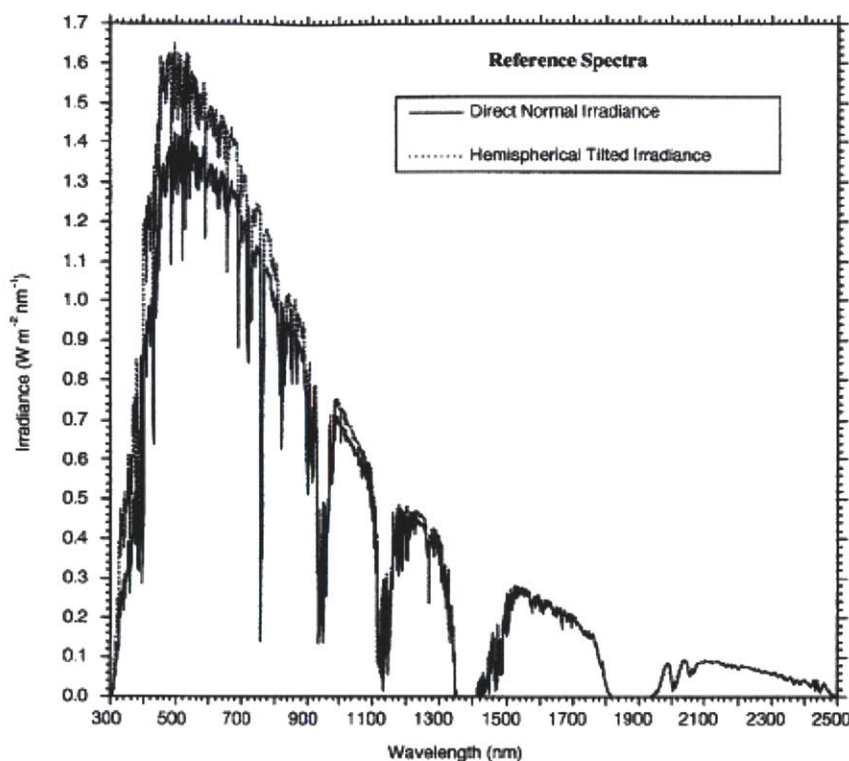
Figure 1- Plot of Direct Normal Spectral Irradiance (Solid Line) and Hemispherical Spectral Irradiance on 37° Tilted Sun-Facing Surface (Dotted Line) (ASTM Int'l).

2.1.1 History

The sun is the most abundant energy source in the solar system and people have been harnessing this energy for thousands of years. The methods by which this was done were originally simple but have become more elaborate through the course of history. The first record of substantial solar energy use was around 200 B.C.E. when Archimedes, a Greek physicist, and Diocles, a Greek mathematician, used mirrors to concentrate the sun's energy on attacking ships to set them on fire (Tabak). For over 2 millennia afterwards optics were studied for their ability to manipulate sunlight with lenses and mirrors for various applications. It wasn't until the 19th century when the steam engine was in widespread use and the Industrial Revolution had changed the world that there was a significant advance in solar technology. A solar powered steam engine was invented by Augustin Mouchot because he believed coal to be a scarce resource that would quickly disappear (Tabak). This inspired the invention of other devices such as solar powered pumps and seemed to have brought about a new age of solar technology, but this trend ended quickly in the early 20th century. World War I demonstrated coal as the superior energy source of

the time, and inventions utilizing alternative power sources were unable to compete. Thus, the use of solar energy for industrial applications ended, but the interest in solar energy as an electricity generation source was just beginning.

The modern age of solar energy began with Edmund Becquerel who published in 1838 the concept of using materials to transform sunlight into energy, but it took until the 20th century for the concept to become developed enough for attempted production. The early 1900's saw the rise and fall of many companies attempting to market solar technologies, but few found success even after Albert Einstein's Nobel Prize winning research on the Photoelectric Effect (Tabak). It took until the discovery of silicon's use as a semiconductor by Bell Laboratories in 1954 and the creation of photovoltaic solar panels to jumpstart the industry (Facts about Solar Energy). During the 1950's and 1960's there was a tremendous amount of research on solar energy due to both its energy and space applications. Both American and Soviet satellites on the late 50's and 60's were powered by photovoltaic technology because it was the only plausible long term energy source for space applications. The advancement of solar energy technology also took a big leap forward in the 1960's and 70's due to concerns about the stability of the oil energy sector in the middle east which culminated with the 1973 oil embargo. However, this did not instigate the advancement of photovoltaic technology, but rather began the interest in solar thermal technology systems (Tabak). During the 1990's there was a small reduction in the progress of solar energy because the demand for the space applications was falling, and the energy crisis had passed. However, a renewed interest in solar energy occurred in the 2000's and has carried through to the present due to the continued instability in the oil energy market and the threat of global warming.

2.1.2 Current Technologies

At this point in history, the major demands of society involve energy in the form of electricity. Solar power has the potential to supply a significant portion of this demand, but it currently lacks the cost competitiveness with fossil fuel to make it a viable alternative energy source. In 2004, the cost of solar energy was $0.25 to $0.30 per kilowatt-hour while energy from fossil fuels was running closer to $0.05 (Lewis). Therefore, there have been strides taken to reduce the cost of

solar electricity production which has involved the advancement of solar energy generating stations. There are solar technologies designed to operate at a single residence, but energy is more cost effective when produced in large quantities at one location. Therefore, this will be an analysis of the current state of solar plant technologies which can be separated into two categories, photovoltaic and concentrated solar power (CSP) technologies.

Photovoltaic solar energy systems operate by use of a solar panel, typically composed of silicon, that produces an electrical current via the photoelectric effect. This technology is considered the more traditional solar energy technology because of its widespread uses. The solar panels do not necessarily have to be used in a plant setting, but can be installed anywhere from a roof, to a calculator, or potentially to a car. The major disadvantage is that there is no potential for storing energy which means the power supply disappears once the sunlight is gone. Therefore, the production of power relies on factors that cannot be controlled. Another drawback is that solar panels do not draw power from the entire solar spectrum which leads to drastic inefficiencies compared to CSP. Currently, the best solar panel efficiency is around 43.5% (Wesoff), and the current research with photovoltaic systems is to increase that efficiency.

Concentrated solar power plants are designed to concentrate the sun's energy to run a thermodynamic cycle. The main difference between the different designs involves the receivers chosen to accept the thermal energy and transfer it to the thermodynamic fluid. While there are a few offshoots, the two most common CSP plants are the parabolic trough and solar tower. Parabolic trough is the most common design for CSP plants, and uses fields of parabolic mirrors with a pipe running through the focus of the mirrors. This design heats a fluid that runs through the pipe and runs on a conventional thermodynamic system. Most parabolic trough receiver pipes operate at 500 °C or less. This design requires that the pipes be thin to allow the fluid to heat efficiently, but this can cause the pipes to become clogged easily. Spain is currently the leader in solar energy production, and their fleet of parabolic trough power stations has a capacity of approximately 600 megawatts (MW). The United States has a few parabolic trough power stations located in the southwest region of the country including the Solar Energy Generating Systems plant (354 MW) in the Mojave Desert, and the Nevada Solar One plant (64

MW) in Boulder City, Nevada.

The solar tower design of a CSP plant involves a field of mirrors all oriented to aim light at a receiver on the top of a tower. The receiver is heated to high temperatures and is then cooled by a fluid which runs a thermodynamic cycle. The thermal receiver in the solar tower design can reach temperatures of up to 900 °C or 1000 °C. Due to the higher receiver operating temperature, the

Figure 2-Sierra Sun Tower (Schell).

thermodynamic fluid reaches a higher temperature which results in greater efficiencies in the thermodynamic cycles, and creates the potential for energy storage (Alexopoulos and Hoffschmidt). Spain has a few operating solar towers, most notably the PS10 and PS20 solar power towers in Seville that produce 10 MW and 20 MW, respectively. The Sierra SunTower operated in Lancaster, California, is the only solar tower in North America, and produces 5 MW. Solar towers are currently limited in number due to the large initial capital investment required to build them, but there are several aspects of the design that are being examined to determine if costs can be lowered. For example, one of the largest expenses in the system is the field of mirrors, known as heliostats, that direct the sunlight to the receiver. These heliostats are typically large, but eSolar is experimenting with using many small heliostats to reduce both the initial and operating costs (Schell). Each heliostat tracks the sun individually and adjusts to direct the sunlight to the solar receiver. This concept was originally conceived in 1862 by Léon Foucault, but has only recently been successful because of the advances in computer technology that allow for cheap computation of each heliostat's motion (Madrigal). The thermodynamic cycle is another area for potential improvements, and specifically with the application of liquid metals as the coolant for the receiver (Angelino and Invernizzi). Finally, there has been a significant amount of research into the design of the receiver, specifically the materials and geometry (Jarvinen).

2.1.3 Design Criteria: Solar Receiver

The focus of this project is to increase the efficiency of a concentrated solar tower power system by increasing the energy retained by the receiver surface. Specifically, the objective is to maximize solar absorption and minimize radiant losses via engineering of the receiver surface. Therefore, the design of the plant and expected operating conditions has already been determined by ENEL in their plant design, and this study will focus exclusively on determining an advantageous surface for this receiver. Table 1 summarizes the relevant design criteria of the receiver surface.

Operating Temperature Range	700-1000°C
Thermal Power	450-500 kW
Area	1.375 m^2
Shape	Ellipsoid
Material	Inconel 617

Table 1-Relevant design criteria for the receiver surface.

2.2 Radiative Heat Transfer

The principles of radiative heat transfer are essential to the understanding of the physics of the system in question, and certain definitions must be established in order to determine the effectiveness of the surfaces tested. The power source to drive this solar power tower is the sun's radiation that is being concentrated on the receiver surface, and the primary means of energy loss to the environment is the radiation that is being produced by the receiver itself. This section will establish the fundamental principles behind radiative heat transfer, and the definitions that will be used in this analysis.

2.2.1 General Mechanisms

Radiative heat transfer is the emission of energy from a body due to the oscillations and transitions of electrons within the body which is directly linked to the body's temperature (Incropera, DeWitt and Bergman). It is a unique form of heat transfer because it does not require physical contact which allows for heat transfer through a vacuum. Therefore, radiative heat

transfer occurs in all matter at all times with the exception of systems at 0 °K. However, the magnitude of radiative heat transfer is extremely dependent on the temperature difference in the system as demonstrated by the following equation (Incropera, DeWitt and Bergman).

$$q''_{rad} = \varepsilon\sigma(T_s^4 - T_{sur}^4)$$

$$\sigma = 5.67 * 10^{-8}\frac{W}{m^2 {}^\circ C}$$

At high temperature deviations between the surface temperature (T_s) and the surrounding temperature (T_{sur}) there is an enormous potential for heat transfer due to the power of four relationship between the two. However, due to the magnitude of the Stefan-Boltzmann constant (σ), radiative heat transfer will be minimal while there are small temperature deviations. For the application to a solar thermal receiver, the temperatures of the surface and surroundings are set which means that the emissivity (ε) (Section 2.2.3) must be decreased to decrease the radiative heat transfer in the receiver.

When considering radiative heat transfer from a surface, it is essentially an analysis of the radiation entering and leaving the surface which is referred to as the irradiation (G) and radiosity (J). The spectral irradiation is described by the following equation.

$$G_\lambda(\lambda) = \int_0^{2\pi}\int_0^{\frac{\pi}{2}} I_{\lambda,i}(\lambda, \theta, \phi)cos\theta\ sin\theta\ d\theta\ d\phi$$

In the equation above and similar equations λ is the wavelength of the light, θ is the polar angle, and ϕ is the azimuth angle. To obtain the total irradiation on the surface, the equation above can be integrated over the entire wavelength spectrum. The spectral irradiance for this project is a multiple of the plot in Figure 1 of the solar spectrum.

The radiosity (J) of a surface is made up of the emitted energy from the surface and the reflected energy from the irradiation as represented by the following equation.

$$J_\lambda(\lambda) = \int_0^{2\pi} \int_0^{\frac{\pi}{2}} I_{\lambda,e+r}(\lambda, \theta, \phi) \cos\theta \, \sin\theta \, d\theta \, d\phi$$

Similar to the irradiation, the total radiosity can be calculated by integrating over the wavelength spectrum. In this case, the radiosity will be almost exclusively the emissivity due to the high absorptivity which keeps the reflectivity low; spectral emissivity equals absorptivity via Kirchhoff's Law (Section 2.2.7).

2.2.2 Absorptivity/Reflectivity/Transmissivity

There are three different interactions that can occur when a photon is incident on a surface. The photon can be reflected by the surface resulting in only a change in the direction of the photon. It can also be absorbed by the surface resulting in the termination of the photon and a deposition of its energy into the material. Lastly, it can be transmitted through the surface resulting in no energetic interaction between the surface and the photon. Given these interactions and the goal of creating a solar thermal receiver, a surface must be selected that maximizes the number of absorbed photons to allow for a large amount of energy to be deposited into the surface.

The intensity of the absorbed, reflected, and transmitted radiation will equal the intensity of the incident irradiation. This concept can be represented by the following equation.

$$\alpha + \rho + \tau = 1$$

The absorptivity (α), reflectivity (ρ), and transmissivity (τ) are the absorbed energy divided by the incident energy, the reflected energy divided by the incident energy, and the transmitted energy divided by the incident energy, respectively, as seen in the equation below (Incropera, DeWitt and Bergman). For the applications in this project, the thickness of the surface layers may be thin enough to allow radiation to transmit to the sub-layers. Therefore, any sub-layers in the coating will have an influence on the performance on the surface. However, the receiver itself is easily thick enough to not allow any transmitted radiation which allows for the assumption that the absorptivity plus the reflectivity is equal to one.

$$\alpha_\lambda(\lambda) = \frac{G_{\lambda,abs}(\lambda)}{G_\lambda(\lambda)}$$

Along with the terms absorptivity, reflectivity, and transmissivity, the terms absorptance, reflectance, and transmittance will be used to describe the performance of the surfaces. The absorptivity is the fraction of the incident energy that is absorbed while the absorptance is the total amount of energy absorbed. The difference is that the absorptivity is a property of the surface while the absorptance is dependent on the system and the amount of incident energy. Reflectance and transmittance have analogous meanings with reflectivity and transmissivity.

2.2.3 Emissivity

The emissivity of a surface is an extremely important quantity for this project because of the high operating temperature. Emissivity defines the ability of the surface to emit radiation. Emissivity and emittance have a similar relationship to that of absorptivity and absorptance which makes emittance the total amount of energy that is emitted by the surface. For the purposes of this project, it is advantageous to have a low emittance surface to allow the receiver to retain the energy rather than release it back to the environment.

$$\varepsilon_\lambda(\lambda, T) = \frac{E_\lambda(\lambda, T)}{E_{\lambda,bb}(\lambda, T)}$$

The value of a surface's emissivity has no bearing on the incident energy, but rather defines the ratio of the surface's emittance to that of a black body at the same temperature as seen by the equation above (Incropera, DeWitt and Bergman). Since a black body is a perfect emitter it is convenient to use it as a standard reference for emittance. The emissive power of a black body follows the Planck Distribution (Section 2.2.5) which can be multiplied by the spectral emissivity of a surface to determine the emission spectrum for the surface.

2.2.4 Types of Surfaces

In the study of radiative heat transfer there are several types of surfaces that are defined to quickly establish the properties of the surfaces in the system. This is important because different

surfaces interact differently with incoming radiation, and defining surface types allows for a quick understanding of the general trends of the surface.

2.2.4.1 Black Body

The most important surface, or theoretical surface, in the study of radiative heat transfer is a black body surface. A black body surface is a perfect absorber and emitter. It will absorb any radiation that interacts on its surface, and will emit the maximum possible radiation at its temperature. The following equation is valid for a black body across all wavelengths.

$$\alpha_{bb} = \varepsilon_{bb} = 1$$

Therefore, it is impossible for any other surface to absorb or emit more energy than a black body surface. A perfect black body is a theoretical surface, but there are many real surfaces that are very good black body imitators. The concept of a black body allows for a standard to be set by which emissivity values for real surfaces can be measured. The emissivity of a surface will always be a value between 0 and 1 because it describes the emissivity in relation to that of a black body. Since the emissive power of a black body can be described by the Planck Distribution, the emissive power of any surface can be calculated by multiplying the Planck Distribution by the surface's spectral emissivity.

2.2.4.2 Selective Surface

A selective surface is a surface that has a significant variation in its absorptivity and emissivity over its wavelength spectrum. This is important because Kirchhoff's Law (Section 2.2.7) states that the absorptivity and emissivity must be equal at each individual wavelength, but not necessary the same value across the wavelength spectrum. In the context of a solar receiver application, a selective surface would have a high absorptivity and emissivity over the wavelengths on the solar spectrum, and a low absorptivity and emissivity over the wavelengths of the Planck Distribution where it would be emitting energy.

Example of a Selective Surface
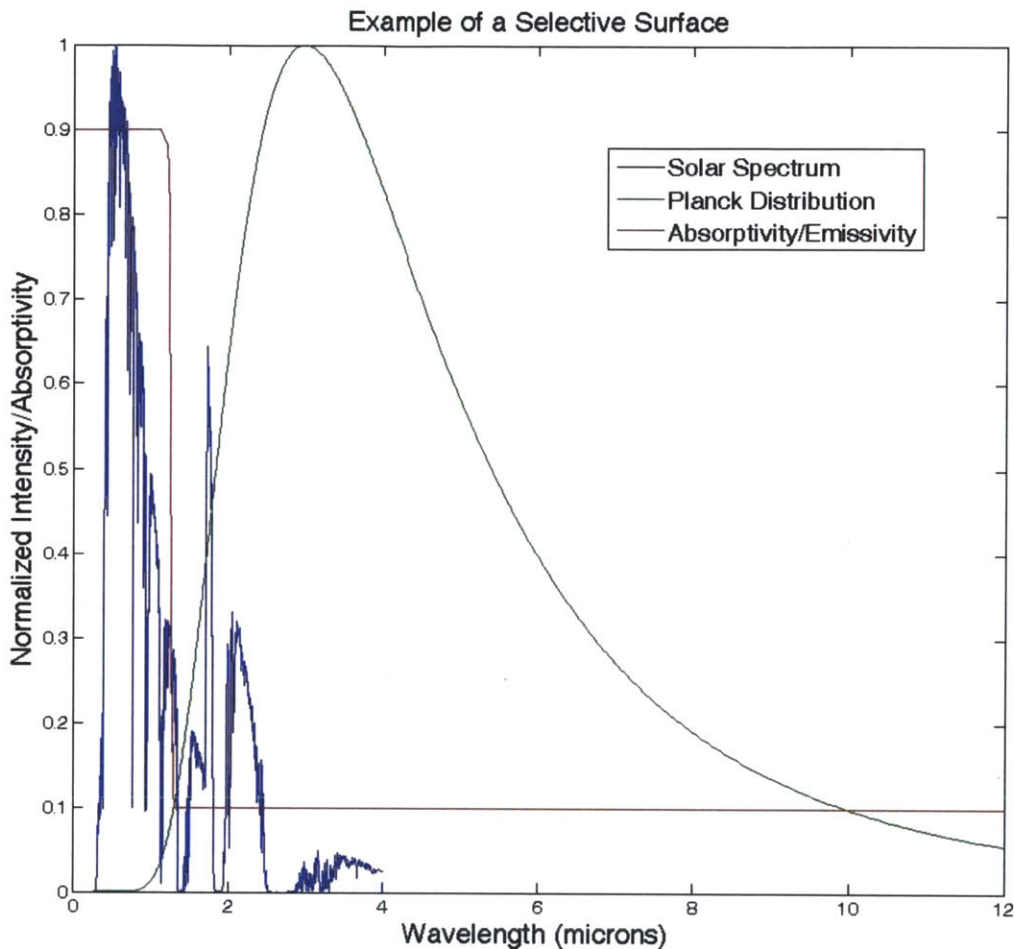
Figure 3-Example of the spectral absorptivity of a solar selective surface with the normalized solar spectrum and Planck Distribution at 973 K.

This concept can be summarized by the graph in Figure 3. The graph in this figure displays the normalized solar spectrum, normalized Planck Distribution at 973 °K, and the absorptivity/emissivity values of a theoretical selective surface at each wavelength. In the region of the solar spectrum it is important for the surface to have a high absorptivity to absorb the incoming radiation efficiently. However, in the region of the Planck Distribution it is important to have a low emissivity in order to efficiently retain the energy in the receiver. The optimal transition region for a solar selective surface is about 1.2 microns because at this point over 80% of the solar spectrum is covered with high absorptivities while the entire Planck Distribution is in the low emissivity region. Real selective surfaces require a much larger absorptivity/emissivity

transition period than the one displayed in Figure 3. A smaller transition period results in a better selective surface as well as increased absorptivity across the solar spectrum and lower emissivity across the Planck Distribution.

2.2.5 Planck Distribution

The emissive power of a black body is extremely important because it is the standard by which the emissivity of all other surfaces is quantified. Due to its importance, Planck determined an equation that represents the spectral emissivity of a blackbody at any temperature. It is called the Planck Distribution, and it is given below (Incropera, DeWitt and Bergman).

$$E_{\lambda,bb}(\lambda, T) = \frac{2\pi h c_0^2}{\lambda^5 \left[exp^{\frac{hc_0}{k\lambda T}} - 1 \right]}$$

$$h = 6.626 * 10^{-34} J * s$$

$$k = 1.381 * 10^{-23} J/K$$

$$c_0 = 2.998 * 10^8 m/s$$
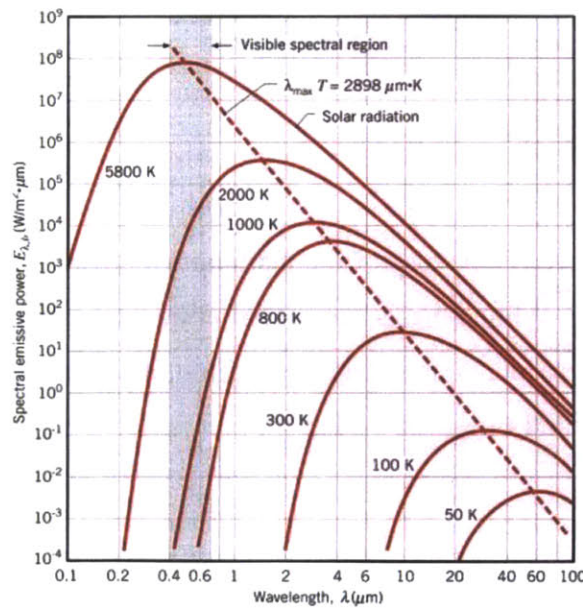
Figure 4-Planck Distribution at a variety of different temperatures (Incropera, DeWitt and Bergman).

Figure 4 displays the Planck Distribution at a variety of temperatures, and certain key factors should be noted about the trends. Firstly, with increasing temperature the emissive power increases across every wavelength resulting in a significantly larger emittance at high temperatures. This is the cause of the exponent relationship (T^4) between temperature and radiative heat transfer. Secondly, the spectrum shifts toward shorter wavelengths as the temperature increases which results in the emission in the visible wavelengths. This is demonstrated by solids glowing when they reach high temperatures.

2.2.6 Wien's Law

As can be seen by Figure 4, the peak of the Planck Distribution is continually shifting toward shorter wavelengths. This peak can be calculated by using Wien's Displacement Law which is given below.

$$\lambda_{max} = \frac{2898 \, \mu m \, K}{T}$$

The sun is essentially a black body operating at 5800 K, and following the equation above that puts the maximum intensity of the spectrum at 0.5 μm which explains why so much visible light is produced by the sun (Incropera, DeWitt and Bergman).

2.2.7 Kirchhoff's Law

Thus far, it has been established that a solar thermal receiver should have a high solar absorptivity and a low radiative emissivity for the maximum amount of energy to be inserted into the thermodynamic system. While this is simple in principle, it becomes challenging when considering Kirchhoff's Law which states that the spectral, angular absorptivity and emissivity are equal (Incropera, DeWitt and Bergman). This concept is stated more plainly by the following equation.

$$\alpha_{\lambda,\theta} = \varepsilon_{\lambda,\theta}$$

Since these quantities are linked, it is necessary to find surfaces that drastically change their

properties at different wavelengths. Thus, a selective surface is advantageous.

2.3 Geothermal Energy

Deep within the earth there is a large amount of energy stored in the rock, and in some regions this energy is close enough to the surface for extraction. The water present in the ground around these regions of hot rock absorbs some of this energy, and this water can be extracted. A supply of heated water from the earth is referred to as a geothermal resource. To create geothermal energy, the energy is extracted from the geothermal resource to produced steam to create electricity, and the water is then reinserted back into the ground so it can be reheated by the rock. Depending on the rate of energy extraction it is possible for geothermal energy to be a renewable or non-renewable energy source, but it is typically viewed as a renewable energy source because energy from the rock is extracted slowly enough that the rock reheats from the energy deeper within the earth. Geothermal energy is a promising renewable energy technology because it can produce a steady supply of energy since it doesn't rely on an inconsistent power source (unlike wind and solar), but it is available in limited regions that nature has provided with accessible geothermal resources.

2.3.1 History

Geothermal resources have a broad range of potential applications and have been harnessed for these applications for most of documented history dating back approximately two thousand years. For the majority of history geothermal resources were primarily utilized as a heated water source. The ancient Chinese and Romans harnessed geothermal waters for use in bathing and cooking (Fridleifsson and Freeston). During the 13th century, a pipeline in Iceland was built to supply warm water to baths a few miles away from the source. In the 18th century, the Industrial Revolution instigated the first industrialization of geothermal resources where minerals were extracted from the geothermal fluid. It is likely that mineral extraction began before then, but this was the beginning of large scale extraction. Many useful minerals can be extracted from geothermal fluids, but during this time period salt was of interest in Iceland and boric acid in Italy (Fridleifsson and Freeston). The Industrial Revolution began the process of revolutionizing the scale of which geothermal resources can be utilized, but it was not until recently that the

technology was available to use geothermal resources to create geothermal energy the way it is thought of today.

The use of geothermal energy for residential heating and electricity only began in the last 120 years or so. The first residential heating system was installed in 1892 in Boise, Idaho, and electricity was first produced in 1904 at Larderello (which is the geothermal facility of interest for this project) in Tuscany, Italy (Tabak). While electricity production began at the beginning of the 20th century, it would take until the 1960's for aggressive expansion of geothermal electricity production in countries around the world including New Zealand, Japan, and the United States (Fridleifsson and Freeston). The use of geothermal energy for greenhouse farming sprung up all over the world during the 1920's including countries such as Iceland, Russia, New Zealand, and Hungary. During the 1950's the use of geothermal steam for industrial applications began to help supplement the large energy needs of industrial processes. Today, the main application of geothermal energy is to heating and electricity production, and the installed capacity has been steadily increasing over the last decade. As of 2008, geothermal energy electricity production has an installed capacity of over 10,000 MWe worldwide in 24 countries in both the industrialized and non-industrialized world (D. Gallup). The United States is the largest consumer of geothermal electricity followed by the Philippines which draws 23% of its power from geothermal resources. In terms of heating requirements, Iceland is the leading country obtaining 87% of its heating needs from geothermal resources (Blodgett and Slack).

2.3.2 Current Technologies

There are several different types of geothermal power plants in use today, and the differences between them arise from the differences in the geothermal resources they are designed to utilize. Geothermal energy can be contained in subterranean vapor, water, or hot rock, and each geothermal site contains some combination of these three. Vapor dominated systems are obviously preferred because it provides a direct supply of steam, but most of the resources around the world are water dominated (D. Gallup). Hot Dry Rock (HDR) dominated systems are the most difficult systems to extract energy from because it requires the addition of water to the rock which creates water level maintenance issues. There can also be major pumping concerns

depending on the porosity of the rock. Another major difference between geothermal resources is the temperature of the extracted steam or water. In the western United States alone, geothermal waters vary from 100 °C to 325 °C which allows for quite different energy production per unit of extracted water (Blodgett and Slack). The type and temperature of the geothermal resource are the major two factors that dictate what type of geothermal plant will be used.

There are three major types of geothermal power plants in operation today. The first is referred to as a Dry Steam Power Plant, and is designed to utilize the vapor dominated systems. These plants take the steam extracted from the ground and send it straight to a turbine. The condensed steam exiting the turbine is reinserted back into the ground. The second is the most common type of plant which is a Flash Power Plant that utilizes water dominated systems above 150 °C by extracting hot water from the ground and sending it through a steam separator (Blodgett and Slack). The steam separator will be at a lower pressure than the pressure in the ground which allows for much of the water to flash to steam, and the rest in referred to as "brine". This brine will be extremely concentrated with contaminants due to the loss of water in the steam separator, and causes extreme fouling problems in the pipes. The final type of plant is a Binary Power Plant that utilizes water dominated resources below 150 °C. The water is extracted from the ground and sent through a heat exchanger that heats a fluid with a lower boiling point, such as isobutane or pentafluoropropane, which then powers the turbine (Blodgett and Slack). The geothermal water is kept completely separate from the working fluid which makes for easy extraction and reinsertion into the ground. However, these plants experience fouling problems on the heat exchangers which drastically reduces the production capability of the plant. These are the three major types of plants, but plants can also be a combination of these to better utilize the resource. The most common is a Flash/Binary Plant where the brine exiting a steam separator is then sent to a heat exchanger before being sent back into the ground.

Fouling is one of the major problems of geothermal power plants regardless of plant design. The fouling of the pipes and heat exchangers requires the plant to shutdown to clean the system which results in a large financial loss to the company because of the cost of cleaning, lost operation time, and loss of efficiency during service. The geothermal loop experimental facility

at the Salton Sea Known Geothermal Resource Area in California must shutdown after approximately 42 days of operation due to fouling issues, and it takes days to weeks to clean the system (Jacobson, Rogers and Schoepflin). Therefore, the losses from fouling problems are considerable, and each plant has their own unique problems due to the unique chemistry of every geothermal resource. The plants operating at the Fushime geothermal field at Kyushu, Japan, have tremendous silica deposition problems due to the high temperature of the water in this region (Akaku). The Milos Geothermal Plant on Milos Island in Greece experiences fouling due to heavy metal sulfides and silicon compounds (Karabelas, Andritsos and Mouza). Plants in the Paris Basin also experience sulfide deposition, but high concentrations of dissolved metals are also present (Criaud and Fouillac). However, while each plant experiences their own fouling problems, they can be classifies into three major types of deposition which are sulfide deposition, silica deposition, and carbonate deposition.

2.3.2.1 Sulfide Deposition

The deposition of sulfur in a geothermal system is caused by the presence of both metal ions and sulfide in the working fluid. The metal ions and sulfide react causing a solid to form that precipitates out of solution. The main compound of sulfide deposition is iron sulfide, and its deposition process is described by the following reactions.

$$H_2S(g) \leftrightarrow HS^-(aq) + H^+(aq)$$

$$(1 + x)Fe^{2+}(aq) + HS^-(aq) \rightarrow Fe_{1+x}S(s) + H^+(aq)$$

$$Fe^{2+}(aq) + HS^-(aq) \rightarrow FeS(s) + H^+(aq)$$

$$Fe^{2+}(aq) + 2HS^-(aq) \rightarrow FeS_2(s) + 2H^+(aq) + 2e^-$$

$$3Fe^{2+}(aq) + 4HS^-(aq) \rightarrow Fe_3S_4(s) + 4H^+(aq) + 2e^-$$
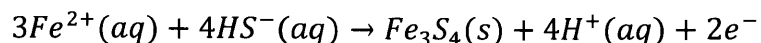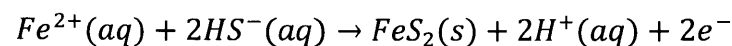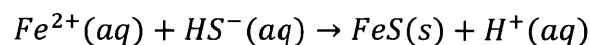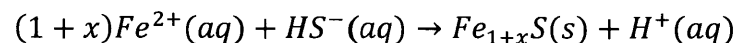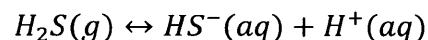
$Fe_{1+x}S$, FeS, FeS_2, and Fe_3S_4 are referred to as the mackinawite, kansite or troilite, pyrite, and

iron sulfide phases of iron sulfide deposition, respectively (Criaud and Fouillac). There is also an evolution to the compounds after they have been deposited that is summarized with the following reactions.

$$FeS(s) + HS^-(aq) \rightarrow FeS_2(s) + H^+(aq) + 2e^-$$

$$3FeS(s) + HS^-(aq) \rightarrow Fe_3S_4(s) + H^+(aq) + e^-$$

$$2FeS + FeS_2 \rightarrow Fe_3S_4$$
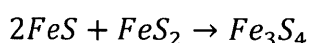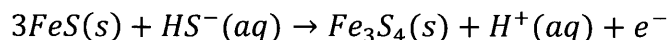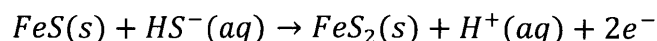
An increase in the concentration of HS⁻ or Fe⁺⁺ will increase the rate of iron sulfide deposition. The concentration of HS⁻ is a property of the geothermal fluid being extracted, and will not increase throughout the plant process. The concentration of Fe⁺⁺ however does not come from the ground but from the steel components. The corrosion of steel generates Fe⁺⁺ in the brine which interacts with the HS⁻ via the reactions above and deposits on component surfaces. The reactions for the corrosion of steel are given below.

$$Fe^0(s) \leftrightarrow Fe^{2+}(aq) + 2e^-$$

$$2Fe^{2+}(aq) + Cl^-(aq) + 3H_2O(l) \leftrightarrow \beta Fe_2(OH)_3Cl(s) + 3H^+(aq)$$
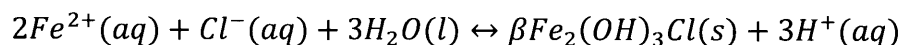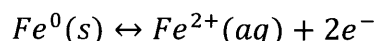
The first reaction given above is a summation of multiple reactions that are listed below (Ma, Cheng and Li).

$$Fe(s) + H_2S(aq) + H_2O(l) \leftrightarrow FeHS^-(aq) + H_3O^+(aq)$$

$$FeHS^-(aq) \leftrightarrow Fe(HS)(s) + e^-$$

$$Fe(HS)(s) \rightarrow FeHS^+(aq) + e^-$$

$$FeHS^+(aq) + H_3O^+(aq) \leftrightarrow Fe^{2+}(aq) + H_2S(aq) + H_2O(l)$$
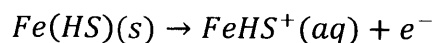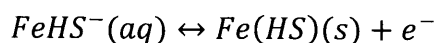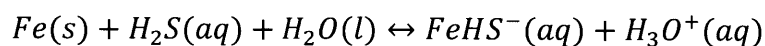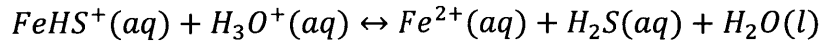
Deposition also occurs during corrosion by the following reaction.

$$FeSH^+(aq) \rightarrow FeS_{1-x}(s) + xSH^-(aq) + (1-x)H^+(aq)$$
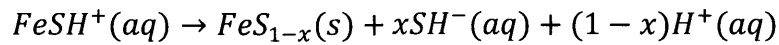
The corrosion of the steel leads to the insertion of not only iron to the brine, but also the other metals that make up the alloy of steel used. Therefore, it is common to observe deposition of nickel or manganese (depending on the alloy), but this deposition is negligible compared to the deposition of iron sulfide because of the large amount of iron in the steel. At a geothermal plant there will be some deposition due to the presence of metals such as Cr, Ni, Cu, As, or Mo already in the brine from either the well or different sections of the production process, but this deposition is minimal due to their low concentrations (Honegger, Czernichowski-Lauriol and Criaud).

The use of stainless steel instead of carbon steel for the pipes prevents sulfide deposition because stainless steel inhibits corrosion which prevents the generation of Fe^{++} in the fluid. Initially, the reaction of stainless steel in the presence of water and hydrogen sulfide results in the formation of nickel sulfide, iron sulfide, and chromium oxide by the following reactions (the reaction for iron sulfide is given above). These reactions are the most prevalent because nickel oxide, iron oxide, and chromium sulfides are not thermodynamically stable because of a large negative Gibbs Free Energy change is required for formation.

$$Cr(s) \leftrightarrow Cr^{3+}(aq) + 3e^-$$

$$2Cr^{3+}(aq) + 3H_2O(l) \leftrightarrow Cr_2O_3(s) + 3H_2(g)$$

$$Ni(s) \leftrightarrow Ni^{2+}(aq) + 2e^-$$

$$Ni^{2+}(aq) + HS^-(aq) \leftrightarrow NiS(s) + H^+(aq)$$
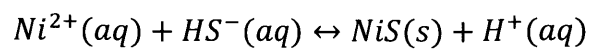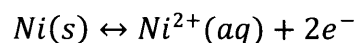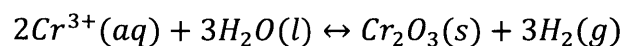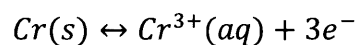
However, these reactions are not sustained due to the protective chromium oxide layer that forms. The nickel and iron sulfides go into solution, but the chromium oxide remains on the surface where it is formed and eventually builds a protective layer that inhibits further addition of sulfides to the brine (Tapping and Davidson). Therefore, a minimal layer of sulfide deposition will occur with the stainless steel, but not enough to cause significant fouling problems.

Similar to the chromium oxide on the stainless steel, the deposited iron sulfide on carbon steel can in some cases protect the steel from corrosion and thus prevent further deposition. This only occurs with the right combination of the different phases of iron sulfide. This inhibiting affects can be displayed when higher concentrations of the phases of troilite (FeS) and pyrite (FeS_2) are present because they have more protective properties. However, mackinawite ($Fe_{1+x}S$), kansite (FeS), and iron sulfide (Fe_3S_4) do not posses protective properties. Typically, the inhibiting effects on corrosion are only seen with low concentrations of H_2S and pH values of three to five (Honegger, Czernichowski-Lauriol and Criaud). The operating condition of the DCT are outside of these ranges, thus it is expected that the deposition will not inhibit corrosion. It has also been demonstrated in similar geothermal systems that the iron sulfide is permeable and allows for corrosion of the steel through the deposited iron sulfide (Ma, Cheng and Li). Sulfide deposition is present at the site of interest for this study, thus the understanding of these mechanisms will be crucial.

2.3.2.2 Silica Deposition

Near the end of the production process, silica fouling becomes a serious problem because the solubility of silica in water decreases as temperature decreases (Jacobson, Rogers and Schoepflin). Silica deposition is kept at a minimum upstream because the brine is at a higher temperature and the solubility of silica in water is unaffected by pressure changes in the steam separators (Criaud and Fouillac). However, after the brine has passed through the steam separators and heat exchangers it drops in temperature considerably, and the silica becomes supersaturated. This leads to the deposition of amorphous silica in the later phases of the production process. Amorphous silica deposits in the largest quantity downstream because it has the highest solubility of any phase of silica which results in it remaining in solution the longest.

Amorphous silica is also the most concentrated phase of silica in the brine, and it is therefore the most important (Criaud and Fouillac).

Amorphous silica flocculates out of the brine in a few different steps. After the brine has been supersaturated with amorphous silica and the silica has become suspended in the brine, the particles begin to bond together to form polymers (large molecules with repeating structure) less than the size necessary to deposit. This occurs throughout the brine to the point where the silica polymers are evenly dispersed through the brine. The particles continue to grow to the point where they pass a certain threshold (the particles are now known as colloids) and flocculate out of the brine (Gorrepati, Wongthahan and Raha).

It has been shown that the deposition rate of silica increases as the pH of the brine increases (Akaku). However, over the pH ranges typically of interest in geothermal systems the solubility of amorphous silica remains unchanged or slightly increases. While this is counterintuitive, it is most likely due to the fact that the silica must bond together to flocculate out of the brine, but the presence of acid impedes this process by re-separating the bonding particles. Silica deposition is usually very low if the pH of the brine is kept below 6 (Gallup and Barcelon). However, adding acid to lower the pH drastically increases the corrosion of the system resulting in a new set of problems. Therefore, there has been research into the use of inhibitors to prevent silica deposition without increasing corrosion (Gallup and Barcelon). However, acids continue to prove themselves to be the best way to prevent silica deposition.

The salt content of the brine also has a major affect on the rate of silica deposition. The solubility of amorphous silica decreases with increasing concentrations of salts, but some salts have more of an influence than others (Gorrepati, Wongthahan and Raha). For example, $AlCl_3$ causes more deposition than a similar concentration of NaCl. This is a result of the increased ionic strength of the $AlCl_3$. However, while the presence of the salts results in increased deposition, they do not deposit themselves.

Silica deposition is a major problem for binary cycle plants because the binary cycle heat

exchanger is located downstream where the temperature of the brine is lower. Thus, the further temperature decrease caused by the heat exchanger results in a large amount of silica precipitation out of solution. Silica is not present in significant concentrations at the site of interest as the water comes from the turbine and steam does not transport silica.

2.3.2.3 Calcium Carbonate Deposition

Calcium carbonate is present in geothermal fluids because it is a common compound in rock, and thus must be sent through the plant with the fluid. The deposition of calcium carbonate occurs when the brine undergoes a large pressure drop as experienced by the brine in steam separators or during the production well extraction process (Chan, Rau and DeBellis). However, deposition can also occur due to the pressure drops from valves or constrictions in the pipes. Deposition occurs because the pressure drop decreases the solubility of CO_2 in the solution as defined by Henry's Law. The decrease in CO_2 in the solution increases the pH of the brine (Karabelas, Andritsos and Mouza), and the concentration of CO_3^{2-} increases resulting in the formation of $CaCO_3$ which deposits. This process can be summarized in the following reactions. The connection between CO_2 and the pH is explained in these two reactions.

$$CO_2(g) + H_2O(l) \leftrightarrow H_2CO_3(aq)$$

$$H_2CO_3(aq) \leftrightarrow HCO_3^-(aq) + H^+(aq)$$
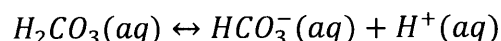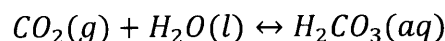
A decrease in the concentration of CO_2 results in a decrease in the concentrations of H_2CO_3 and thus of H^+. A drop in the concentration of H^+ results in an increase in the pH of the brine by definition. As the pH of the brine increases, the solubility of $CaCO_3$ decreases resulting in supersaturation of $CaCO_3$ which initiates deposition. The deposition of $CaCO_3$ will decrease its concentration in the fluid which in turn decreases the pH of the brine by the following equations which temporarily halts its deposition. The pH decreases because the drop in concentration of $CaCO_3$ decreases the concentration of CO_3^{2-} which in turn causes an increase in the concentration of H^+.

$$Ca^{2+}(aq) + CO_3^{2-}(aq) \leftrightarrow CaCO_3(s)$$

$$CO_3^{2-}(aq) + H^+(aq) \leftrightarrow HCO_3^-(aq)$$
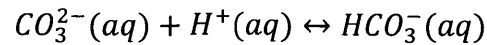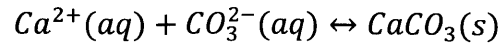
While calcium carbonate deposition is drastically affected by pressure changes, it is not influenced by temperature changes (Criaud and Fouillac). Thus, calcium carbonate deposits readily at the beginning of the production process, but not at the end when pressure changes become less prevalent. Calcium carbonate deposition is not present at the site of interest for this study.

2.3.3 Design Criteria: DCT

The objective of the geothermal aspect of this project is to determine a solution to the fouling of a dry cooling tower (DCT) due to deposition by identification of a nanosurface that can be applied to the inside of the pipes. Currently, a DCT is in operation at the Larderello Geothermal Power Plant that has a capacity to cool approximately 5% of the needs for the plant. It was built to test the viability of converting to a DCT, and has provided extremely useful data concerning many different aspects including its operating conditions, chemistry, and the nature of the deposition.

2.3.3.1 Dry Cooling Towers

A dry cooling tower (DCT) is an alternative type of cooling tower that uses the convection of air rather than evaporation as the main means of heat transfer to cool the working fluid. The working fluid (typically water) is sent into many small tubes that have large fans continually blowing air over them. The heat transfer of a DCT is limited compared to traditional wet cooling towers (WCT) because of the low specific heat, density, and thermal conductivity of air, but there are several advantages to using a DCT. A few of these advantages are a greater preservation of water since evaporation is not necessary, negligible maintenance, helps maintain a clean working fluid, and no corrosion is caused by the air. However, in the case of the plant in Larderello, Italy, there is an additional motivation for a DCT because of the presence of hydrogen sulfide in the water. Hydrogen sulfide is present because it is extracted from the ground with the geothermal

water, and evaporates along with some of the water in the steam separators. It travels through the turbine and is condensed back into a fluid with the water in the condenser. Thus, hydrogen sulfide is present in the working fluid sent through the cooling tower, but unfortunately hydrogen sulfide is toxic and has a powerful odor which makes it undesirable to expose to the plant workers and the environment. The use of a WCT will result in the release of hydrogen sulfide which is why the application of a DCT to this production process has been identified as a practical solution to this problem.

However, the application of a DCT as a solution to this problem is not easy because of the fouling problems caused by hydrogen sulfide on low carbon steel pipes. The presence of hydrogen sulfide in the water results in sulfide deposition on the pipes in the DCT causing the cooling tower to be cleaned twice a year using water lancing. Water lancing is a process that involves the cleaning of equipment using high pressure water to force the

Figure 5-Picture of the dry cooling tower at the Larderello Power Plant (courtesy of ENEL).

deposition off of the surface. The use of stainless steel for the pipes of a DCT can prevent the sulfide deposition by preventing the insertion of iron ions into the water from corrosion, but the expense of stainless steel makes this solution impractical. A DCT requires a large amount of steel because a large amount of surface area is required to have the heat transfer required due to the cooling heat capacity of air. Therefore, the use of stainless steel for this application is impractical due to the large amount of steel required and the associated cost. Therefore, an alternative method to solve the problem of sulfide deposition in this DCT is needed.

2.3.3.2 DCT Operational Data

The data collected from the DCT clearly demonstrates a loss of capacity over time which justifies the need for this study. The graph below displays data for the volumetric flow rates and

pressure drops that was obtained from the operation of the DCT over approximately one year of operation. The loss of capacity of the heat exchanger over the first 6 months of operation is clearly demonstrated. The loss of flow rate is related to the deposition that occurs on the heat exchanger tubes which reduces the flow area and flow rate. There appears to be three phases of deposition. The first is a slow steady decline that is eventually followed by an accelerated reduction in the second phase. The transition between the two phases is fairly abrupt, and is similar to the transition stage seen during localized corrosion. The final phase is the halting of the reduction of the flow rate which is likely due to the flow eroding the new deposition resulting in equilibrium in the deposition on the tube. During the time period of data retrieval there was a 2 to 3 month period of shutdown over which the pipes were cleaned. The increase in flow rate and cooling capacity after the cleaning is clearly demonstrated.
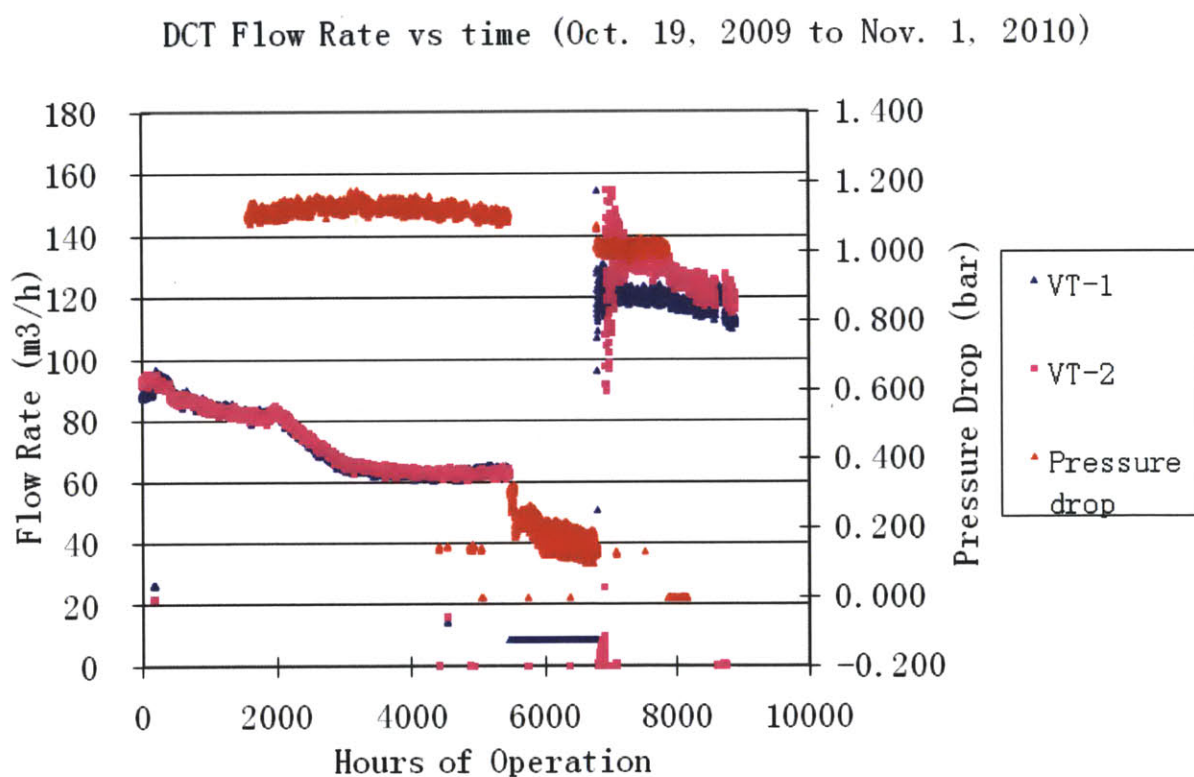
Figure 6-The volumetric flow rate and pressure drop of the DCTs over a one year period.

The deposition found on the DCT pipes was analyzed and determined to contain sulfur. The DCT itself does not contain any sulfur which indicates that the sulfur must be entering the system through the working fluid. The chemical analysis of the working fluid is presented in

Table 2. Therefore, the sulfur compounds identified from the chemistry analysis of the fluid indicates that the deposition must be initiated by the presence of sulfate or sulfite ions, or hydrogen sulfide. Hydrogen sulfide is the likely source because it is gaseous and can travel with the steam through the turbine.

CHEMICAL ANALYSIS										
WATER ANALYSIS OF LARDERELLO_3 DRY COOLING TOWER (DCT)										
On field Data										
POINT OF SAMPLING	**sampling #**	**Date**	**T**	**p**	**pH**	**Cond.**	**Alc.**	**Alc. rit.**		
			°C	Bar		mS/cm	mg/L			
DCT INLET	**152711**	05/19/2011 9.50.00	36.8	1.55	6.69	4300	0.98	0.05		
DCT OUTLET	**158911**	05/26/2011 10.30.00	32.4	1.07	6.79	4200	0.85	0.00		
Lab Data										
POINT OF SAMPLING	**sampling #**	**Date**	**Na**	**NH₄+**	**SO₄--**	**SO₃--**	**S₂O₃--**	**S₀**	**H₂S**	**S tot. (calc.)**
			mg/L							
DCT INLET	**152711**	05/19/2011 9.50.00	522	287	1772	21.8	<10	<1	2.8	609
DCT OUTLET	**158911**	05/26/2011 10.30.00	602	293	2015	<10	<10	<1	2.9	685

Table 2-Chemistry of the working fluid operating in the DCT at the Larderello Power Plant. Provided by ENEL.

2.3.3.3 Deposition Analysis

A sample of the DCT pipes from the Larderello site were taken for study. The DCT uses 1" OD, 0.83" ID, INOX 10456 pipes with aluminum fins around the outside of the pipe. To preform the analysis, the fins were removed and approximately 10" of the pipe was sectioned in half. The fouling on the pipes was sizable, and a sample of the deposit was taken to detemine the phase and composition of the deposition. Figures 7 and 8 are pictures of the sectioned pipe and the deposition.

Figure 7-The 10" section of the sample DCT fouled pipe.
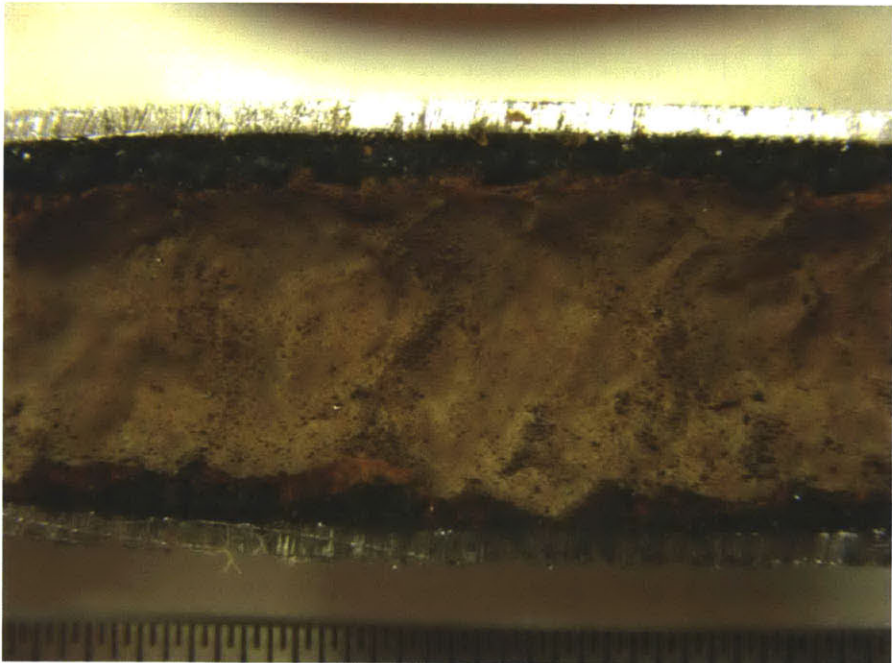
Figure 8-The deposition on the DCT fouled pipe in the condition that it sits on the pipe.

The SEM was used to inspect the deposition in its form as it sits on the pipe. In other words, there was no treatment to the sample before inspection. Figure 9 displays an image of the depositon. EDS was performed on the deposition and it demostrated a mostly iron and oxygen composition as seen in Figure 10. There was sulfur present, but it was not the majority of the composition. In fact, in a second EDS anaylsis there was no sulfur detected so it is safe to assume that sulfur's presence is at the bottom of the detectable range. This would indicate that the DCT are exposed to oxygen during the corrosion which causes the formation of iron oxide on the surface. This is amplified by the fact that there is sulfur in the system as well which results in the formation of iron sulfide. The combination of the two result in considerable deposition. This also demonstrates that the influence of hydrogen sulfide on the deposition in the system is not just the presence of sulfur, but also the insertion of hydrogen ions into the system which propages the corrosion which reacts with oxygen. The presence of iron oxide demonstrates the need to prevent corrosion in the system. It should be noted that oxygen is likely entering the system from outside the system, but even if the system was air tight there would still be oxygen produced by hydrolysis of water.
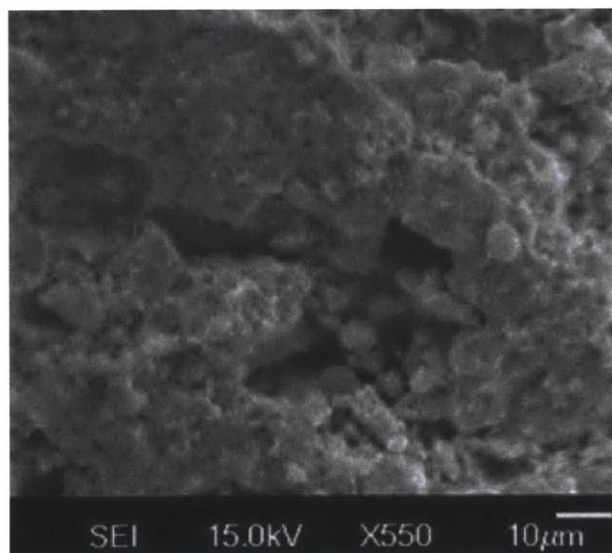
Figure 9-SEM image of the deposition on the DCT pipe as it sits on the pipe.

Element	Weight%	Atomic%
O K	32.84	62.47
S K	2.29	2.17
Fe L	64.87	35.36
Totals	100.00	

Figure 10-EDS spectrum for the deposition on the DCT pipe, and the corresponding atomic weight percents.

The deposition was also analyzed using the XRD to determine the compound and phases present in the deposition. To obtain this data, it was required to scrape the deposit off the pipe and turn it into a fine powder. Therefore, the structure it possessed on the pipe was lost. The spectrum and analysis data are shown below in Figure 11 and Table 3.

Figure 11-The resonance peak spectrum obtained during the XRD analysis of the deposition on the pipe.

Visible	Ref. Code	Score	Compound Name	Displaceme nt [°2Th.]	Scale Factor	Chemical Formula
*	04-012-7311	55	Sulfur	0.000	0.701	S
*	04-008-4511	46	Iron Oxide	0.000	0.432	Fe3 O4
*	04-010-4300	45	Iron Oxide Hydroxide	0.000	0.867	Fe O (O H)
*	01-073-6522	37	Iron Oxide Hydroxide	0.000	0.381	Fe O (O H)

Table 3-The compounds matching the resonance peaks from the XRD analysis of the deposition on the pipe.

As expected, iron oxide is shown to be very prominent in the deposition. It was unexpected to find it in a compound with hydroxide; however the presence of the hydroxide indicates the region on the Pourbaix Diagram which the DCT operates. Figure 12 is the Pourbaix Diagram for iron, and from the analysis above it is likely that the system is in the region indicated for Fe_3O_4 and $Fe(OH)_2$. This indicates that it is a somewhat oxygen starved environment since more oxygen would lead to a higher potential. It is also intriguing that the DCT does not operate in the Fe^{++} region which is the known common region for geothermal plants with sulfide deposition. It should also be noted that the region indicated below can be achieved with a pH less than 7 because the lines are altered based on the chemistry of the system. Therefore, for this system the iron oxide and iron hydroxide regions clearly stretch into the acid region.
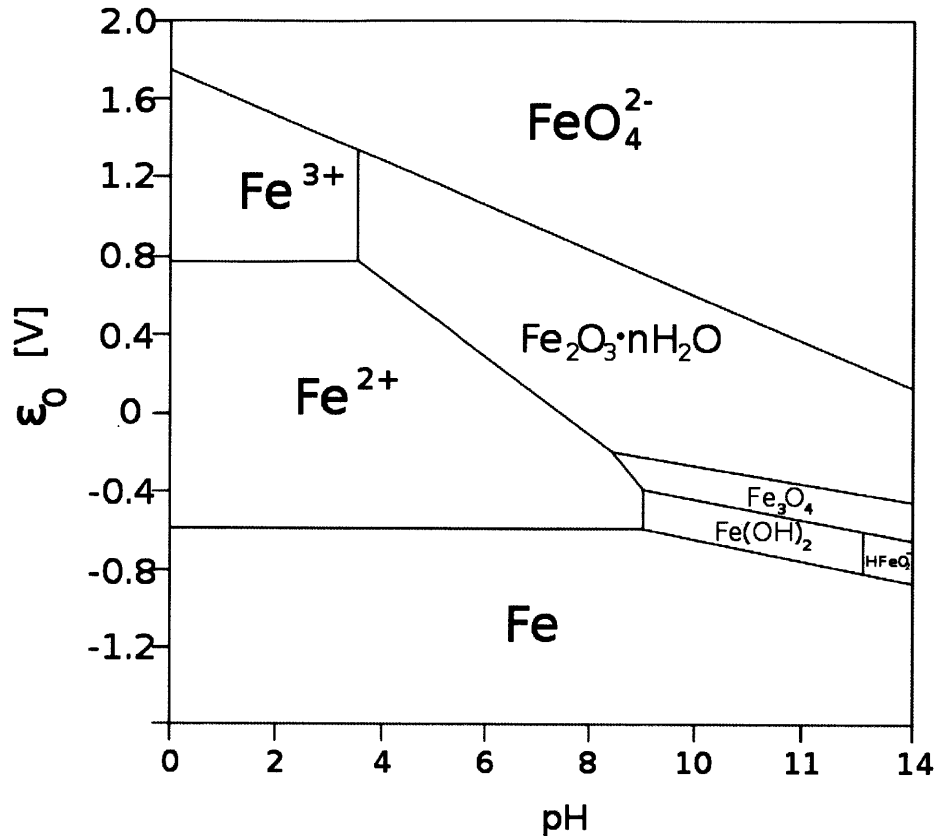
Figure 12-The Pourbaix Diagram for iron.

2.3.4 Chemistry

The chemistry of the brine in a geothermal system is a major factor in the rate of deposition. As the brine progresses through the plant, the fluid properties and operating conditions change resulting in different rates and types of deposition. Therefore, a firm understanding of several chemical mechanisms that affect the brine is required to correctly analyze the deposition and corrosion in geothermal systems. This section is meant to provide a background on the chemistry concepts necessary for this analysis, but not provide the detailed analysis of the chemistry of the brine. However, the examples used are pertinent to this project.

2.3.4.1 Henry's Law

Henry's Law describes a fluid-vapor system where the vapor is at some pressure, and the system is at a constant temperature. It states that the amount of dissolved gas in the fluid is proportional to the partial pressure of that gas in the vapor above the fluid while the system is at equilibrium.

Thus, a sudden decrease in the pressure of the vapor would result in a drop in the solubility of the gas in the liquid and some of the gas will leave the fluid and become vapor. The equation describing Henry's Law is given below where p is the partial pressure and c is the concentration of the gas in the solution.

$$p = k_H c$$

The value of the constant k_H is dependent on the solute and solvent, and it is a function of temperature. The value of k_H can be determined using the following set of equations.

$$k_H(T) = k_H(T^*)e^{\left(-c\left(\frac{1}{T}-\frac{1}{T^*}\right)\right)}$$

$$C = -\frac{\Delta H_{solv}}{R}$$

The constant C is the enthalpy of solution, which is the energy change of the system during the dissolving process, divided by the ideal gas constant (8.31447 J/molK). Therefore, C is a value that can found in a table based on the solute and solvent. The quantity T* is a reference temperature, and by convention it is always 298 °K (room temperature).

2.3.4.2 Equilibrium Constant

In order to determine the equilibrium concentration of the different components of a system it is necessary to understand the concept of an equilibrium constant. Chemical reactions have the capacity to react in both directions rather than just one. The equilibrium constant defines the equilibrium rate at which the forward and backward reactions occur. In the case of a solid dissolving into a liquid, the reaction is a solid chemical becoming a chemical or chemicals in an aqueous solution. However, the reaction of the aqueous chemical dropping out of solution and becoming a solid again is also taking place. Therefore, the concentration of the solution is determined by the rate of the equivalent forward and backward reactions, and this comparison is quantified by the solubility constant (a specific type of equilibrium constant).

As an example, the impact of carbon dioxide on the pH of a solution will be examined. Below are the equations for the reaction of carbon dioxide and water that produces the hydrogen ion and carbonic acid.

.

$$CO_2(aq) + H_2O(l) \leftrightarrow H^+(aq) + HCO_3^-(aq)$$
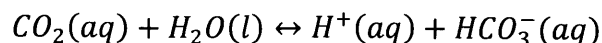
These equations state that it is both possible for carbon dioxide and water to react to from a hydrogen ion and bicarbonate, and for a hydrogen ion and bicarbonate to react to form carbon dioxide and water. Since the pH of the system is based on the concentration of H^+, the pH of the system is directly dependent of the solubility constant and therefore equilibrium coefficients of products and reactants in a balanced equation which is defined below for this system.

$$k = \frac{\{H^+\}^1\{HCO_3^-\}^1}{\{CO_2\}^1\{H_2O\}^1}$$

2.3.4.3 Flocculation vs. Precipitation

The manner in which a solution, or mixture of solids in a solution, deposit particles is important because this describes the manner in which the brine deposits chemicals on the pipes or heat exchanger surfaces. Silica, for example, will flocculate out of solution and deposit on the pipe. Flocculation is the process where a microscopic solid substance, known as a colloid, that is suspended in a fluid will agglomerate and drop out of the fluid in flakes. The solid is not dissolved in the fluid, but suspended, and before depositing the particles of the substance combine to form larger structures, or flakes. In a geothermal system, this can occur if too many additives are added to the brine, and particles begin to adhere to each other more readily. A similar process to flocculation is precipitation which is the formation of solids in a solution which, in this case, would eventually drop out of the fluid and deposit on the pipe or heat exchanger. The difference between flocculation and precipitation is important to silica deposition which flocculates rather than precipitates. In other words, when the temperature of the brine drops causing the solubility of silica in water to decrease, the silica will fall out of solution and become suspended in the brine rather than depositing immediately.

3. Selection of Test Surfaces

The most challenging and important aspect of this project is the selection of the surfaces worthy of testing. There are a wide variety of materials, structures, and coatings that have been investigated for their use on a solar thermal receiver, but there is little information available on receiver applications involving operating temperatures above 700 °C. Similarly, the use of nanosurfaces for antifouling applications has not been studied extensively. Thus, the challenge is determining potentially beneficial surfaces to test for each application from the data obtained from similar studies. This section is a review of the potential types of surfaces to test, and the justification for the surfaces chosen to test here.

3.1 Solar Receiver Test Surfaces Decision Criteria

The main criteria that will determine the selection of the surfaces are the surface's optical properties, and the surface's thermal stability. A surface will be tested for performance, for benchmarking, or for validation, and surfaces will be chosen based on their ability to fulfill one of these purposes. The thermal stability is necessary for both consistency in the testing, and the production of valid data.

3.1.1 Testing Strategy

The main objective of the tests will be to determine the viability and potential benefits of the chosen surface for implementation. Therefore, one of the surfaces tested will be uncoated and untreated Inconel 617 which will serve as a benchmark upon which the benefits, or lack thereof, of the chosen surface can be compared. Also for the purposes of comparison, a black body surface will be tested which will help to validate the obtained data from the experiments. As stated previously, an ideal black body surface is unobtainable so a surface must be chosen to imitate the black body. The rest of the surfaces tested will either be potential coatings or surfaces to validate the potential coatings. The potential coatings will obviously be tested to determine their optical properties, but other surfaces may need to be tested to prove the thermal stability of the potential coating. For example, a multilayered coating might require testing of the individual sub-layers to determine thermal stability, or a nanosurface will require the testing of a plain surface of the same material to quantify its benefits. Thus, there will probably be one potential

coating, a few validation surfaces, and two benchmark surfaces selected for testing.

3.1.2 Thermal Stability

Due to the high operating temperatures of this system, the thermal stability of the chosen materials is important to justify the extended use of the surface. Thermal stability refers to the ability of a surface to maintain its shape, structure, or morphology at elevated temperatures. Diffusion of atoms in the material and oxidation are the fundamental causes of these changes within a surface. Diffusion is a process that occurs in all materials at all times, but the rate of diffusion is exponentially related to temperature. At room temperature diffusion is extremely small, but at the operating temperature for this project diffusion can be very quick. When at elevated temperatures the diffusion of atoms is easier because of the increased energy in the system (Kaltenbach, Graf and Kohl). Therefore, it is necessary to determine if the diffusion of the materials in the surface is proceeding relatively quickly or slowly. The oxidation of the surface must also be considered because the receiver will be operating in an oxygen environment. Thus there are many materials, specifically pure metals, that should not be used for this application because they will immediately oxidize and change optical properties. The correct choice of material will allow for use of the receiver for an extended period of time because it will retain its advantageous properties.

Oxidation and diffusion in these materials leads to the destruction of the favorable properties of the surface. In a nanosurface, the atoms need only move a few nanometers to change the nanostructure which nullifies its advantages. For a coating with many nanometer thick layers, these layers will diffuse into each other creating one large combined layer rather than many individual layers. All materials eventually succumb to diffusion given a high enough temperature, and this is a common challenge in many engineering applications. However, it is particularly influential in this project due to the small distance that the atoms must travel to negate the optical properties.

3.1.2.1 Diffusion Barriers

Since thermal stability is related to the diffusion of atoms in the system, materials that are

These materials are listed for the purpose of benchmarking. Therefore, silicon carbide would be an appropriate choice because of its high emissivity as seen in Figure 13. Since silicon carbide does not possess selective properties so the emissivity should be constant across the spectrum. Therefore, silicon carbide would be a cheap, convenient black body surface to test.

3.2.2 Carbon Nanotubes

Carbon nanotubes (CNTs) have become a premiere topic for research since their discovery in the early 1990's because, in part, of their incredible mechanical, electronic, and optical properties. It is the combination of all of these properties that make CNTs appealing for use as a high temperature black body. CNTs are one of the strongest and stiffest materials currently known, and this strength arises from the sp^2 carbon bonds that compose the structure. This strength makes CNTs attractive for a wide variety of materials applications. Mainly, they can be used to increase the adhesion between material layers or fibers on a nanoscale to increase the material strength. Specific examples of this include increasing the interlaminar properties of composite materials produced by prepreg methods (Wardle, Hart and Garcia), and the

Figure 14-A carbon nanotube forest structure that displays the light absorbing properties of carbon nanotubes.

strengthening of the adhesion of alumina fibers for enhanced interfacial shear strength on armor layers (Wardle, Hart and Garcia). Another interesting property of CNTs, is that they display the electronic properties of a semiconductor which for the purposes of this project is important because of the influence this has on the optical properties. CNTs demonstrate the optical properties of a black body due to the semiconducting properties and multiple reflections within the CNT forest structure. The forest structure describes a surface of CNTs that are all oriented vertically which would be optimal for this application. This high absorptivity behavior is demonstrated across the entire solar spectrum. The challenge with CNTs is retaining their structure at high temperature. Single-walled carbon nanotubes (SWCNT) are known to become

resistant to diffusion and oxidation will be extremely useful. A material resistant to the affects of diffusion and oxidation can be placed between layers that are composed of materials that are more prone to diffusion and oxidation. This is known as a diffusion barrier. This will help inhibit the movement of atoms between the layers which will increase the thermal stability of the system. The uses of diffusion barriers will prove to be extremely relevant in the analysis of selective surfaces. Platinum and molybdenum have been shown to be an excellent diffusion barrier which explains their frequent use in multi-nano-layered coatings (Thornton and Lamb).

3.2 Black Body Options

For the purposes of comparison, it would be very beneficial to test a black body surface along with the selective surface. However, a black body surface does not exist, and a surface must be chosen with properties similar to a black body. There are many strategies to imitate a black body that are not necessarily surfaces, but rather enclosures that allow for measurements of a system with no incident radiation at high temperature (Cezairliyan and Miiller) (Pompei). However, the needs for this project require an actual surface, and two possibilities were found.

3.2.1 Silicon Carbide

A good black body will have high emissivity values across the spectrum, but finding a suitable surface to produce these high values is challenging. Therefore, the next best surface to use is a material that has a high emissivity across the spectrum, and a relatively constant value at the temperature ranges of interest. It is important that the emissivity remain constant across the different temperatures of interest because it becomes easier to benchmark the emissivity analysis of the other surface as their temperatures drop. Figure 13 displays multiple materials that have relatively constant emissivity values across the temperature ranges of interest in this study.
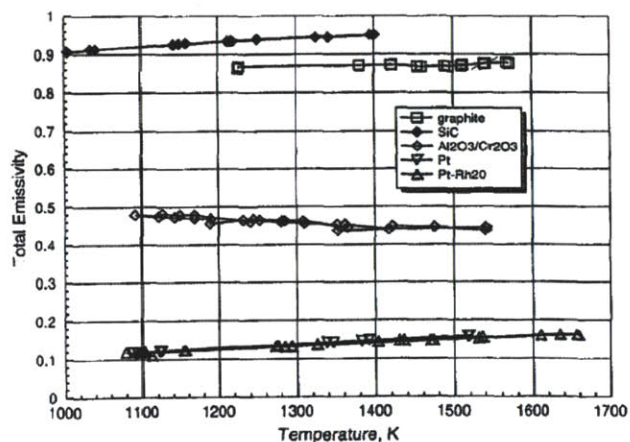
Figure 13-Total normal emissivity of various materials with the potential for emissivity benchmarking (Neuer and Jaroma-Weiland).

thermally unstable around 500 °C, but multi-walled carbon nanotubes (MWCNT) are reported to be stable up to 2900 °C (Begtrup, Ray and Kessler). Therefore, there is potential for the application of MWCNT to create the black body needed for testing.

3.3 Solar Selective Surface Options

The potential benefits of using a surface with selective optical characteristics are promising enough to warrant investigation. Therefore, the candidate surface chosen will attempt to display these properties. However, there are many different types of surfaces that demonstrate selective optical properties, and a selection requires an extensive analysis of the different options.

3.3.1 Metal Oxides

A practical, effective option for creating a selective surface is the use of a metal oxide. Metal oxides are the oldest and simplest selective surfaces considered for applications to solar thermal receivers. Transition metals have the most effective optical properties due to the semiconductor characteristics that they possess. More specifically, the most common metal oxides studied are chromium, molybdenum, cobalt, and nickel oxides. The main disadvantage to metal oxides is that they tend to have higher emissivities than more elaborate surfaces (Braendle). Metal oxides originate from the use of metal in oxygen environments, and the metal oxide usually has increased emissivity compared to its pure parent metal. However, the solar thermal receiver in this project is designed to operate in air, and thus oxides must be taken into account when using metals.

Chromium oxide and molybdenum oxide have been shown to display favorable optical properties at low temperatures. Chromium oxide has been identified as having the favorable optical properties of 0.87/0.14 (α/ε) at 100 °C (Kung), and has been shown to possess favorable adhesion properties on most surfaces (Mareichev, Fridberg and Churkin) and corrosion prevention properties (Bayati, Janghorban and Shariat). Unfortunately, chromium oxide becomes thermally unstable around 300 °C and loses its optical properties (McDonald). Molybdenum oxide also becomes unstable above 300 °C (Hosseini, Smith and Critchley), but molybdenum itself has been shown to have a low emittance (Cverna) and beneficial values in

other types of selective surfaces (multi-nano-layered coatings). While these metal oxides display promise as selective surfaces, they do not possess the thermal stability needed for this project.

However, both cobalt oxide and nickel oxide display the thermal stability needed for this project. Cobalt oxide is another metal oxide that has displayed promising optical properties, and has been extensively studied. Cobalt oxide can contain multiple phases (CoO and Co_3O_4), and it is apparent that Co_3O_4 is the more promising phase for this application (Barrera, Viveros and Morales). Black cobalt oxide (Co_3O_4) was indicated to have optical properties of 0.9/0.2 (α/ε) while being thermally stable at 650 °C which is a higher thermal stability than most metal oxides (McDonald). In another source, it is claimed to be stable at 1100 °C while maintaining an absorptivity of 0.9 (Kokoropoulos, Salam and Daniels). However, at this temperature the emissivity of cobalt oxide has increased beyond the 0.2 measured at 650 °C, and its spectral emissivity can be seen at high temperature in Figure 15. While cobalt oxide is promising due to its thermal stability, it appears that nickel oxide (NiO) displays the same thermal stability with improved emissivity properties as seen in Figure 15 (Kokoropoulos and Evans). Therefore, nickel oxide appears to be the metal oxide of choice since it is indicated to have a similar absorptivity to cobalt oxide (Kreith and Kreider). (It is also worth noting that the thickness of the applied layers has a drastic effect on the optical properties as seen in Figure 15, and will be discussed more thoroughly in section 3.4.1.)
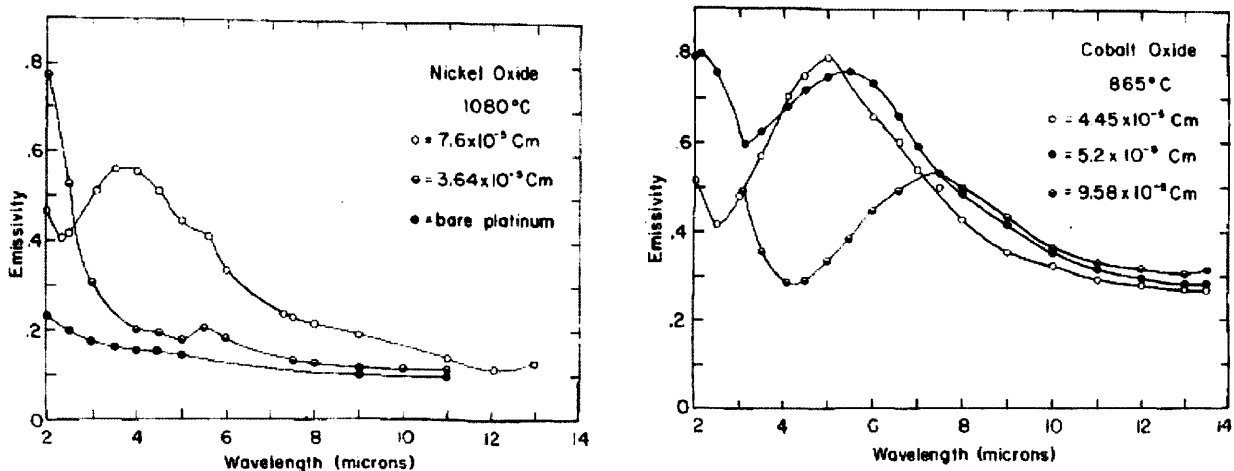
Figure 15-High temperature emissivities for different film thickness of nickel oxide and cobalt oxide (Kokoropoulos and Evans).

3.3.2 Multi-Nano-Layered Coatings

Another possibility for the creation of a selective surface is to use a multi-nano-layered coating. A multi-nano-layered coating consists of a few layers with thicknesses on the order of hundreds of nanometers that typically consist of different materials which each serve a different function in the coating. This allows for the beneficial properties of multiple different materials to be utilized together in one surface. The main elements used in these coatings are typically nickel, aluminum, nitrogen, titanium, tin, platinum, and molybdenum. Diffusion is a major problem for these surfaces due to how thin the layers
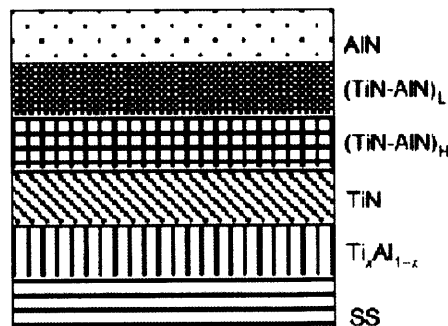
Figure 16-Example of a multi-nano-layered coating (Lei, Miao and XiaoPeng).

are. At high temperature the diffusion of atoms from one layer to another occurs quickly which negates the properties of each layer. However, the use of diffusion barriers as some of the layers can stabilize the system and allow operation at higher temperatures.

The physics of these coatings are quite complex in both the interactions between the different layers, and the interactions between the layers and the incoming radiation. The two major factors to consider for interactions between the layers are adhesion and diffusion. These factors can constrict the choices of materials and layer placement. Some layers must be chosen for their ability at act as a diffusion barrier or adhesion enhancer which can interfere with the coatings absorption properties. While contending with these concerns, layers must also be chosen to provide favorable absorption with the incoming radiation. A general strategy is to have an infrared reflector as the base layer on the substrate, a high absorber layer on top of the infrared reflector, and an anti-reflection layer as the top layer on top of the absorber (Esposito, Antonaia and Addonizio). While this arrangement is not true for every multi-nano-layered surface, the logic behind most coatings does fit this formula. The most important layer is the absorbing layer, and the other layers enhance its features. It is common for a cermet (section 3.3.3.3) to be used as the absorbing layer of a multi-nano-layered coating. The thickness of the absorbing layer is extremely important because these layers will best absorb radiation of similar wavelengths to its thickness (Oloomi, Saboonchi and Sedaghat). Therefore, the absorbing layer is usually the

thickest because it must be several hundreds of nanometers thick. The anti-reflection layer is used to enhance the amount of light that enters the absorption layer. The reflectivity of a surface is related to its refractive index, and a smaller change in the refractive index between the two media results in less reflectance. Therefore, an anti-reflection layer will have a refractive index between that of the air and the absorber to allow for a transition layer (Bostrom, Wackelgard and Westin). It is established that thin coatings or layers translate to low emission (Gillette). Thus, the thermal emittance will not be increased if the anti-reflection layer is kept sufficiently thin. The infrared reflector serves the task of reflecting the radiation produced by the substrate back into the material. The infrared reflector does not directly affect the absorption because the solar spectrum is not as important in the infrared region, but it can reflect the incoming radiation that has been transmitted through the absorbing layer back into the absorber.

There are quite a few examples of multi-nano-layered coatings that have been studied, most with the intent to be used in CSP parabolic trough plants. Some coatings were investigated for their optical properties with no regard to their diffusion or thermal stability which results in them having thermal stabilities less than 300 °C. However, they are worth discussing because they do possess favorable optical properties which in literature is defined by the solar selectivity ratio which is the absorptivity divided by the emissivity. A coating with a bright nickel first layer and a black nickel absorbing layer as the second layer demonstrated properties of 0.91/0.1 (α/ε) (Lira-Cantu, Sabio and Brustenga). Another example is a nickel pigmented aluminum oxide that displayed 0.92/0.11 (α/ε) optical properties (Wazwaz, Salmi and Bes). While these coatings were not considered for high temperature applications, there has been research into thermally stability coatings at high temperatures. An alumina and molybdenum based coating of $Al_2O_3/Mo/Al_2O_3$ displayed optical properties of 0.9/0.2 (α/ε) while becoming unstable at 550 °C (Thornton, Penfold and Lamb). In this surface, the molybdenum acted as a diffusion barrier between two layers of alumina that were deposited with different methods. A similar surface with layers of $Pt/Al_2O_3/Pt-Al_2O_3/Al_2O_3$ had properties of 0.9/0.1 (α/ε) and was stable to 600 °C (Thornton and Lamb). The $Pt-Al_2O_3$ layer is a cermet created by inserting platinum nanoparticles into alumina. The coatings with the highest thermal stability found were both found by the same research group. A coating with layers of $TiAl/TiN/TiN-AlN_H/TiN-AlN_L/AlN$, which is demonstrated in

Figure 16, displayed optical properties of 0.86/0.34 (α/ε) (Lei, Miao and XiaoPeng), and a coating of TiAl/TiAlN/TiAlON/TiAlO demonstrated 0.9/0.15 (α/ε) (Lei, ShuMao and LiJun) at their highest thermal stability of 800 °C. However, while these coatings have impressive thermal stability, they cannot be used for this application where temperatures may rise to 1000 °C.

3.3.3 Nanosurfaces

The use of nanosurfaces also allows for the creation of a selective surface. A nanosurface is defined as a surface that has surface structures sized or spaced on the nanometer scale, or has nanoparticles embedded in a dielectric matrix (Oelhafen and Schuler). Basically, nanoparticles can either be used to create structures on the surface, or they can be inserted into the surface to affect the structure of the surface itself. Therefore, each nanosurface is drastically different than the others and creates favorable properties using different physical methods. However, while each nanosurface affects the structure of the surface in a different manner, the fundamental challenge with using all nanosurfaces is their high temperature stability.

3.3.3.1 Dendrites

One of the most promising nanostructures for absorbing light is dendrites. A dendrite is a crystal that develops with a typical multi-branching tree-like form (Katumba, Olumekor and Forbes). It is this form that gives this structure favorable absorbing properties because of multiple reflections as the incident photons penetrate the needle maze. The needle maze creates cavities on the surface that allow for the light for reflect between the surface and the bottom of the "branches" in the dendrite structure until the light is absorbed. The disadvantage of dendrite structures is that the increased surface area of the

Figure 17-A dendrite structure created by amorphous nanoparticles embedded in NiO (Katumba, Olumekor and Forbes).

structure gives the surface a higher emissivity because it is easier for radiation to escape. Therefore, an effective dendrite surface will consist of a low emissivity material that relies on the dendrite structure to provide the high absorption. A tungsten dendrite surface is an excellent

example of this because tungsten has a low absorptivity and emissivity, but the surface displays properties of 0.98/0.26 (α/ε) at 550 °C which is its thermal limit (Cuomo, Ziegler and Woodall). Another example of the potential of dendrite structures is a surface consisting in a combination of Ni_2Sn_2, Ni_2Sn, and Sn that displays optical properties of 0.98/0.1 (α/ε) (Kirilov, Stefchev and Alexieva). However, this type of nanostructure is only stable to a maximum temperature of 300 °C (Katumba, Makiwa and Baisitse) (possibly 500 °C (Cuomo, Ziegler and Woodall)) because the atoms in the structure diffuse quickly and destroy the structure. Therefore, the incorporation of dendrites into this project will be challenging due to the operating conditions of the receiver.

3.3.3.2 Nanowires

Another promising surface structure is that of nanowires which is composed of wires that are 5 to 15 nm in diameter with lengths of about 250 to 350 nm. These nanowires show promising absorption characteristics because they absorb light well below 350 nm and transmit most light with longer wavelengths (Wu, Wu and Wei). With the correct substrate or sub-layers, transmitted light will be absorbed underneath the nanowires. Therefore,
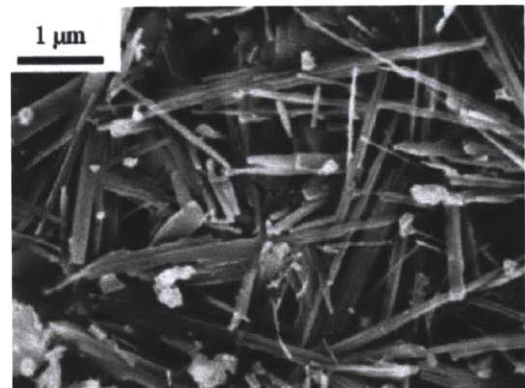
Figure 18-Nickel oxide nanowires (Yang, Sha and Ma)

nanowires are excellent when used as an anti-reflection layer because they possesses a high absorptivity and transmissivity. However, at high temperatures the nanowires begin to decompose back into its nanoparticle components which destroys the favorable optical properties. This decomposition begins at about 500 °C, and is complete at 600 °C (Wu, Wu and Wei). The disadvantage of using nanowires, which is similar to dendrites, is that they increase the surface's emissivity because of the increased surface area.

3.3.3.3 Cermets

Cermets are surface layers that have nanoparticles embedded in a dielectric matrix, and are commonly used with multi-nano-layered surfaces (Bostrom, Wackelgard and Westin). Some of

the surfaces described in the multi-nano-layered surfaces section (section 3.3.2) had cermet layers, and some of the cermet applications discussed here will be multi-nano-layered surfaces. Cermets are considered for solar receiver applications because they are tremendous absorbers. The absorption properties are a result of not only the material choice for the dielectric matrix and the nanoparticles, but also the interaction of the light at the interface between the nanoparticles and the dielectric matrix. The absorption in a cermet is due to the intrinsic absorption (related to the extinction coefficient of the material) and the interference-induced absorption (related to the refractive index). It is theorized that the main absorption in the cermet occurs from the embedded nanoparticles and not the surrounding dielectric matrix even though the dielectric matrix represents more of the surface by mass (Zhao and Wackelgard). This is because the small nanoparticles exhibit a non-scattering behavior that creates the favorable absorption properties (Bostrom, Valizadeh and Lu). The Effective Medium Theory is used to quantify the properties of cermet without knowing the microscopic structure because the properties can be estimated as intermediate between the nanoparticles and the dielectric material (Zhao and Wackelgard). The Effective Medium Theory can only be used if the nanoparticles are small enough that their surface effects are minimized the properties of the nanoparticles can contribute to the entire surface.

When studying the use of a cermet for implementation, cermets are never considered alone but rather as one layer among many. An excellent example is the multi-nano-layered surface of $Al_2O_3/Mo/Mo-Al_2O_3/SiO_2$ (Lanxner and Elgat). This surface demonstrates the general strategy of multi-nano-layered surfaces as described in section 3.3.2 with the Al_2O_3 being the diffusion barrier, Mo being the infrared reflector, $Mo-Al_2O_3$ being the absorber (cermet), and SiO_2 being the anti-reflection layer. This surface demonstrated optical properties of
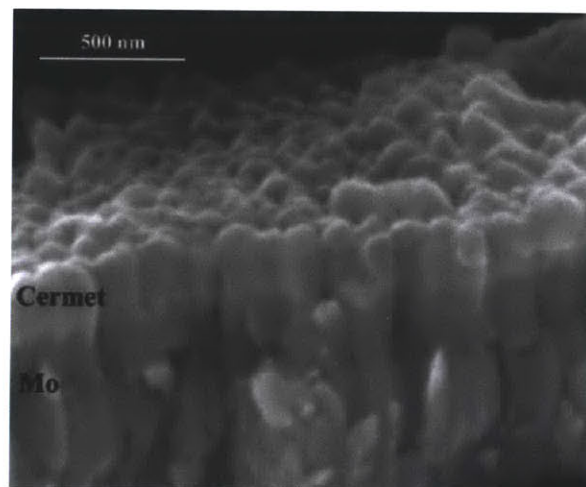
Figure 19-Image of the multi-nano-layered surface containing the cermet Mo-SiO2 (Esposito, Antonaia and Addonizio).

0.97/0.17 (α/ϵ), but was only stable to around 550 °C. A similar surface which can be seen Figure 19 is Mo/Mo-SiO$_{2H}$/Mo-SiO$_{2L}$/SiO$_2$ (Esposito, Antonaia and Addonizio). The H and L designate the relative concentrations of the Mo particles in the SiO$_2$ matrix. This surface demonstrated optical properties of 0.94/0.12 (α/ϵ) at 580 °C which is also its highest point of thermal stability. One last example of the use of a cermet in a selective surface is Pt/Pt-Al$_2$O$_3$/Al$_2$O$_3$ (Thornton and Lamb). It was stable to a slightly higher temperature of 600 °C with properties of 0.97/0.16 (α/ϵ). From these examples it is apparent that cermets have thermal stability problems in the operating temperature region for this project.

3.4 Solar Receiver Test Surfaces Selections

There were five surfaces selected for testing with two benchmarks, one candidate, and two validation surfaces. As discussed before, Inconel 617 was one of the benchmarks, and the other was chosen to be silicon carbide. The candidate surface was decided to be Inconel 617 with 150 nm platinum and 550 nm nickel oxide layers, and the two validation surfaces will be Inconel 617 with 150 nm layer of platinum and a plain nickel oxide sample. The rest of this section discusses the reasons for these surfaces being chosen.

3.4.1 Nickel Oxide on Platinum

A diagram of the selected candidate surface of Inconel 617 with 150 nm platinum and 550 nm nickel oxide layers can be viewed in Figure 20. Nickel oxide was chosen as the starting point for the design of the candidate surface because it was one of few materials found in the literature review that displayed stability at the operating temperatures (Kokoropoulos and Evans), and it demonstrated the best potential for favorable optical properties of the few materials that were stable (Kreith and Kreider). The thickness of 550 nm was chosen to match the wavelength of the light of highest intensity in the solar spectrum which can be seen in Figure 1. There was also an analysis performed to determine the optimum thickness which is described in the next section (Section 3.4.1.1).

One of the challenges of using nickel oxide is that nickel oxide and Inconel 617 are not thermally stable together because they are both nickel based which would cause diffusion to be high

between the layers. Therefore, a diffusion barrier would be needed between them. Platinum was chosen as that diffusion barrier because it does not react with either the nickel oxide or the Inconel 617 (Thornton and Lamb). It has also been demonstrated that platinum improves the optical properties of a surface when used as a substrate (Kokoropoulos, Salam and Daniels). In this case it will be a sub-layer and not a substrate, but it is still expected to improve the optical properties of the surface (this claim is also examined in the next section). A thickness of 150 nm was chosen for platinum because at this thickness the platinum serves the additional purpose of being an infrared reflector (Thornton, Penfold and Lamb).

This candidate surface selected is designed to be a crossover of many of the different types of selective surface discussed previously. The main absorber in the surface is a metal oxide in nickel oxide, but the sub-layer of platinum provides the multi-nano-layered coating aspect to the surface acting as both a diffusion barrier and an infrared reflector. This surface might be able to overcome the high temperature challenges of multi-nano-layered coatings because it is a more simplistic design with less surface interfaces. This surface also has the potential of adding a nanofeature during future testing. Nickel oxide has been shown to be able to create many different nanofeature including dendrites (Katumba, Mwakikunga and Lu), nanowires (Yang, Sha and Ma), and cermets (Katumba, Makiwa and Baisitse).

This surface was designed with the intent for it to be an elegant combination of many different types of selective surfaces. However, the thermal stability of this surface needs to be proven during testing. Therefore, a sample with just platinum on Inconel 617 will be tested to help determine if the platinum holds as a diffusion barrier. A plain nickel oxide sample was also tested to determine if nickel oxide displays the expected optical properties without the other sub-layers.

3.4.1.1 Essential Macleod Software

In order to validate the chosen thicknesses for the platinum and nickel oxide layers on the chosen selective surface, Dr. Jong Won Kim investigated the predicted optical properties of the surface with different thicknesses, and his work is summarized in this section. A computer software

program called *Essential Macleod* was used to predict the optical properties. The software operates by allowing the user to input surface design, and then based on the materials refractive index and extinction coefficient determines the optical properties of the surface.

In this analysis, the two major parameters under investigation for their influence on the optical properties were the thickness of the nickel oxide layer, and the presence of the platinum layer. A diagram of the two samples investigated is shown in Figure 20. The nickel oxide layer in each of the samples was varied from 400 nm to 700 nm in 50 nm steps, but the thickness of the platinum layer remained fixed at 150 nm in the one sample.
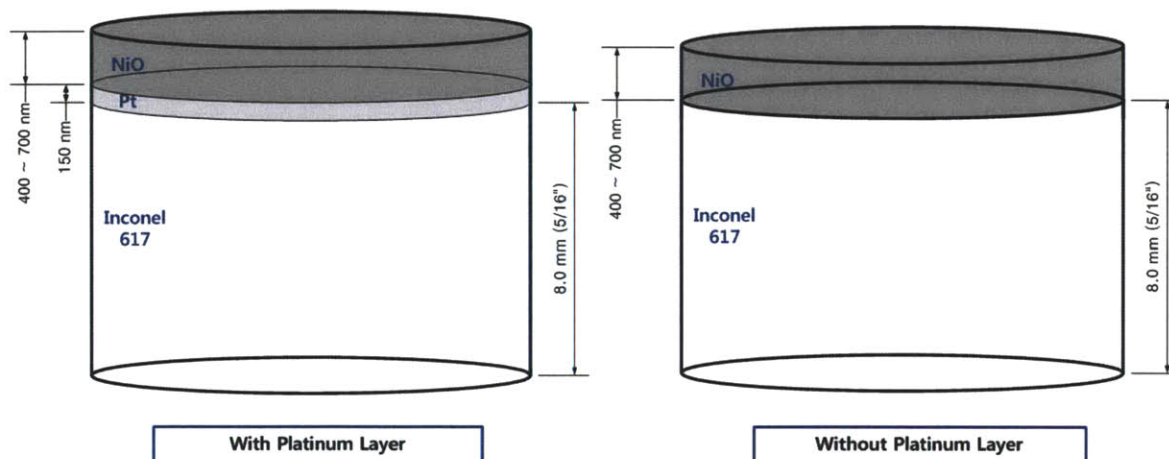
Figure 20-Schematic diagram of the two surfaces investigated using the Essential Macleod software.

The results of absorptivity (and emissivity) versus thickness of the nickel oxide layer is shown in Figure 21. Data from the literature review is included in Figure 21 for comparison, but it should be noted that the data is for nickel oxide on a platinum substrate rather than a platinum sub-layer. The analytical results have almost the same average emissivity in the infrared region as the previous research suggests. In Figure 21 it can also be seen that the absorptivity of the samples with a platinum layer is much higher than without a platinum layer. This is due to the increased reflections of the light by the platinum layer that allows for increased path lengths in the nickel oxide which increases the total absorptivity.

NiO thickness : 400 nm	NiO thickness : 450 nm
NiO thickness : 500 nm	**NiO thickness : 550 nm**
NiO thickness : 600 nm	NiO thickness : 650 nm
NiO thickness : 700 nm	Previous research (Kokoropoulos and Evans)
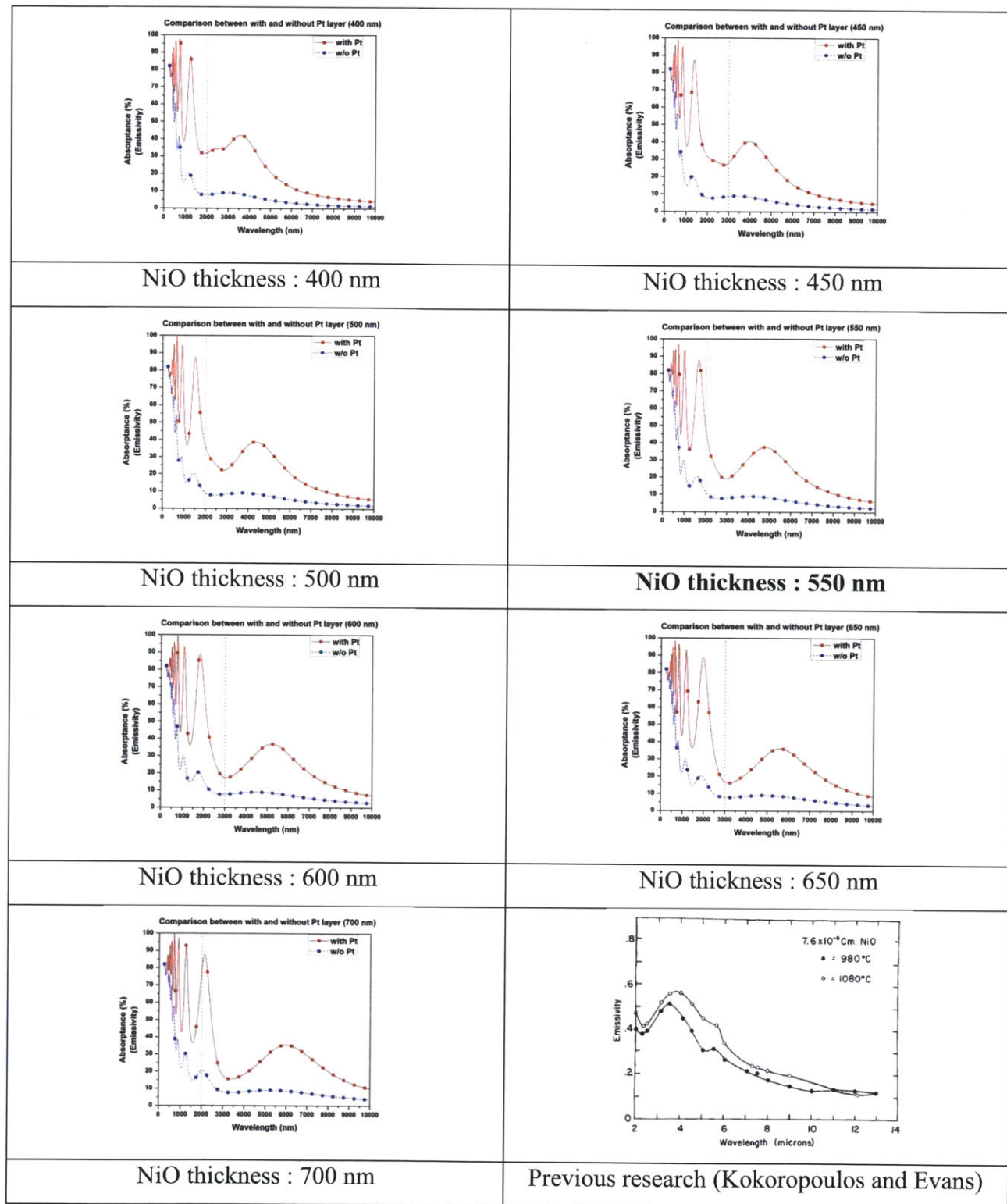
Figure 21-Spectral absorptivity/emissivity obtained from the Essential Macleod software for varying thicknesses of nickel oxide for samples with and without the platinum layer compared to previous research.

While the graphs in Figure 21 provide valuable qualitative information, in order to determine the optimum thickness of the nickel oxide there must be a quantitative analysis. Table 4 contains the necessary information for this analysis and was obtained using methods fully described in section 5.1.2.1. The most important parameter in Table 4 is the thermal efficiency found in the last column. This claim is validated in section 5.1.2.1, but Table 4 indicates that the selection of the thickness of the nickel oxide is not a critical parameter for this surface because the thermal efficiency changes very little over the thickness range studied. Therefore, the investigation using the *Essential Macleod* software validates the chosen dimensions for the 617/Pt/NiO surface chosen for testing.

Nickel Oxide Thickness	Average Absorptivity (α)	Average Emissivity (ε)	Selectivity Ratio (α/ε)	Absorptance (kW)	Emittance (kW)	Net Power (kW)	Thermal Efficiency (%)
With platinum layer							
400 nm	0.7028	0.3182	2.2089	351.40	63.00	288.41	0.577
450 nm	0.7030	0.3189	2.2042	351.50	63.15	288.35	0.577
500 nm	0.7083	0.3251	2.1788	354.16	64.37	289.79	0.580
550 nm	0.7246	0.3306	2.1919	362.29	65.45	296.84	0.594
600 nm	0.7326	0.3454	2.1212	366.29	68.38	297.91	0.596
650 nm	0.7376	0.3557	2.0737	368.78	70.43	298.36	0.597
700 nm	0.7461	0.3645	2.0467	373.05	72.18	300.87	0.602
Without platinum layer							
400 nm	0.3610	0.0739	4.8868	180.49	14.68	165.80	0.332
450 nm	0.3847	0.0807	4.7668	192.35	16.04	176.31	0.353
500 nm	0.4049	0.0875	4.6259	202.46	17.40	185.06	0.370
550 nm	0.4287	0.0944	4.5406	214.35	18.77	195.58	0.391
600 nm	0.4509	0.1013	4.4495	225.46	20.14	205.32	0.411
650 nm	0.4708	0.1083	4.3478	235.38	21.52	213.86	0.428
700 nm	0.4897	0.1152	4.2514	244.86	22.90	221.97	0.444

Table 4-Predicted surface properties for the different surfaces examined using the Essential Macleod software.

3.4.2 Silicon Carbide

Silicon carbide was chosen as a surface for testing because it displays many black body properties. A black body surface was needed as a benchmark, and silicon carbide is a readily

available and cheap material to use. The other option was to use carbon nanotubes which are expensive and difficult to manufacture. At this stage of the project, an excellent black body surface was not needed, and silicon carbide provides the needed properties without any hassles.

3.5 Geothermal Antifouling Test Surfaces Decision Criteria

Similar to the solar thermal receiver experiment, the choice of coatings to test is an important part of geothermal antifouling experiment, and this section will outline the basis for the criteria deemed important. The two main factors are that the types of surfaces tested need to provide a diverse mix of technologies that allow for comparisons and conclusions to be drawn, and the ability for the surfaces to be practically applied to the samples to allow for an adequate sample to test. The testing strategy of the samples will also be outlined to provide a basis for these main factors.

3.5.1 Testing Strategy

The testing strategy to determine the antifouling potential of each coating involved the use of the Geothermal Experimental Antifouling Loop (GEAL). Samples were inserted into the loop for at least four weeks while a fluid containing hydrogen sulfide was passed through them in turbulent flow. The samples were weighed both before and after to determine the percent weight change. To standardize the results across all the trials, a carbon steel sample was included in each round of testing as a control, and the figure of merit will be the percent weight change relative to the carbon steel. This is extremely important because it will be impossible to keep the conditions of the test exactly the same from trial to trial. This is due to the fact that the hydrogen sulfide concentration and pH are continually changing values which are quite difficult to keep constant without active chemistry control which was not applied to the GEAL. Thus, the carbon steel samples will be considered a benchmark across all trials.

The coatings are always applied to 1010 carbon steel which is similar to the steel used in the DCT. Most of the coatings were prepared on 6' long ¼" OD carbon steel tubes sent to the vendors after our preparation. Each carbon steel sample was cleaned with acetone on the outside to remove dust and debris. The inside was cleaned by pulling a ¼" brush through the tube and

running ethanol through to remove the debris. The samples were allowed to air dry after these procedures. Once sent to the coating manufacturer, the samples were prepared differently based on the coating process. After testing, the outside of the samples were cleaned again using acetone to remove the deposits from the chilled water. The inside of the tube remained untouched. The samples were always allowed to air dry before they were weighed.

3.5.2 Types of Coating

It was critical to the experiment to choose a diverse set of samples that would allow comparisons to be made. This required the categorization of the samples to determine the differences between them. There are several factors that can be used to define each of the coatings. Each of the coatings were classified into either commercial or non-commercial coatings. Commercial coatings were tested to provide a comparison to current industry antifouling products, but these coatings tended to not include nanotechnology. The non-commercial coatings were coatings specifically created for this experiment, or were being developed for a different application. Secondly, the coatings can be separated into coatings that utilize nanotechnology and those that do not. While nanotechnology is the focus of this project, there are many other potential solutions that utilize other technologies, and these were tested to provide a comparison between nanotechnology and others. This leads to the final classification of the coatings which is the manner in which the coating prevents fouling. Many of the coatings utilize micro-technology or chemistry to obtain their desired properties, and still others involve the use of layers to separate the steel from the fluid. The beneficial surface properties that lead to antifouling and anticorrosion with reference to nanotechnology will be covered in section 3.6.

3.5.3 Manufacturing Potential

One of the major requirements of the tested coatings was their ability to be applied to both the GEAL and the DCTs. Therefore, the manufacturer had to have the capacity to coat both a ¼" tube and tubes up to 12 m long. The potential coating of a 0.18" ID tube that will be used in the GEAL depends on the coating technique. Some coating techniques involved the use of a nozzle that was inserted into the center of the tube and sprayed on the coating. This method would be ineffective for a ¼" tube because the nozzle would be too big to fit in the tube. For application

to the DCTs, tubes of approximately 12 m would need to be coated. The inner diameter of these tubes is 0.83" which allows for the application of many techniques so the hindrance to application would be the size of the company's facilities. While most vendors did not have the capacity for tubes this long, interest was shown in adaption to the needs of ENEL for a large order such as the one for the DCTs.

3.6 Antifouling Surface Options

As discussed in the background section (2.3.3.3), the fouling of the DCT heat exchanger likely occurs in conjunction with the corrosion of the pipes. Thus, an effective coating must prevent both corrosion and fouling, and it is possible that a coating or nanosurface that prevents corrosion of the pipe may achieve the antifouling properties desired. There have been many different research initiatives with the goal of finding a solution to corrosion, but it seems to be too complex a problem to warrant a simple solution. However, in recent years nanosurfaces have been investigated for their potential uses in preventing corrosion. Thus, this section is a summary of the different nanosurfaces that have been under investigation for corrosion resistance and potential fouling resistance. It will be demonstrated that the three main beneficial properties that the nanoparticles enhance are the surface's uniformity, hydrophobicity, and hardness.

3.6.1 Carbon Nanotubes

The number of potential applications of CNTs is tremendous, and one of those applications is in coatings to prevent corrosion. One theory is to use the electronic properties of the CNTs to create an electronic barrier between the fluid and metal surface. Similar to a semiconductor, a p-n junction is created using the CNTs which allows for the current to only flow in one direction. When the p-junction is next to the metal, the CNTs do not allow charge to travel from the fluid to the metal which prevents the corrosion and degradation of the metal (Sreevatsa and Grebel).

There is another coating using CNTs that takes advantage of their mechanical properties as well as their electronic ones. It has been demonstrated that a thin layer of pure nickel on carbon steel can help prevent corrosion, but the addition of CNTs to the nickel layer produces a superior anti-corrosion coating (Chen, Chen and Xiao). The CNTs protect the surface of the nickel from

wearing and corroding by filling in defects, such as crevices or gaps, on the surface that would otherwise allow for the initiation of corrosion due to the penetration through the nickel. These defects are larger than a micron, and without the CNTs there is nothing in the system that could fill a gap of this size which results in the penetration of the fluid to the carbon steel. The electronic properties of the CNTs are also utilized because their standard potential is higher than that on nickel which increases the corrosion potential to a less negative value which encourages homogenous corrosion. Therefore, corrosion will be delayed because localized areas will not be compromised leading to the demise of the entire system. The entire surface will have to be worn down uniformly which requires more time. However, this only applies if the CNTs are deposited uniformly across the nickel which can be done by electrodeposition.

3.6.2 Hydrophobicity

One of the major applications that nanosurfaces have been investigated for is the creation of a surface with hydrophobic properties, or a resistance to wetting. It has been shown that hydrophobic properties cause a surface to be anti-fouling, self-cleaning, anti-fungal, anti-algal, and easy-flushing (Lin, Yeh and Liu). All of these properties are very beneficial for a heat exchanger. Hydrophobic surfaces are beneficial for corrosion prevention because they allow for less interaction between the fluid and the surface which reduces the flow of ions. Consequently, many of the coatings researched for anti-corrosion applications are chemicals that display hydrophobic properties (Telegdi, Rigo and Kalman).

An example of the impact of a surface's hydrophobicity on corrosion resistance is when cerium is added to a poly-acetamide-acetoxyl methyl-propylsiloxane (PAAMS) polymer. The addition of 3 weight percent cerium increased the contact angle by 13° and increases the corrosion resistance from 10 hours to 768 hours (T. Sugama). One of the reasons for this is that the Ce^{3+} ion does not interact with Cl^- which helps maintain the surface integrity in Cl^- solutions. While many of these chemical coatings exist due to the wide variety of metals that face corrosion problems, the one of most interest is the chemical coating that is applied to zinc. Zinc is important because it's often used to galvanize steel in an attempt to prevent corrosion, but it merely delays the eventual corrosion of the steel. The application of a coating to the zinc that can delay the corrosion of the steel even further is of high interest. A perfluorosilane polymer

has proven to be an effective anti-corrosion coating because it displays hydrophobic properties. This is due to the presence of fluorine which lowers the surface free energy, and has the largest electronegativity of all atoms. It was demonstrated in a laboratory test that it required 29 days to corrode the zinc to the same degree as 1 day without the coating (Liu, Szunerits and Xu).

3.6.3 Nanofibers

The use of polyaniline nanofibers have been shown to be very beneficial corrosion inhibitors. The benefits of the nanofiber structure can be seen when compared against aggregated polyaniline which is polyaniline in groups or clusters. The main difference is that the nanofibers form a more passive layer on the carbon steel that consists of α-Fe_2O_3 and Fe_3O_4. The stronger bands in the nanofibers allowed for the layer to be more passive than the aggregated polyaniline. Another cause resulting in a more passive layer is the increased surface area of the nanofibers that allows for better adhesion to the carbon steel. Therefore, polyaniline demonstrates anti-corrosion properties which are greatly enhanced by the nanofiber structure. They can be synthesized by interfacial polymerization, and provide excellent corrosion protection if they form an even compact coating (Yao, Wang and Ye).

3.6.4 Nanoparticles mixed in Anti-corrosion layers

Nanoparticles can also provide major anti-corrosion advantages when applied to traditional anti-corrosion coatings. The creation of an effective anti-corrosion coating is extremely challenging because if the coating fails in one location then the entire coating becomes nullified. The metals substrate will corrode quickly in that location, potentially blistering, and eventually will breach the outside of the metal. Nanosurfaces are beneficial in this respect because they encourage the creation of a uniform surface by filling in the gaps. A uniform surface is less likely to corrode in one location, and will only fail when the entire surface has been worn away which significantly lengthens the time of corrosion protection.

There are quite a few examples of nanoparticle-surface combinations that display the effect nanoparticles have on the anti-corrosion properties. The application of montomorillonite (MMT), a clay, to polyphenylenesulfied (PPS), a well known thermoplastic, prevents the corrosion of

carbon steel much longer than PPS alone (T. Sugama). The nanoparticles not only create and help maintain a uniform surface, but also prevent the penetration of electrolytes to the carbon steel. The strong bonds between the PPS and MMT nanoparticles create a hard, resistant surface. Another example is the addition of SiO_x to current anti-corrosion paints. Current paints are used to provide a cheap barrier between the metal and the environment, but the addition of the SiO_x nanoparticles increases the hardness, increases the hydrophobicity, and decreases the moisture penetration (Lin, Yeh and Liu). The increased hardness makes the surface easier to clean without removing the paint. The decrease in moisture penetration is due to the uniformity in which the nanoparticles disperse into the paint. The nanoparticles settle uniformly because they are arranged with the same orientation (referred to as a self-assembly monolayer) from the initiating reaction which takes advantage of the SiO_x having a repulsive force due to the static electricity between them. This repulsive force prevents the accumulation of nanoparticles in a single region.

3.7 Geothermal Antifouling Test Surface Selection

There were a variety of coatings tested that were obtained from four different groups that were collaborators on this project which were SilcoTek, Curran International, and MIT Professor Schuh and his company Xtalic. These coatings can be split into the three main categories of traditional coatings, nanoengineered coatings, and alternative coatings. The traditional coatings were the Silcolloy 1000 coating, the Dursan coating, and the Curran 1000 coating. The nanoengineered coatings were the Curran 1000 coating with nanographene, the Curran 1000 coating with nanographene and nanosilicon carbide, and the XPROTECT coating. The alternative coatings were the Curran 1000 coating with PTFE, the Curralon coating with PTFE, and the Curran 1000 coating with self healing properties. The following is a more detailed description of the coatings, but it should be noted that the specifics of some of the coatings are company proprietary information so the following is the best information available.

3.7.1 Traditional Coatings

The Silcolloy 1000 coating is an inert, corrosion resistant coating of amorphous silicon diffused into a substrate that was developed by SilcoTek. Silcolloy 1000 is deposited using CVD which leaves the coating as 1 to 2 microns thick with a contact angle between 15° to 35°. It has been

demonstrated to reduce the corrosion of 316 stainless steel by an order of magnitude. This coating was tested on the inside of a ¼" 1010 carbon steel tube, and the product data sheet can be viewed in the Appendices.

The Dursan coating is a carboxysilicon coating created by SilcoTek that demonstrates increased moisture and wear resistance. Dursan is designed for application to stainless steel in aggressive environments such as ones with hydrogen sulfide. This coating was tested on the inside of a ¼" 1010 carbon steel tube to determine its potential as a cheaper alternative to stainless steel, and the product data sheet can be viewed in the Appendices.

The Curran 1000 coating is a coating developed by Curran International that is specifically designed for heat exchanger tubes. It is an advanced epoxy with organic and inorganic components that is very versatile and will be modified a few times for the tests. An epoxy is advantageous for this application because the coating process involves the mixing of two parts that solidify due to a chemical reaction in the tube which makes application simple. One of the ingredients of the Curran 1000 is micrographene particles which is important to note. This coating was tested on the inside of a ¼" 1010 carbon steel tube, and the product data sheet can be viewed in the Appendices. It should also be noted that this coating was tested twice because the first time it was determined that the mixture was incorrect which resulted in a flawed coating.

3.7.2 Nanoengineered Coatings

The Curran 1000 coating with nanographene replaces the micrographene particles that are used normally with the Curran 1000 with nanoparticles which is anticipated to increase the thermal conductivity of the coating. The comparison between this coating and the Curran 1000 will demonstrate the importance of the size of the particles in the coating. This coating was tested on the inside of a ¼" 1010 carbon steel tube.

The Curran 1000 coating with nanographene and nanosilicon carbide will be tested for a comparison with the Curran 1000 coating with nanographene for effect of the addition of nanosilicon carbide. Silicon carbide is of interest to add to the mixture because it is expected to

increase the heat transfer capability and wear resistance of the coating which is applicable to the heat exchanger application. This coating was tested on the inside of a ¼" 1010 carbon steel tube.

XPROTECT is an electroplated coating of nickel and tungsten that was developed by Xtalic Corporation in conjunction with MIT's Professor Schuh that increases the corrosion and wear resistance of a surface. XPROTECT is a nanocrystalline Ni-W alloy that is unique because of the properties it possesses due to the use of the pulse-reverse electrodeposition technique used to manufacture it. XPROTECT is encouraging for this application because the corrosion resistance will be beneficial to prevent fouling, and the wear resistance and hardness will be imperative to allow for easy cleaning of the heat exchanger. The hardness of XPROTECT can easily be increased to a desired value by applying a mild heat treatment which relaxes the grain boundaries. XPROTECT has already been applied to the field of gravure printing where the letters are exposed to ink followed by contact wear as the ink is applied to a surface. XPROTECT increased the lifetime of the printer by an order of magnitude. This coating will be tested on the outside of a 6" long 3/8" diameter rod with coating thicknesses of 25 and 50 microns (Jones, Hamann and Lund).

3.7.3 Alternative Coatings

The Curran 1000 coating with polytetrafluoroethylene (PTFE) will be tested to determine the antifouling capability of PTFE in this environment. PTFE has demonstrated beneficial properties for the prevention of silica scaling in geothermal energy systems by preventing the silica deposits to adhere to the surface (Sugama and Gawlik). This coating was tested on the inside of a ¼" 1010 carbon steel tube.

The Curralon coating with PTFE will allow for a comparison to the Curran 1000 with PTFE to assess the importance of Curran 1000 as a substrate. Curralon is a thermoplastic which means that it must be melted onto the tubes which is disadvantageous for this application because it requires heating the tubes to high temperature. This coating was tested on the inside of a ¼" 1010 carbon steel tube.

Curran 1000 with self healing properties is a different coating design that will fill any holes in the coating created by corrosion. The Curran 1000 has boehmite, an aluminum oxide hydroxide, mixed in with it that captures water and expands which will fill the gaps. This coating was tested on the inside of a ¼" 1010 carbon steel tube.

4. Methodology

A basic understanding of the fundamental processes and equipment capabilities is required to correctly interpret the results of this study. This section will review the fundamentals of the different nanosurface fabrication techniques along with the basics of the instruments utilized and how they are applied. A review of the Geothermal Experimental Antifouling Loop (GEAL) will also be presented.

4.1 Surface Fabrication

The first step of the testing process involves the fabrication of the surfaces. For some of the samples, this involves the formation of layers that are nanometers in thickness. The method of deposition is extremely important because it has a profound effect on the produced surface which in turn drastically changes the properties which are of interest in this study. Therefore, the choice of the deposition method must be considered along with the choice of which surfaces to test. The deposition methods to choose from are physical vapor deposition (PVD), chemical vapor deposition (CVD), sol-gel deposition, and electroplating. Each produces surfaces with slightly different properties, but these differences are difficult to predict without testing.

4.1.1 Physical Vapor Deposition

Physical vapor deposition (PVD) is a process by which a thin film of material is deposited on a substrate by the accumulation of atoms from a source above the substrate. Both the substrate and a sheet composed of the atoms which are to be deposited are inserted into a vacuum with the substrate placed below the sheet. An electric field is then applied over the whole system, and ions are created in the system between the substrate and the sheet. The ions follow along the electric field and collide with the sheet which releases a few atoms. This process is known as sputtering. These atoms are neutral so the electric field does not influence their path, and they fall onto the substrate and deposit. Over time this process forms a thin layer that can be can of any thickness depending on the length of time the deposition is allowed to occur and the rate of ion creation in the system. This process is known as physical vapor deposition by sputtering which is the most common type of PVD.

4.1.2 Chemical Vapor Deposition

Chemical vapor deposition (CVD) involves the insertion of a substrate into a chamber filled with typically two gases. The gases are chosen so that the there will be a chemical reaction between the two that will result in the desired deposition only in the presence of a required activation energy. Therefore, the substrates are at an elevated temperature so that all of the reactions in the system are occurring on the surface of the substrate and depositing the desired atoms. The critical aspect of this technique is to choose two gases that will have the desired effect. As an example, if it was desirable to deposit tungsten on a surface, then the gases of choice would be tungsten fluoride and hydrogen. The reason of this choice is best seen in the following equation.

$$WF_6(g) + 3H_2(g) + Q \rightarrow W(s) + 6HF(g)$$
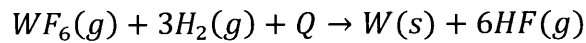
In the presence of some activation energy (Q), which is provided by the substrate at an elevated temperature, tungsten will be formed on the surface as hydrogen fluoride will leave the system. Often the surface is heated to a high enough temperature to allow for the diffusion of the atoms into the surface of the substrate.

4.1.3 Sol-gel

The sol-gel deposition technique involves the creation of a gel from chemical reactions in aqueous solutions that is then dried to form a thin film. While there are several variations on this technique, surfaces for solar receiver applications tend to use a solution of metal alkoxides and water in an alcoholic solvent (Phalippou). Hydrolysis occurs where the water present splits into H+ and OH-, and this allows for a chemical reaction that forms a metal oxide. This forms a network of the metal oxide in the solvent to create a gel. The solvent is then removed by heating the gel. In some cases when alcohol is used, the gel is kept at about 120 °C to allow for quick evaporation of the alcohol, and then calcined at about 750 °C to allow for a structural change of the metal oxide to get the remaining alcohol out of the structure (Yang, Sha and Ma). This also causes the metal oxide structure to become denser and less porous.

4.1.4 Electroplating

Electroplating is a deposition process that involves the insertion of a substrate and a strip of the metal to be deposited into a solution. A current is run through the solution with the substrate acting as a cathode and the metal acting as an anode. Since electrons will be travelling from the cathode to the anode, positively charged metal ions will travel from the anode to the cathode. When the ions reach the cathode they will deposit on the surface creating a thin film. The advantage of using electroplating is that it requires far less expensive equipment when compared to PVD or CVD, but the deposition is drastically effected by the chemistry of the solution. Typically, the solution contains an acid, a compound with the metal to be deposited, and possibly a salt (Blum and Hogaboom). Therefore, it requires a tremendous amount of research and precision to produce the desired surfaces using this method.

4.2 Reflectometer

A reflectometer measures the reflectivity of radiation off of a surface. The reflectivity data is highly valuable because the absorptivity can be calculated since it is known that there is no transmittance in the system, and from the absorptivity the emissivity is known (via Kirchhoff's Law, Section 2.2.7) at the same wavelength. Therefore, a reflectometer will be used to measure the spectral reflectivity across all of the wavelengths of interest. The equipment necessary for these measurements is expensive and not available at MIT which led to the hiring a contractor to perform the required measurements.

In order to obtain the reflectivity for all of the necessary wavelengths, two reflectometers were required. They are the Cary-Integrating Sphere Reflectometer which measures reflectivity between 0.2 μm and 2.0 μm, and the SOC-100 Infrared Reflectometer which measures between 2.0 μm and 26.0 μm. Each operate using similar principles, but require different geometries to produce the measurements of the correct wavelength.

The Cary-Integrating Sphere Reflectometer is used to measure the reflectivity in the near-ultraviolet, visible, and near-infrared regions of the spectrum. The geometry of the system can be seen in Figure 22. The instrument operates by having a 55 watt halogen bulb inside a 9"

hollow sphere that is coated with Halon (G-80 tetrafluoretheylene). The sample also resides inside the sphere, but is separated from the halogen bulb by a diffuse reflector. The geometry is such that the light must be reflected by the inner surface of the sphere at least twice before it can interact with the sample. This creates an environment that is uniformly lit from the perspective of the sample (Surface Optics Corporation). There are two small openings in the sphere that allow the light to be transmitted to a device known as the Cary Model 14 Spectrophotometer. The two slits are positioned so that one light source comes from the sample, and the other comes from the surface of the sphere in the uniformly lit region. Therefore, to measure the reflectivity the intensity of the light from the sample is divided by the light from the sphere surface because the light at the surface is equivalent to the incident intensity on the sample. The incident angle is changed by adjusting the orientation of the sample.
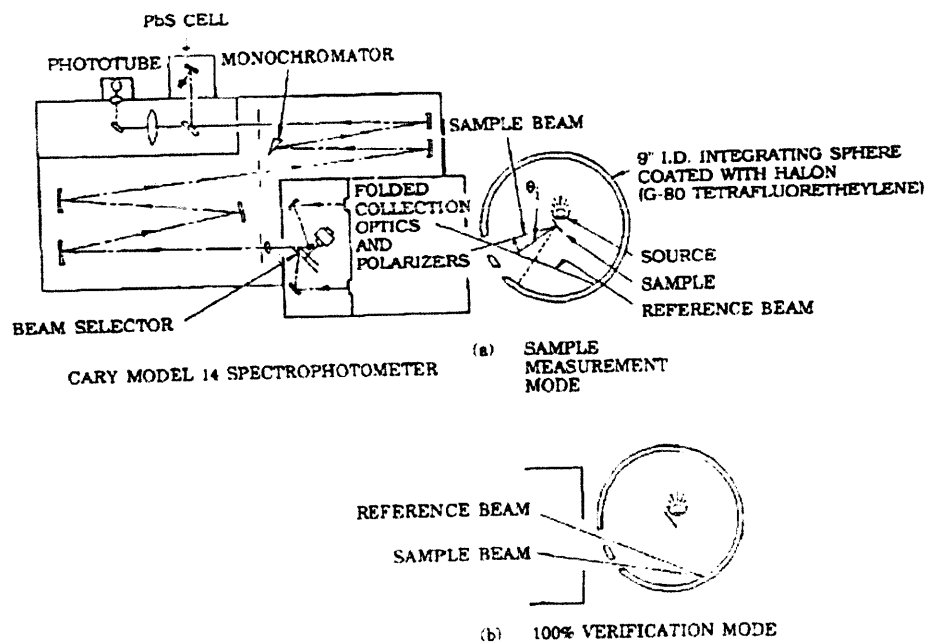
Figure 22-A schematic diagram of the Cary-Integrating Sphere Reflectometer and the Cary Model 14 Spectrophotometer. Image taken from the report provided from Surface Optics Corporation.

The Cary Model 14 Spectrophotometer is designed to take the two incoming beams of light and measure their intensities. This is accomplished by use of a mirror that is designed to select one of the beams of light. This light is then sent through a monochromator to separate the different wavelengths, and then the light is directed at the appropriate detector based on its wavelength. Radiation between 0.3 μm and 0.8 μm require a photomultiplier tube detector, and a lead sulfide

cell detector is required for radiation between 0.8 μm and 2.0 μm. Radiation between 0.2 μm and 0.3 μm requires a different photomultiplier tube than the one used for radiation between 0.8 μm and 2.0 μm, and the use of a deuterium lamp instead of the halogen bulb (Surface Optics Corporation). Therefore, the Cary Model 14 Spectrophotometer measures the intensities at a variety of wavelengths from each beam and divides them to obtain the reflectivities.

The SOC-100 Infrared Reflectometer measures the reflectivity of a sample beyond the near-infrared regions of the spectrum. The geometry is quite different from that of the Cary-Integrating Sphere Reflectometer, and can be seen in Figure 23. The theory behind the geometry is that any radiation produced at a focus of an ellipse must travel through the other focus after reflecting off the surface of the ellipse. Therefore, a point source of light at one focus will result in uniform illumination of the ellipsoid from the perspective of the sample which is placed at the other focus. A sophisticated laser verification system is used to ensure the sample is placed correctly. Similar to the Cary-Integrating Sphere Reflectometer, the SOC-100 Infrared Reflectometer also requires uniform illumination of a sphere, or in this case an ellipsoid, to measure the reflectivity. A mirror is placed in the ellipsoid that can be moved to select

(a) Top View.

(b) End View.

Figure 23- A schematic diagram of the SOC-100 Infrared Reflectometer. Image taken from the report provided from Surface Optics Corporation.

the reflected radiation to be measured, and directs it to a series of mirrors that direct the radiation out of the ellipsoid and to a 750 FTIR Spectrometer which measures the intensity. The 750 FTIR Spectrometer operates in a similar fashion to the Cary Model 14 Spectrophotometer, but is designed for wavelengths beyond the near-infrared (Surface Optics Corporation). The reference

intensity is measured using a standardized sample of known reflectivity which in this case was evaporated gold standard on a smooth fused silica substrate.

4.3 Infrared Camera

The use of an infrared (IR) camera will allow for a means of visibly comparing the emissivity of two samples. The IR camera measures the IR signals from 3 to 5 microns which unfortunately does not cover the entire spectrum upon which the surfaces will be emitting, but is enough to compare two samples. The computer software used with the IR camera also has the ability to determine the number of counts coming from different regions. Therefore, there is a quantitative means for comparing two samples. Figure 24 below is an example of the type of image that can be obtained using the IR camera. The two samples in this picture display comparable emissivities, and thus have similar illumination in this image.

To obtain data such as Figure 24, the testing procedure required diligence from all parties involved due to the high cooling rate of the samples. The block of alumina holding the samples was inserted into the furnace, and the furnace was set at 1000 °C. It was required to create a block of alumina that the samples could be inserted into because they would cool too fast to obtain data in the desired range without insulation. Each sample had a thermocouple spot welded to its surface, and in the cases of surfaces with deposited films it was necessary to scrap the part of the film off to allow for the thermocouple to be spot welded. The thermocouple was spot welded to the same location near the periphery on each sample. After the samples reached 1000 °C, the samples were taken from the furnace and placed on an alumina block on the floor under the IR camera which was supported approximately 4 feet above the ground. The alumina block was critical for this step because it shielded the samples from the forced convective cooling of the air as it was moved. Once the samples were in place, they were allowed to cool from approximately 900 °C to 600 °C while their temperatures were recorded with the thermocouples, and the IR camera recorded a video of their IR radiation over time.
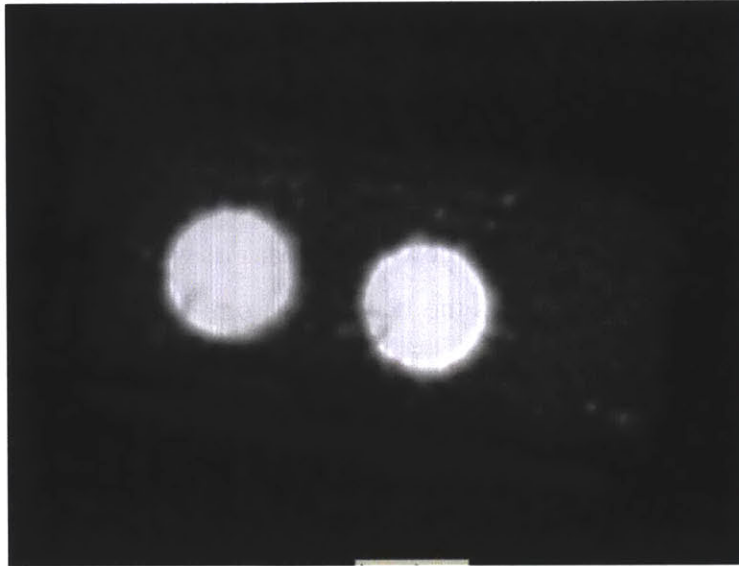
Figure 24-Image taken with the IR camera of a nickel oxide/platinum surface on Inconel 617 and an Inconel 617 surface in an alumina block

While this method does not provide a means to precisely measure the emissivity, it does provide a method to compare the emissivities of two samples against each other. This allows for confirmation of the trends established from the data received from the reflectometer.

4.4 Scanning Electron Microscopy

A major aspect of this study involves quantifying and verifying that the surfaces tested have the characteristics and composition intended. To fully quantify a surface and all of the nuances that compose its structure requires the use of many instruments, but the analysis for this study can be shortened because only certain features require examination. A scanning electron microscope (SEM) will be used to perform this function because of its capabilities to produce images on the micrometer scale, and quantify the elemental atomic concentrations in the system. Due to the high degree of importance placed on the analysis from the SEM, an understanding of its inner workings is appropriate.

The essence of how the SEM operates involves the bombardment of a surface with electrons to produce secondary and backscatter electrons that are measured by a detector to produce an image. The production of secondary and backscatter electrons varies according to the surface morphology and atomic number which allows for the detector to record different electron

intensities and produce an image representative of the surface (Goldstein, Newbury and A. D. Romig). The electron beam focuses on a single point on the surface while the detector records the number of secondary and backscatter electrons produced, and then the beam is moved to another point while the detector records the electron readings at this new point. The intensity

from each point is represented by a pixel on the screen which as a whole produces an image of the area rastered by the electron beam. The magnification of the image will be increased when the points on the surface recorded are closer together resulting in less area being covered. Specifically, the magnification is defined as the ratio of the area of the viewing screen to the area of the sample surface covered by the electron beam (Goldstein, Newbury and A. D. Romig). The electron beam is produced by an electron gun, and is focused using electron lenses which are magnetic fields

Figure 25-Diagram of the main process in a SEM starting with the production of electrons to the creation of an image (Goldstein, Newbury and A. D. Romig).

designed to reduce the diameter of the beam. The diameter of the electron beam can be approximately 10 nm on most SEMs (Goldstein, Newbury and A. D. Romig). The direction of the beam is slightly modified by four deflection coils that allow for movement/rastering of the beam from one point to another to create the pixel measurements. The generated electrons are collected by an Everhart-Thornley electron detector that determines the intensity of the measurement, and these measurements are used to create an image. The E-T detector operates by accelerating the electrons into a scintillator where the electrons interact with a material to produce light. The light travels into a photomultiplier tube (PMT) that creates an electrical signal of varying amplitude based on the amount of light entering the PMT. Thus an image can be created from many electrical signals representing different points on the surface of the

specimen.

SEMs also have the capacity to determine the elemental composition of a sample from use of an Energy-Dispersive X-Ray Spectrometer (EDS). An EDS operates by using a lithium-drifted silicon Si(Li) solid-state x-ray detector to measure the X-rays produced by the sample surface as a result of electron bombardment (Goldstein, Newbury and A. D. Romig). The Si(Li) detector has a Si(Li) crystal that absorbs the x-rays and produces an electron that is swept away due to a voltage applied across the crystal. This creates an electrical pulse which is converted by a pre-amplifier and amplifier before being sent to a computer x-ray analyzer (CXA). The computer records the intensity of the counts across a range of different voltages, and produces a histogram. This allows for identification of the elements present because the voltage pulse is proportional to the energy/wavelength of the X-ray produced by the sample (Goldstein, Newbury and A. D. Romig). The X-rays produced by elements as a result of electron bombardment are known from previous experiments. Therefore, the CXA is able to calculate which elements are present and in what quantities based on the energy and intensity of the voltage peaks.

To demonstrate the capabilities of the SEM, the results obtained from the analysis of Inconel 617 will be shown below. After the manufacturing of the Inconel 617 samples, the SEM was used to verify that the composition of the sample was within the accepted tolerances. Figure 26 demonstrates the results of an EDS analysis on the specimen, and while it is not within the exact specifications of Inconel 617 of 44.5 % Ni (minimum), 20-24 % Cr, 10-15% Co, 8-10% Mo, 0.8-1.5% Al, 3% Fe (maximum), and 1% Mn (maximum) (Special Metals Corporation), it is within experimental error. Figure 27 is an image of morphology of Inconel 617 after it has been oxidized. Prior to oxidation, this sample was flat due to the polishing of the sample so most of the features are due to the oxidation of the surface.

Element	Weight%	Atomic%
AlK	0.77	1.69
CrL	22.02	24.91
MnL	1.42	1.52
FeL	0.15	0.15
CoL	17.23	17.20
NiL	48.92	49.01
MoL	8.48	5.20
WM	1.01	0.32
Totals	100.00	
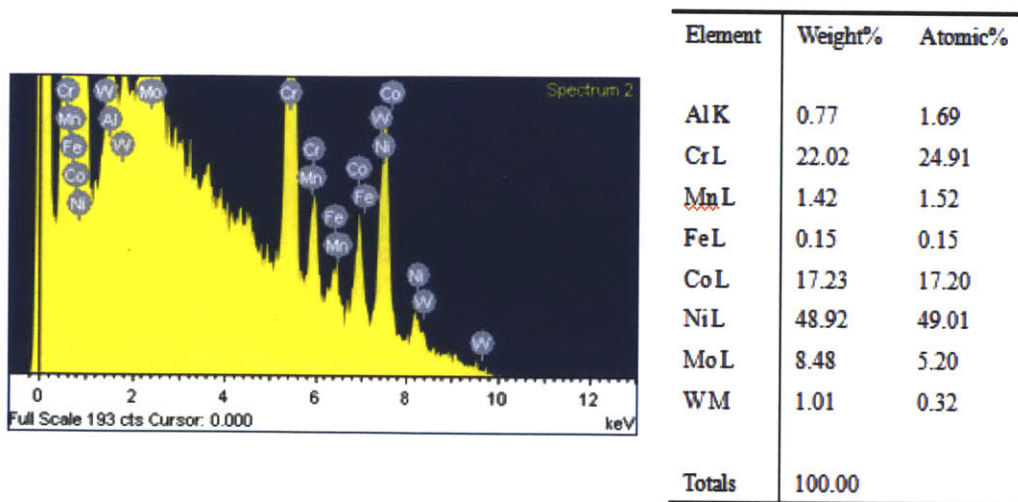
Figure 26-Results of EDS on a polished Inconel 617 sample. The histogram on the left is the intensity spectrum, and the table on the right is the list of the weight and atomic percents determined by the CXA.
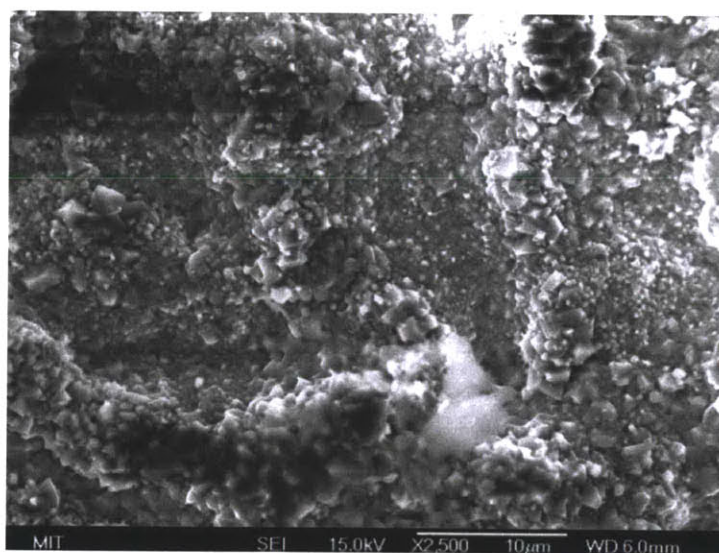
Figure 27-An image of oxidized Inconel 617 taken by a SEM.

4.5 X-Ray Diffraction

X-Ray Diffraction is a technique that can be utilized to determine the chemical makeup of an unknown substance, and for this project it will be used to identify the composition of the deposition on the DCT sample from ENEL. The use of XRD is required because of the wide range of possible compounds present with similar elemental concentrations. The SEM allows for identification of the atomic fraction of different elements, but XRD provides the chemical

formulas of the compounds present. The specific instrument used was the Rigaku High-Power Rotating Anode X-Ray Powder Diffractometer available in the MIT XRD shared experimental facility. X-Ray Powder Diffraction is a specific type of XRD technique that required the crushing of the sample into a fine powder before analysis.

The theory behind XRD is based on the understanding of the interaction of X-rays with material lattices and atoms. It has been observed that X-rays will reflect off of a crystal lattice in a material at certain angles. The angle at which this occurs involves a combination of the wavelength of the X-ray, λ, the lattice spacing, d, and the angle of penetration, θ. This relationship can be summarized by Bragg's Law which is given below (Guinier).

$$n\lambda = 2d\ sin\theta$$

For the purposes of XRD, this equation states that given a certain X-ray source that produces a characteristic X-ray (same wavelength), the X-rays will reflect at certain angles given the lattice size of the sample, and it is possible to detect the angles of reflection with XRD. Therefore, each compound will be identified by the reflection angles because of the unique lattice structure. However, the implementation of XRD is more complicated because most samples contain multiple different compounds and structures which along with statistical noise can make identification of a sample's composition challenging.

The Rigaku is designed to detect the reflection of X-rays off of the sample while precisely measuring the reflection angle. This is accomplished by an X-ray source and a detector, each on different arms, having synchronous movements to allow for detection of X-rays reflecting off of a sample. The X-ray source provides a constant supply of X-rays that are filtered by the divergence slit to ensure they are monodirectional. The X-rays are produced in a
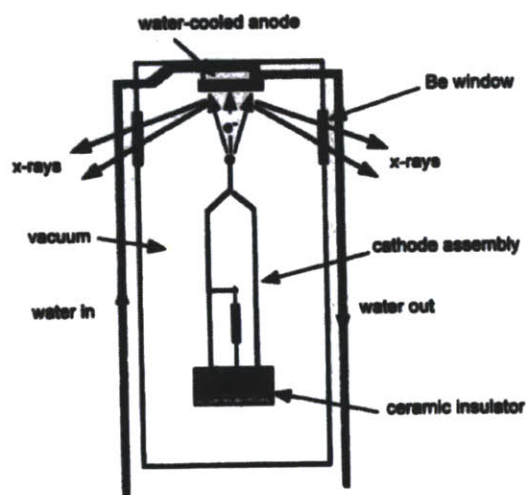
Figure 28-Diagram of an X-Ray source in an XRPD (Suryanarayana and Norton).

vacuum chamber with a Cr source. Electrons are accelerated toward the Cr source and the impact produces heat and X-rays. Most of the impacts produce heat rather than X-rays which requires the system to be cooled (Suryanarayana and Norton). There are two beryllium slits in the chamber to allow for the X-rays to escape because beryllium has a low interaction rate with X-rays. The rest of the chamber is designed to shield the user from X-rays. The X-rays hit the sample and if they reflect they will be detected by the detector. Both the X-ray source and detector move slowly over the course of testing to determine the reflectance at a variety of angles. The data obtained by the detector looks similar to the data in Figure 29, and using a database of data for comparison it is possible to determine the composition of the sample. The key notes from Figure 29 are that the x-axis displays the angle at which the X-rays interact with the sample, and the y-axis is the number of counts. It is apparent that certain angles have much more diffraction than others, but a real sample such as this is so complex that many peaks emerge which makes identification of compounds challenging.
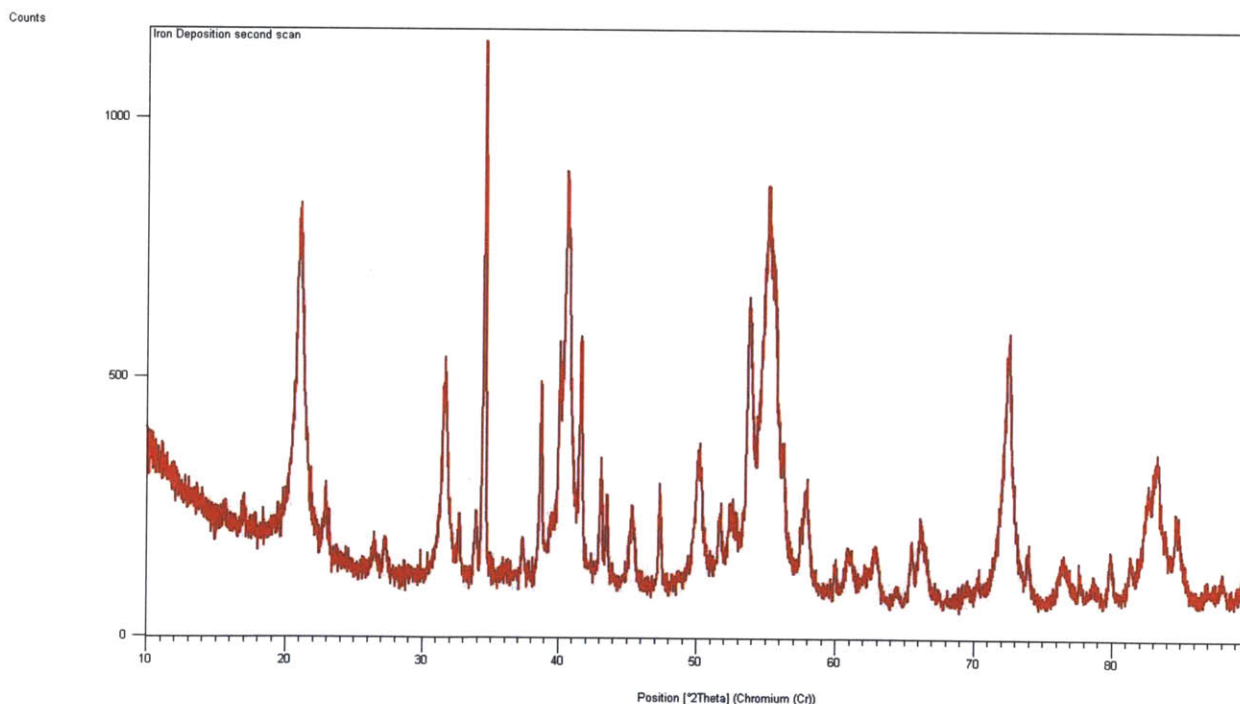
Figure 29-An example of the data produced by XRD analysis. The x axis is the angle of X-ray penetration, and the y axis is the count number.

4.6 Geothermal Experimental Antifouling Loop (GEAL)

The antifouling surfaces for geothermal applications section of this project required the ability to test multiple samples for about a month in an environment similar to that of the Larderello plant. Therefore, an experimental loop called the Geothermal Experimental Antifouling Loop (GEAL) was constructed that would operate in the Green Lab and test multiple samples at once. The testing strategy would be to weigh samples before insertion into the system, and weigh them again after about a month in the GEAL. The weight change will quantify the amount of deposition on the samples, and photo documentation of the samples will identify the structure of the deposition. Each batch will have a carbon steel sample for comparison so the difference in fouling in the same environment can be quantified.

4.6.1 The GEAL Design

The GEAL was designed to achieve the desired design criteria while abiding by the constraints of the available resources of the lab. The design criteria of the GEAL was to imitate the temperature drop across the DCT heat exchanger of 10 °C while maintaining turbulent flow over the sample, and to achieve a H_2S concentration of 2 to 3 ppm. The constraints of the Green Lab were the amount of cooling available from the chilled water, and the amount of power available from the outlets to heat the water. Below is a picture of the GEAL.

Figure 30 - The GEAL loop as seen in the Green Lab.

With unlimited cooling capacity it would be possible to match the Reynold's number of the flow through the DCT while testing many samples simultaneously, but given the cooling limitations it was determined that having turbulent flow through four samples would be acceptable. To achieve this, each heat exchanger will have a sample of 6' with an outside diameter of 0.25". The small diameter of the sample potentially causes coating problems, but was chosen to achieve turbulent flow in the samples. Also, to avoid transients it was necessary to have the same heating capacity as cooling capacity so the loop did not cool over time. A 3000 W heater was used which would turn on and off to keep the reservoir water around 35 °C which is the inlet temperature of the DCT. The size of the reservoir was determined to be 44 gallons to allow the cool water time to heat up before reinjection into the loop. The calculations performed to determine these parameters can be viewed in the Appendix. These critical design parameters were calculated to ensure the successful operation of the GEAL, but are only a small part of the GEAL.

The GEAL is a closed loop system that has four tube-in-tube heat exchangers to allow for convenient testing of four samples. The majority of the water in the system is held in a reservoir at 35 °C while a relatively small amount is pumped through the heat exchanger. The flow is split for the four different samples in a manifold, and each path has a rotameter to measure the flow rate through each sample. Each heat exchanger is a counter-flow tube-in-tube heat exchanger. Each heat exchanger operates with the sample having the working fluid flowing through it while chilled water flows around it. After the fluid passes through the heat exchangers it is recombined in a manifold and injected back into the reservoir. The temperature of the fluid is taken before and after the manifolds to provide an average temperature drop across the heat exchanger. A diagram of the experimental apparatus is shown below in Figure 31.
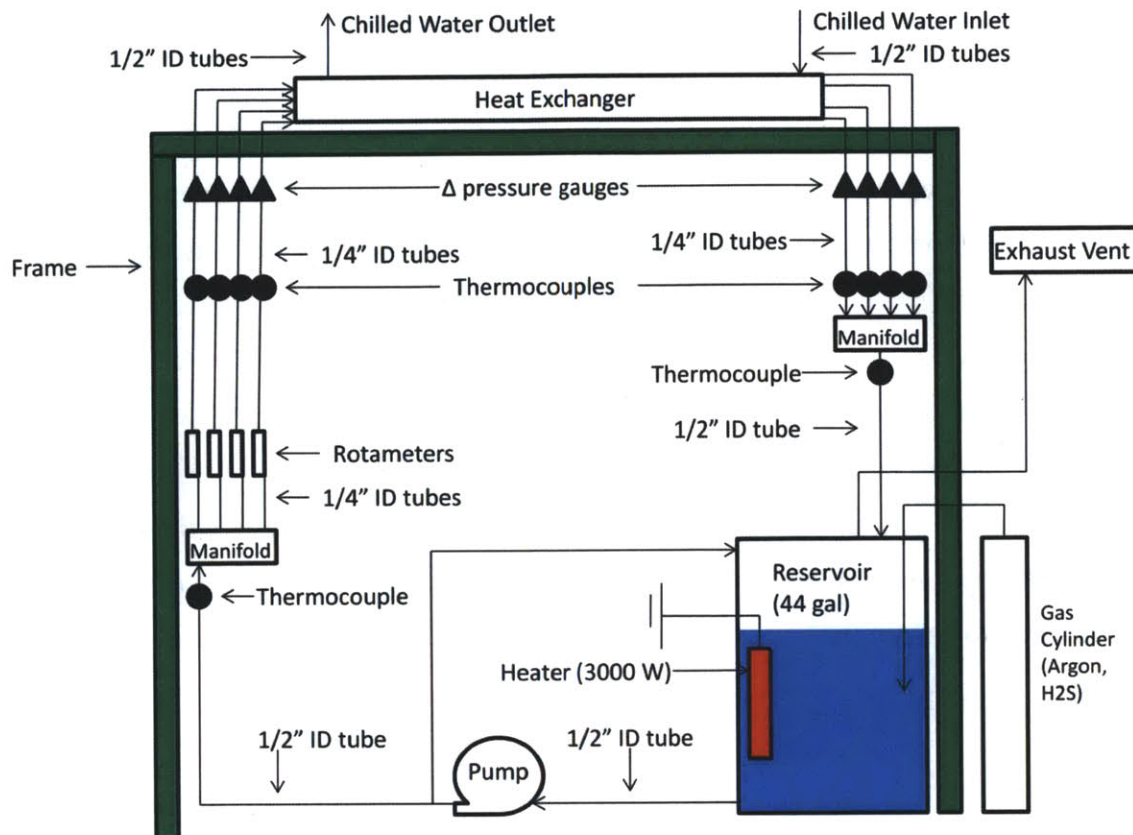
Figure 31 - A schematic of the GEAL.

The insertion of hydrogen sulfide into the system is accomplished by use of a gas cylinder and a sparging stone. A custom gas mixture of argon and hydrogen sulfide is bubbled into the reservoir which creates a pressure inside the containment. According to Henry's Law (Section 2.3.4.1), the partial pressure of hydrogen sulfide above the water is proportional to the concentration in the water. The concentration of the hydrogen sulfide relative to the argon has been calculated to be 14500 ppm to provide the correct concentration in the water (~2.8 ppm). To avoid a build-up of pressure in the reservoir, there is an exhaust line built into the top of the reservoir that allows for gas to leak out of the system into a fume hood. In the fume hood, there is a water trap consisting of a beaker of water with the exhaust line ending under the water which prevents the ingress of air into the system. For safety reasons, there was also a tarp surrounding the gas cylinder and reservoir so that any leak would be vented by the fume hood rather than build up in the room. There is a valve on this line that allows for the adjustment of the pressure in reservoir.

Below are a few pictures of the experimental apparatus that display the features that have just

been discussed. Figure 32 displays the top of the reservoir which has five main penetrations. The center penetration is the heater, and the penetration at 9 o'clock is a thermowell for the heater. This thermowell allows the heater to turn on and off to allow for it to keep the water at a set temperature. The penetration at 12 o'clock deals with the injection of the hydrogen sulfide. The metal pipe allows for insertion of the gas into the sparging stone, and the pipe coming off the side leads to the exhaust vent. The penetration at 3 o'clock is the water return from the heat exchanger, and has a plug that can be removed to allow for insertion of chemicals into the tank to maintain pH. The penetration in the 6 o'clock position is the return from the bypass loop, and is the insertion point for the thermocouple that allows for measurement of the reservoir temperature.
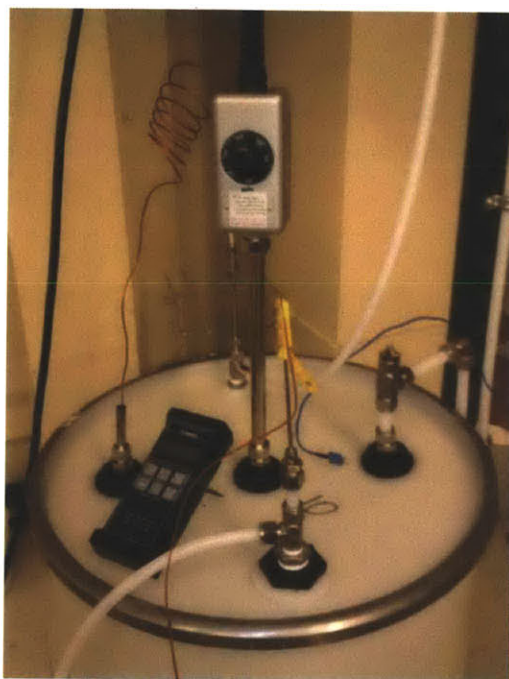
Figure 32 - Top of the reservoir tank with multiple penetrations.

Figure 33 displays the rotameters that provide the flow rate through each of the four parallel counter flow heat exchangers. Figure 34 displays the end of the heat exchangers, and it can be seen that the chilled water is inserted from above into a pipe that fitted around the sample section. Figure 35 shows the pipes leading from the reservoir to the pump, and the bypass loop. A bypass loop was added to the system to reduce the stress on the pump to help maintain a health system. The bypass sends the water directly back to the reservoir.
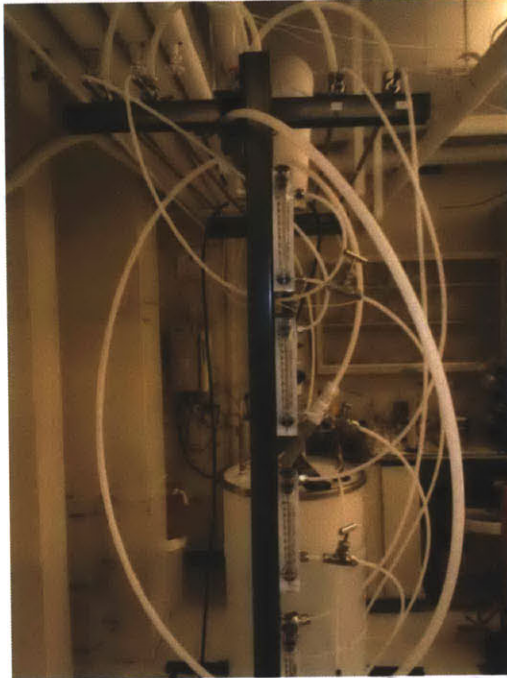
Figure 33 - The rotameters that measure the flow rates prior to entering the heat exchanger.
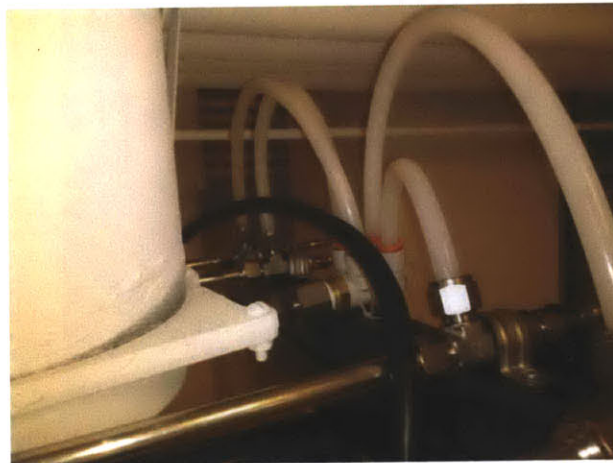
Figure 34 - The junctions on the back ends of each of the heat exchangers. The chilled water enters the heat exchangers through the white tubes seen above.

Figure 35 - The pump can be seen below along with the bypass back to the reservoir.

4.6.2 Validation

Before samples could be inserted into GEAL, it was necessary to demonstrate its adherence to the both the design which includes both the operation and fouling capability of the system. In the previous section it was established that the main constraints of GEAL involved the limitations in the cooling capability of the Green Lab. The heat exchangers were designed to provide 10 °C of cooling on the main loop while maintaining turbulent flow. The following figure is a plot of the temperature change across the heat exchanger with the turbulent regime identified.
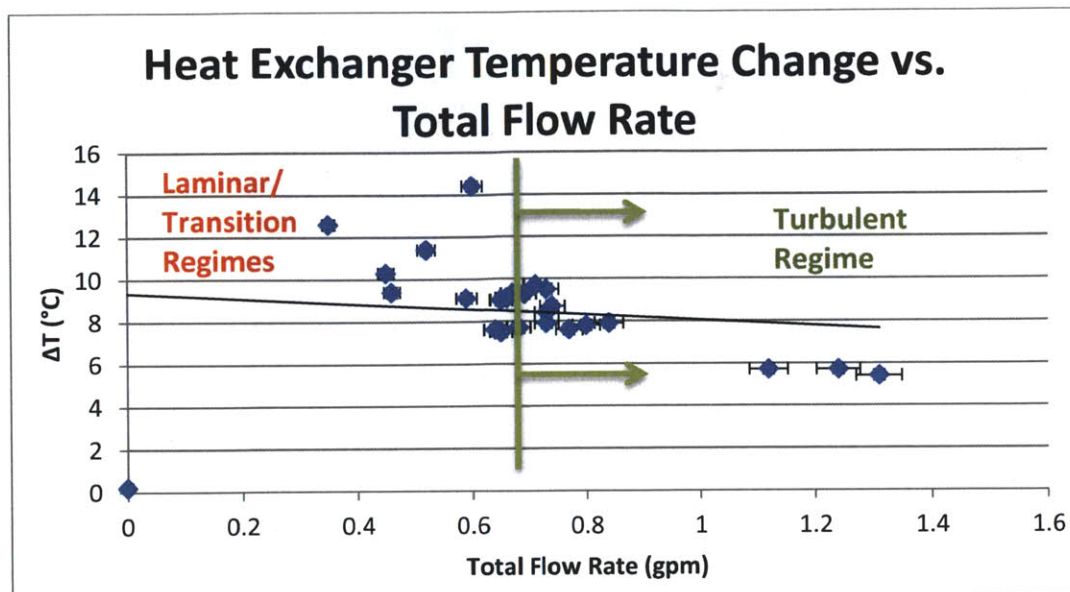
Figure 36 - A graph of the temperature change across the heat exchanger versus the total flow rate. The heat exchanger was designed to be barely turbulent with a 10 degree temperature change.

Figure 36 demonstrates that the transition between the turbulent and laminar regimes occurs approximately around 9 °C temperature changes across the heat exchanger. The discrepancy in the ΔT and the variation in the data above occur because of the inconstancies in the chilled water line which varies in both temperature and flow rate with time. However, the ΔT across the heat exchanger does not need to be exactly 10 °C to produce useful data, and it was decided later by the sponsor to allow for a smaller ΔT in favor of more turbulent flow. Therefore, the combination of temperature drop and flow rate was demonstrated to be adherent to the design, and appropriate to produce the desired results.

The chemistry aspects of the design were critical to producing accurate results, and proved to be the most challenging aspect of the design. The goal of the system was to operate with water at a pH between 5.5 and 7.0, and a H_2S concentration around 2.0 to 3.0 ppm. To obtain the necessary 2.8 to 2.9 mg/L of H_2S the tank must hold a pressure slightly above atmospheric. However, there has been some difficulty obtaining high concentrations of hydrogen sulfide in the fluid due to leaks in the system. While operating GEAL during the validation trial there was only enough H_2S available to maintain a low concentration within the water. However, in the middle of the trial it was decided to sparge the H_2S at an accelerated rate to demonstrate the potential trends. The chemistry changes due to this excursion are shown below.

H2S concentration vs. pH
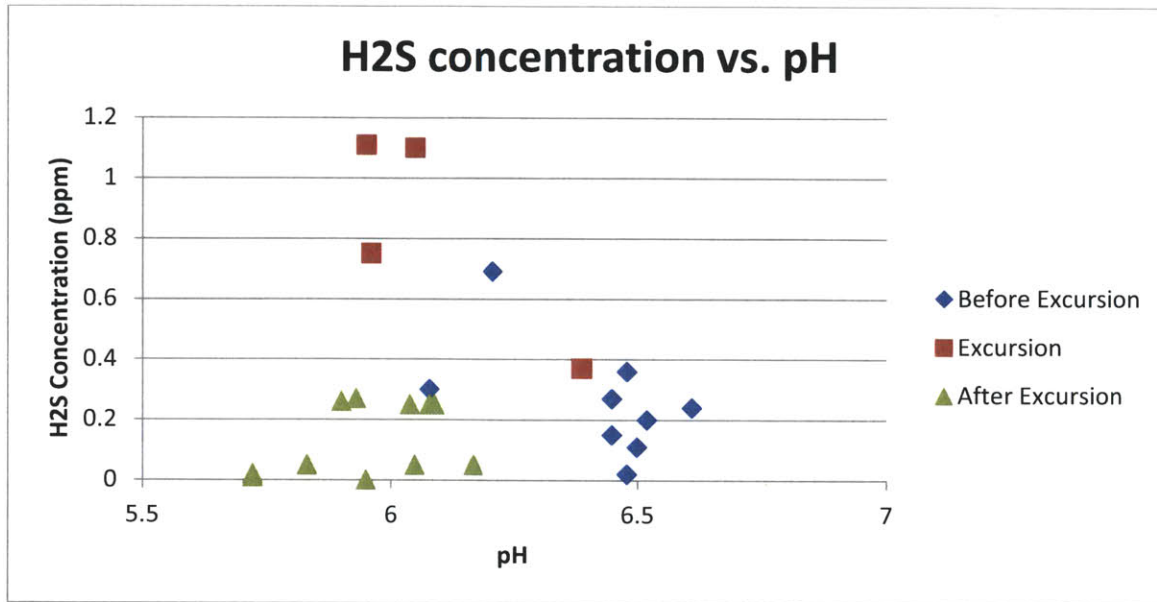
Figure 37-The hydrogen sulfide concentration versus pH during the Validation trial. The uncertainty was 0.01 for the pH measurements, and 0.15 for the hydrogen sulfide concentration.

Figure 37 clearly demonstrates that there was a permanent shift in the pH of the system due to the excursion. This indicates the cumulative effect of H_2S in the system and as a result it will be necessary to add ammonium to the system in the future to maintain a pH above 5.5. This will become more important as higher concentrations of H_2S are attempted.

During validation the system leaked at a rate which only allowed for low concentrations of H_2S, but GEAL was able to provide the necessary fouling of the 1010 carbon steel samples. During the validation trial run, there were three 1010 carbon steel samples and one 304 stainless steel sample tested. All four were weighed before and after insertion into GEAL which provides a good indication of the deposition and fouling of the samples. After extraction from the loop, the samples were allowed to air dry until there was no longer a weight change. The final weight of the sample was used for comparison against the initial weight, and the results are shown in Table 5.

Sample	Material	% Weight Change
1	1010 Carbon Steel	3.83
2	304 Stainless Steel	-0.01
3	1010 Carbon Steel	4.65
4	1010 Carbon Steel	3.67

Table 5 - The results of the validation trial for GEAL. The validation trial ran for 46 days.

To ensure that the weights of the samples were indicative of dry samples, a 12" section of one of the carbon steel tubes was place in an oven at 70 °C for 2 days. The oven should have allowed for all the remaining water in the tube to evaporate, but there was a negligible weight change after the two days in oven. Therefore, the data in Table 5 is indicative that air drying for 8 days is representative of the weight change of the samples due to fouling. The data clearly indicates that the carbon steel tubes are susceptible to fouling in the environment created by GEAL and the stainless steel sample not. This matches the trends seen on the DCT which also did not experience fouling on stainless steel. Furthermore, the deposition on the carbon steel was quite similar to that of the DCT tube which can be seen in the Figures 38 and 39 below. Compare these images to Figures 7 and 8 to see the similarities in the deposition. The constancy between the results using GEAL and the data provided from the DCT validate the legitimately of the data obtained with GEAL.
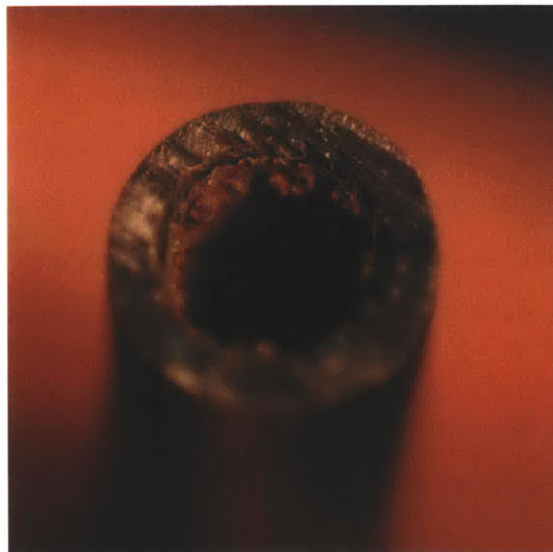
Figure 38 - View of the deposition on the carbon steel samples during the validation trial from the end of the sample.

Figure 39 - View of the deposition on the carbon steel samples from the validation trial from the sectioned sample. Tick marks are 1/64th of an inch.

5. Results and Discussion

This section contains a description of both the data obtained from the different experiments performed, and the interpretation of the data with respect to its implications on the feasibility of the surfaces. Information regarding the experiments themselves such as a description of the experimental procedure, the principles by which they operate, or how they obtain the experimental objectives are outlined in the Methodology (4) section.

5.1 Solar Receiver Study Results and Discussion

5.1.1 Solar Receiver Samples Surface Procurement

The first step of the experimental process is the procurement of the samples to be tested. These samples included silicon carbide, oxidized nickel, oxidized Inconel 617, oxidized Inconel 617 with a 150 nm layer of platinum, and oxidized Inconel 617 with 150 nm platinum and 550 nm nickel oxide layers. The first three surfaces were relatively easy to obtain. A 1"x1"x0.4" block of alpha silicon carbide was purchased from Sentro Tech of Berea, OH, and 99.98% pure 0.5"x0.011" nickel discs were obtained from MIT's NRL. A 1" diameter Inconel 617 rod was purchased from High Temperature Metals of Sylmar, CA, and cut into about twenty 1 cm thick discs. This rod provided the Inconel 617 sample, and the substrate for the 617/Pt and 617/Pt/NiO samples which were more challenging to procure.

The production of the 617/Pt and 617/Pt/NiO surfaces was the most challenging due to the required thickness of the layers. These types of surfaces are created by the deposition of individual metallic particles onto a substrate, Inconel 617 in this case. There are several deposition methods that were considered such as physical vapor deposition (PVD), chemical vapor deposition (CVD), sol-gel deposition, and electroplating. The method of deposition is extremely important because it has a profound effect on the produced surface which in turn drastically changes the optical properties. In the end, the choice was PVD because the data obtained during the literature review indicated promise in this technique for selective surfaces (Braendle). The equipment needed for PVD is very sophisticated and unavailable given the very short timeline of this project. Therefore an outside company, William Advanced Materials of Buellton, CA, order # 13529, was contracted to deposit the surface. To prepare for this, the faces

of the Inconel 617 discs were polished via lapping to a mirror finish. Once polished the samples were cleaned by a sequential ultrasonic cleaning procedure consisting of immersion in an aqueous soap solution, acetone, ethanol and finally distilled water. Post cleaning the samples were assigned a unique designation and placed in plastic bags prior to being coated. A 50 nm thick layer of titanium tungsten (TiW) was deposited on the 617 substrate prior to the platinum layer to enhance the adhesion of the platinum layer. On top of the platinum layer a 325 nm layer of nickel was deposited. The 325 nm layer of nickel will translate to 550 nm of nickel oxide after oxidation. The samples requiring oxidation were oxidized for 6 hours at 1,100 °C which was indicated as a sufficient length of time to ensure adequate oxidation (Kokoropoulos and Evans, Infrared spectral emissivities of cobalt oxide and nickel oxide).

5.1.2 Reflectometer Results

A Cary-Integrating Sphere Reflectometer and SOC-100 Infrared Reflectometer were used to determine the spectral absorptivity of each of the samples. The spectral absorptivity can be determined by measuring the spectral reflectivity which the reflectometers can measure. These measurements were performed by Surface Optics Corp of San Diego, CA, Job # 3520-MP. The reflectivity data was measured at room temperature with an 8° incident angle for light with wavelengths of 200 nm to 12 microns. Measuring reflectivity at room temperature introduces some uncertainty in the extrapolation of this data to higher temperatures, but it is indicated that solar absorptivity increases as temperature increases so the absorptivity measurements will be conservative values (Sainte-Catherine, Jeandin and Kechemair). Obtaining absorptivity from reflectivity is accomplished with the following formula, $\alpha=1-\rho$. This equation is valid because the transmittance through the surface is zero as discussed in the Background (2.2.2) section. Figure 40 shows the measured absorptivities for each material after oxidation at 1,100°C for 6 hours. Note that the SiC sample was not oxidized prior to measurement.
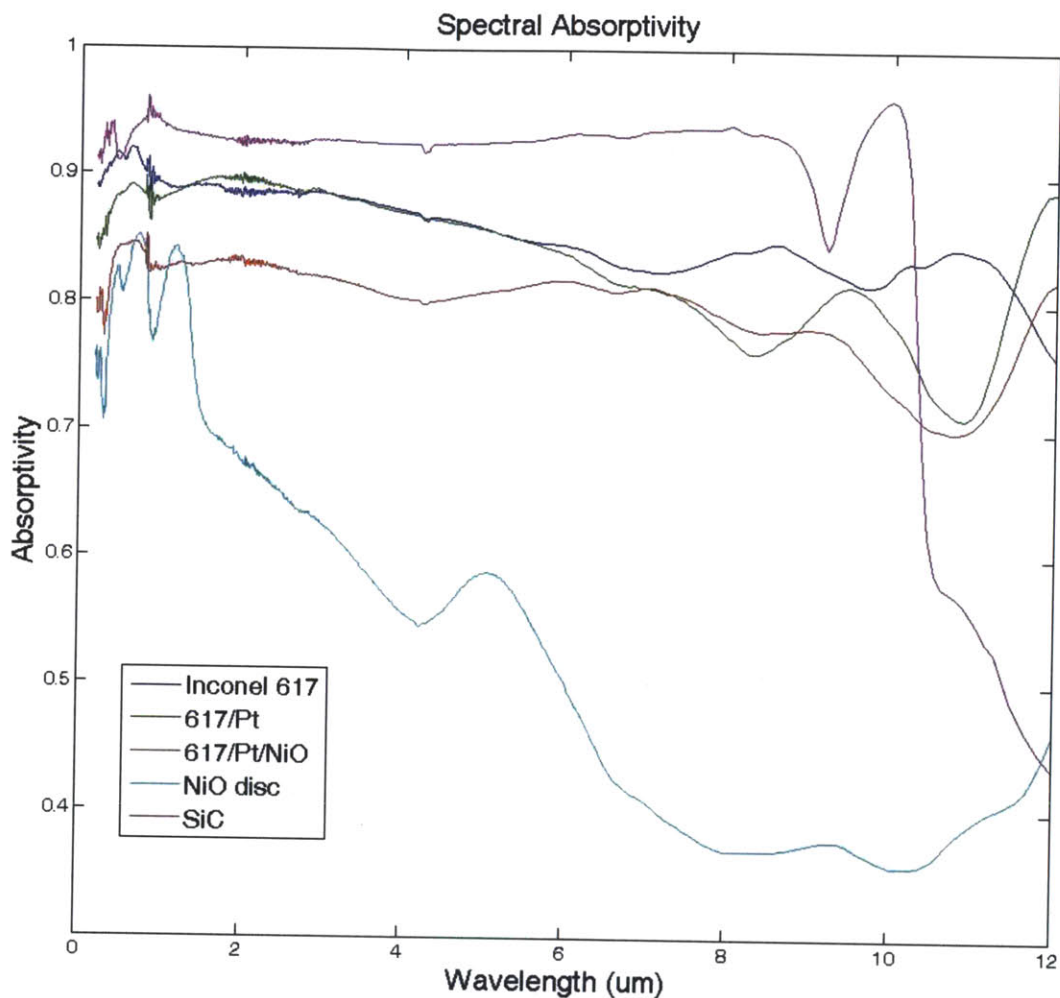
Figure 40-Spectral Absorptivity measured by two reflectometers.

Upon a quick inspection, it is apparent that the nickel oxide disc tested did display some solar selectivity, but the 617/Pt/NiO sample did not. This is probably an indication that the platinum failed as a diffusion barrier which allowed for the disruption of the surface properties. This is collaborated by the fact that the 617/Pt sample demonstrated absorptivity values close to the Inconel 617 sample. The 617/Pt sample should display low absorptivity values due to the small absorptance properties of platinum, but Inconel 617 properties were demonstrated.

5.1.2.1 Analysis of the Spectral Absorptivity Data

From the optical properties presented in Figure 40, the expected performance of each of the

surfaces on a solar thermal receiver can be determined. For the purposes of this analysis, it will be assumed that the surface is operating with an incident power of 500 kW, which is the maximum operating solar heat flux. For the purposes of identifying trends and predicting performance under different operating conditions, the analysis will be performed for a surface at 700 °C, 750 °C, 800 °C, 900 °C, and 1000 °C. These temperatures span the operating temperature range, and include the target operating temperature of 750 °C.

The purpose of this analysis is to determine the performance of the surfaces under the operating conditions for this project, and the thermal efficiency is the parameter that defines their performance. The thermal efficiency is the power retained by the receiver divided by the incident power. Essentially, it tells the percentage of the total possible power that the receiver is able to retain. The goal of this entire project is to identify a surface that produces the highest possible thermal efficiency. Therefore, the thermal efficiencies must be calculated which requires a few other parameters to be calculated first.

The absorptance of each of the surfaces must be calculated to determine the power absorbed by the surface. An explanation of the term absorptance can be found in the Background section (2.2.2). The absorptance can be determined by the summation across all wavelengths of the spectral solar power incident on the receiver at a wavelength multiplied by the receiver's absorptivity at that wavelength by the wavelength distance between data points. The following equation states this relationship more plainly.

$$Absorptance = \sum_{\lambda} \alpha_\lambda P_{solar_\lambda} \Delta\lambda$$

The solar power at each wavelength was calculated by using the data in Figure 40. The curve was normalized, and then scaled to produce a total power of 500 kW. Thus, the absorptance was calculated by matching the two data sets across all wavelengths. This process was performed by a computer code written in MATLAB, and can be viewed in the Appendices.

Due to the ease of its calculation, it is logical to determine the average absorptivity. The average absorptivity provides a single value to estimate the effectiveness of the surfaces under the operating conditions. It is determined by the following equation which is very similar to the equation for absorptance.

$$\alpha_\lambda = \frac{\sum_\lambda \alpha_\lambda P_{solar_\lambda} \Delta\lambda}{\sum_\lambda P_{solar_\lambda} \Delta\lambda}$$

The determination of the emittance of the surfaces is also necessary to determine the thermal efficiency because it defines the amount of power lost by radiation to the environment. This can be determined in a similar fashion to the absorptance, but the Planck Distribution (section 2.2.5) will be considered at each wavelength instead of using the incident solar power. Figure 40 provides the spectral emissivity as well as the spectral absorptivity as defined by Kirchhoff's Law ($\alpha_\lambda = \varepsilon_\lambda$)(Section 2.2.7).

$$Emittance = \sum_\lambda \varepsilon_\lambda P_{Planck_\lambda} \Delta\lambda$$

With the formula for the Planck Distribution, the emitted power at each wavelength and temperature needed was performed and inserted into the above equation. This was also performed in the MATLAB computer code found in the Appendices.

Similar to the average absorptivity, the average emissivity was calculated due to the ease at which it could be done. The average emissivity provides a single value to quantify how well the surface retained the energy absorbed under the considered operating conditions. Its formula is analogous to the average absorptivity formula.

$$\varepsilon_\lambda = \frac{\sum_\lambda \varepsilon_\lambda P_{Planck_\lambda} \Delta\lambda}{\sum_\lambda P_{Planck_\lambda} \Delta\lambda}$$

From the properties just calculated, the rest of the parameters needed for the analysis can be determined. The selectivity ratio is the ratio of the average absorptivity to the average emissivity. A surface's selectivity ratio is a term that is widely used in literature, and assesses how well the surface demonstrated selective properties under the conditions. At low temperatures it has been reported that some materials have selectivity ratios as high as 15, but given the high temperatures of this project the selective ratios will be much lower. The net power retained by the surface is the difference between the absorptance and the emittance, and this quantity is important to the plant because it is the available power to transfer into the thermodynamic system. But more importantly, the thermal efficiency is the net power divided by the incident power which in our case is 500 kW.

The results of the analysis described here for all the surfaces at all five different operating temperatures are given in Table 6. The green shaded cells indicate the highest achieved thermal efficiency at each temperature. There are two shaded at 1000 °C because of how close the values are.

Energy Balance of Candidate and Benchmark Surfaces with 500 kW of Incident Power

Sample	Average Absorptivity (α)	Average Emissivity (ε)	Selectivity Ratio (α/ε)	Absorptance (kW)	Emittance (kW)	Net Power (kW)	Thermal Efficiency (%)
700 °C							
617	0.9034	0.863	1.047	451.70	56.73	394.97	0.790
617/Pt	0.8849	0.856	1.034	442.45	56.29	386.16	0.772
617/Pt/NiO	0.8347	0.807	1.034	417.35	53.06	364.29	0.729
NiO	0.804	0.557	1.443	402.00	36.62	365.38	0.731
SiC	0.9317	0.914	1.019	465.85	60.07	405.78	0.812
750 °C							
617	0.9034	0.865	1.044	451.70	69.98	381.72	0.763
617/Pt	0.8849	0.859	1.030	442.45	69.51	372.94	0.746
617/Pt/NiO	0.8347	0.808	1.033	417.35	65.42	351.93	0.704
NiO	0.804	0.565	1.423	402.00	45.7	356.30	0.713
SiC	0.9317	0.915	1.018	465.85	74.05	391.80	0.784
800 °C							
617	0.9034	0.866	1.043	451.70	85.36	366.34	0.733
617/Pt	0.8849	0.861	1.028	442.45	84.88	357.57	0.715
617/Pt/NiO	0.8347	0.81	1.030	417.35	79.78	337.57	0.675
NiO	0.804	0.572	1.406	402.00	56.37	345.63	0.691
SiC	0.9317	0.916	1.017	465.85	90.29	375.56	0.751
900 °C							
617	0.9034	0.869	1.040	451.70	123.53	328.17	0.656
617/Pt	0.8849	0.866	1.022	442.45	123.04	319.41	0.639
617/Pt/NiO	0.8347	0.812	1.028	417.35	115.4	301.95	0.604
NiO	0.804	0.586	1.372	402.00	83.3	318.70	0.637
SiC	0.9317	0.918	1.015	465.85	130.52	335.33	0.671
1000 °C							
617	0.9034	0.871	1.037	451.70	173.12	278.58	0.557
617/Pt	0.8849	0.869	1.018	442.45	172.67	269.78	0.540
617/Pt/NiO	0.8347	0.814	1.025	417.35	161.67	255.68	0.511
NiO	0.804	0.599	1.342	402.00	118.99	283.01	0.566
SiC	0.9317	0.92	1.013	465.85	182.72	283.13	0.566

Table 6-The energy balance at different operating temperatures for each of the tested surfaces.

5.1.2.2 Interpretation of the Spectral Absorptivity Data

There are many major implications that can be drawn about the tested surfaces from the data presented in Table 6. Firstly, it is clearly demonstrated that the thermal efficiency, and not the selectivity ratio, is the best property to judge the performance of the receiver surface. It is common in literature to quantify the value of a receiver surface with its selectivity ratio because it is a property that more describes the surface itself rather than its application. As can be seen from Tables 6 and 7, the selectivity ratio of the surfaces demonstrates minor deviations across the different temperatures. The thermal efficiency, on the other hand, is a better balance of the operating conditions and surface properties which results in a more suitable measure of performance. As can be seen from Table 6, the values for the thermal efficiencies have larger deviations from each other based on different conditions (in this case temperature). The thermal efficiency is not as common a term in literature because research into selective surfaces is typically not specific to a single application.

There are two major trends that are established from this data concerning the operation of the plant. The first is the trend of thermal efficiencies to decrease with increasing temperature which is demonstrated in Table 6. This is due to the increase in the emittance that is tied to the temperature via the Planck Distribution, and indicates that the receiver should be run at as low a temperature as possible while still achieving the thermodynamic advantages desired from the high temperature. The second is the trend that the thermal efficiency increases with increased incident power which is quantified in Table 7. Table 7 demonstrates the analysis at 750 °C because that is the target operating temperature. It is intuitive that an increase in incident power will result in a larger absorptance, but it is worth stating and demonstrating to indicate the importance in operating the plant as close to maximum incident power as possible.

Energy Balance of Candidate and Benchmark Surfaces

at an Operating Temperature of 750 °C

Sample	Average Absorptivity (α)	Average Emissivity (ε)	Selectivity Ratio (α/ε)	Absorptance (kW)	Emittance (kW)	Net Power (kW)	Thermal Efficiency (%)
450 kW							
617	0.9034	0.865	1.044	406.53	69.98	336.55	0.748
617/Pt	0.8849	0.859	1.030	398.21	69.51	328.70	0.730
617/Pt/NiO	0.8347	0.808	1.033	375.62	65.42	310.20	0.689
NiO	0.804	0.565	1.423	361.80	45.7	316.10	0.702
SiC	0.9317	0.915	1.018	419.27	74.05	345.22	0.767
500 kW							
617	0.9034	0.865	1.044	451.70	69.98	381.72	0.763
617/Pt	0.8849	0.859	1.030	442.45	69.51	372.94	0.746
617/Pt/NiO	0.8347	0.808	1.033	417.35	65.42	351.93	0.704
NiO	0.804	0.565	1.423	402.00	45.7	356.30	0.713
SiC	0.9317	0.915	1.018	465.85	74.05	391.80	0.784

Table 7- The energy balance at different operating incident powers for each of the testing materials. All of the samples are oxidized except for silicon carbide.

However, the most important implication from Table 6 is that silicon carbide demonstrated the best optical properties over the operating temperature range. At each temperature the silicon carbide has the highest absorptance and emittance as it should since it was expected to display black body characteristics. However, it was unexpected that the nickel oxide did not produce the most favorable properties at all temperatures. The nickel oxide did indeed have the lowest emittance of any of the samples due to its selective properties, but it also had the lowest absorption of any of the samples. The savings on the emittance did not make up for the loss of absorptance until 1000 °C as demonstrated by Table 6. This is an indication that at the operating temperatures of this project, it is prudent to use a black body as a receiver instead of a selective surface. This is an interesting observation because at lower temperatures a surface with excellent selective surfaces can be chosen that will create a superior receiver compared to a black body. At higher temperatures the emittance becomes large enough that the selective properties reduce the emittance enough to compensate for the lost absorptance. Therefore, given these operating temperatures a black body should be used because surfaces with excellent selective properties

are not thermally stable, and surfaces that are thermally stable do not provide suitable performance until the maximum operating temperature is reached.

It should also be noted that the silicon carbide only showed marginal improvement over the Inconel 617. Given the data from Tables 6 and 7, it would be more cost effective to simply use a bare receiver as originally planned, but the silicon carbide does possess superior high temperature thermophysical properties compared to the Inconel 617. The other option is to investigate a surface that demonstrates better black body properties that will have a larger margin over the Inconel 617.

5.1.3 IR Camera Results

In order to verify the emissivity data taken above, the comparative emissivity of the 617/Pt/NiO, and 617 samples was determined by use of an Infrared (IR) Camera. The IR camera measures IR wavelengths from 3 to 5 microns. This range does not cover the entire spectrum upon which the surfaces will be emitting, but is enough to compare the samples. Figure 41 is a picture taken with the IR camera of an Inconel 617 sample (right) and the 617/Pt/NiO surface (left) in a hollowed out block of alumina.
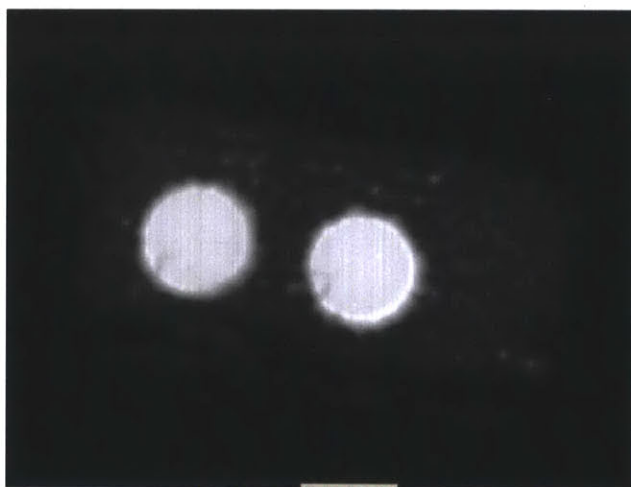
Figure 41-IR image of the 617/Pt/NiO (left) and 617 (right) samples taken at approximately 800 C.

K type thermocouples spot welded to the surfaces of the recessed discs showed that the samples cooled at the same rate. In Figure 41 the samples are at approximately 800 °C, and it appears that

both are emitting the same amount of radiation and this was confirmed using a computer program to measure the IR counts from each sample. This provides strong evidence that the room temperature emissivity evaluation performed above from the reflectivity data is accurate.

The IR camera test also verifies the data presented in Figure 40 and Table 6 that the 617/Pt/NiO surface is not exhibiting the desired selective behavior. The most likely cause is that the surface failed from diffusion. It is also collaborated by a comparison between the benchmark samples of 617 and 617/Pt. Firstly, there was the observed visual blackening of the 617/Pt sample after oxidation at 1,100°C. This indicates failure of the platinum layer because platinum should be effective at preventing oxidation of the Inconel which oxidizes black. Platinum should also have a very low absorptivity and emissivity, less than 0.1. The data presented in Figure 40 shows the 617/Pt sample performing very close to the 617 sample which is an indication of the failure of the platinum layer. In other words, it is likely that the platinum layer allowed diffusion from the Inconel 617 to the surface which ultimately caused the 617/Pt sample to produce optical properties near those of Inconel 617. This would also imply that the 617/Pt/NiO surface has most likely failed which prevented the nickel oxide from demonstrating its solar selective properties. The surfaces of these samples will be investigated to determine if the hypothesis that the platinum layer has failed is correct.

5.1.4 Solar Receiver Sample Surface Morphology

The absorptivity and emissivity data are dependent upon surface phase and structure so it is important to perform surface analysis on the samples. Since the platinum layer of the samples appears to have failed, this analysis will be to confirm or refute this explanation. Scanning Electron Microscopy (SEM) was used to determine the surface morphology and composition. Figure 43 shows the surface structure of oxidized Inconel 617. Using the EDS component of the SEM it was possible to quantify the composition of the surface. The structure seen in Figure 42 is composed of about 55% chromium, 25% oxygen, and 15% manganese with the rest being titanium. This demonstrates that the oxide that forms on Inconel 617 is mostly a chromium oxide with smaller amounts of manganese and titanium. Note that the maximum specified levels of manganese and titanium in 617 are <1.0% and <0.6%. Figure 43 is the surface structure of the

nickel oxide on the 617/Pt/NiO sample. The composition was about 75% nickel, about 10% oxygen, and the rest was chromium, manganese, and titanium. This leaves two possible interpretations. Firstly, the presence of chromium and titanium demonstrate that the platinum was unable to prevent the surface elements of the Inconel 617 from diffusing into the nickel oxide layer which caused the surface to fail. This can be inferred because these two elements in the nickel oxide were the same that were found in the 617 sample. However, the EDS analysis interrogates a depth greater than the combined 750 nm coating thickness, and this to could also explain the presence of chromium and titanium. The other possibility is that the platinum was not put down on this sample by accident which would prove the necessity of the platinum layer to the design of the surface. However, discussions with the PVD coater confirmed the deposition of the platinum layer as specified on all samples. Further analysis should be conducted for a more definitive conclusion, but the project timeline did not allow for this analysis.
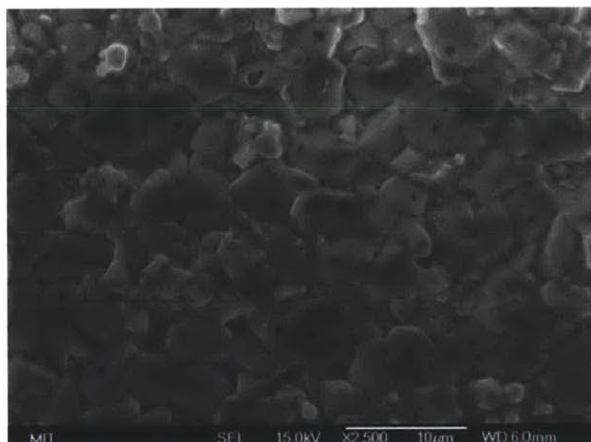
Figure 43-Structure of the oxidized nickel oxide on the 617/Pt/NiO sample obtained with the SEM.

Figure 42-Structure of the surface of the 617 samples obtained with the SEM.

5.2 Geothermal Antifouling Study Results and Discussion

5.2.1 GEAL Operational Data

While the main goal of the Geothermal Experimental Antifouling Loop (GEAL) was to obtain weight change data for the samples, there was a significant amount of data obtained during operation. This data is important to analysis because it provides insight into how the differences in operating conditions effects the weight change data, and how the different samples perform as

heat exchanger coatings. The operational chemistry provide insights into what environment exasperates corrosion and fouling, and an analysis of the operational heat transfer data will allow for quantification of each surfaces potential for application in a heat exchanger.

5.2.1.1 Operational Chemistry

The chemistry of the system during each of the trials is important because of the impacts the changes in chemistry has on the amount of corrosion and fouling. The difference in chemistry between the trials is what requires the use of a carbon steel benchmark, and the carbon steel sample performs differently in each trial because of the chemistry changes. The objective was to maintain the chemistry with a pH of 5.5 to 7 and a hydrogen sulfide concentration in solution of 2 to 3 ppm, but these limits were not always achievable due to challenges that will be discussed shortly. Figures 44 through 48 display the chemistry data taken during the validation trial, Test 1, Test 2, Test 3, and Test 4, respectively.
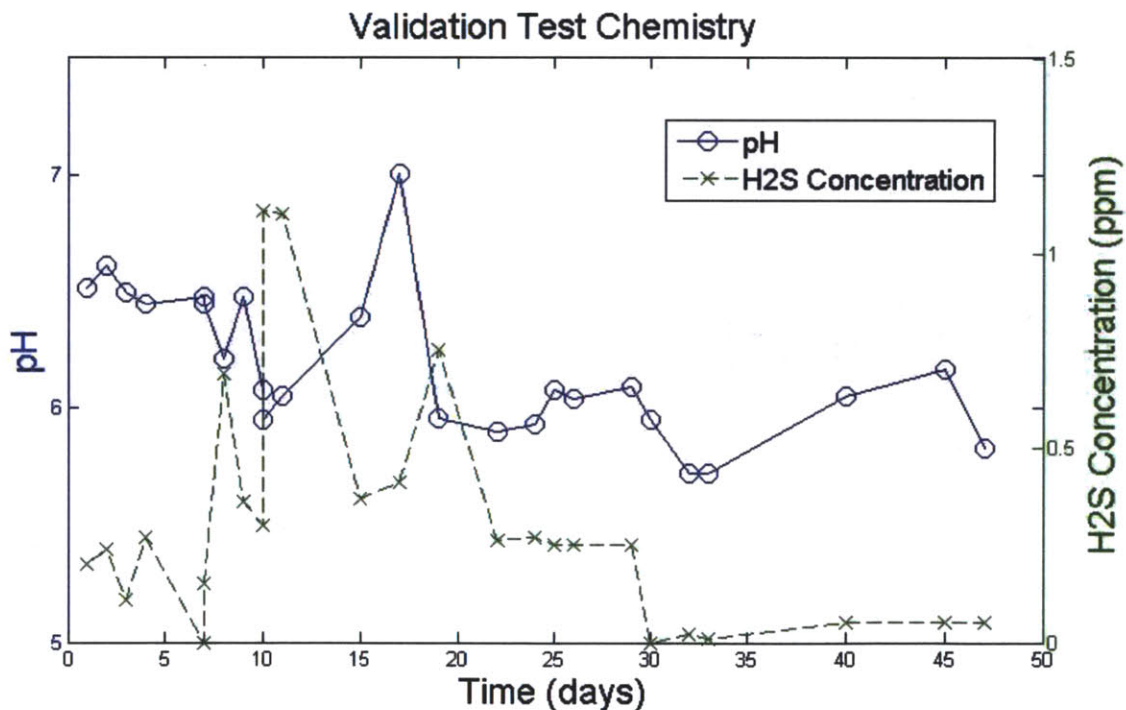
Figure 44-Chemistry data recorded during operation of the validation trial period. The uncertainty was 0.01 for the pH measurements, and 0.15 for the hydrogen sulfide concentration.
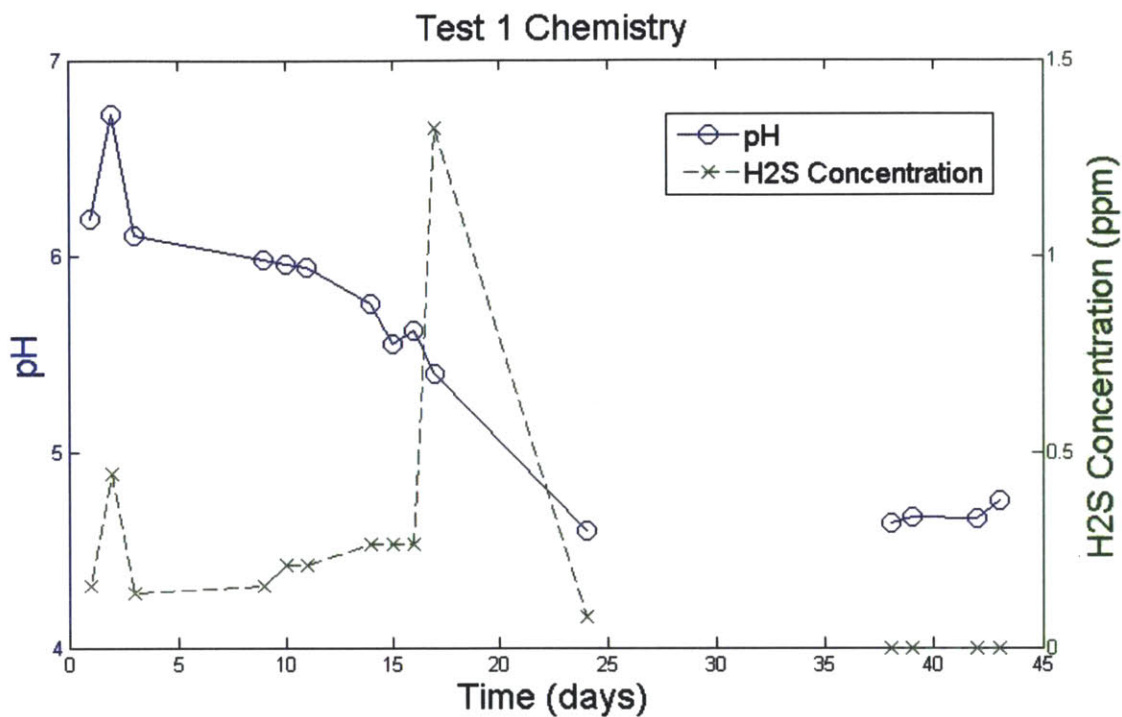
Figure 45-Chemistry data recorded during operation of Test 1. The uncertainty was 0.01 for the pH measurements, and 0.15 for the hydrogen sulfide concentration.
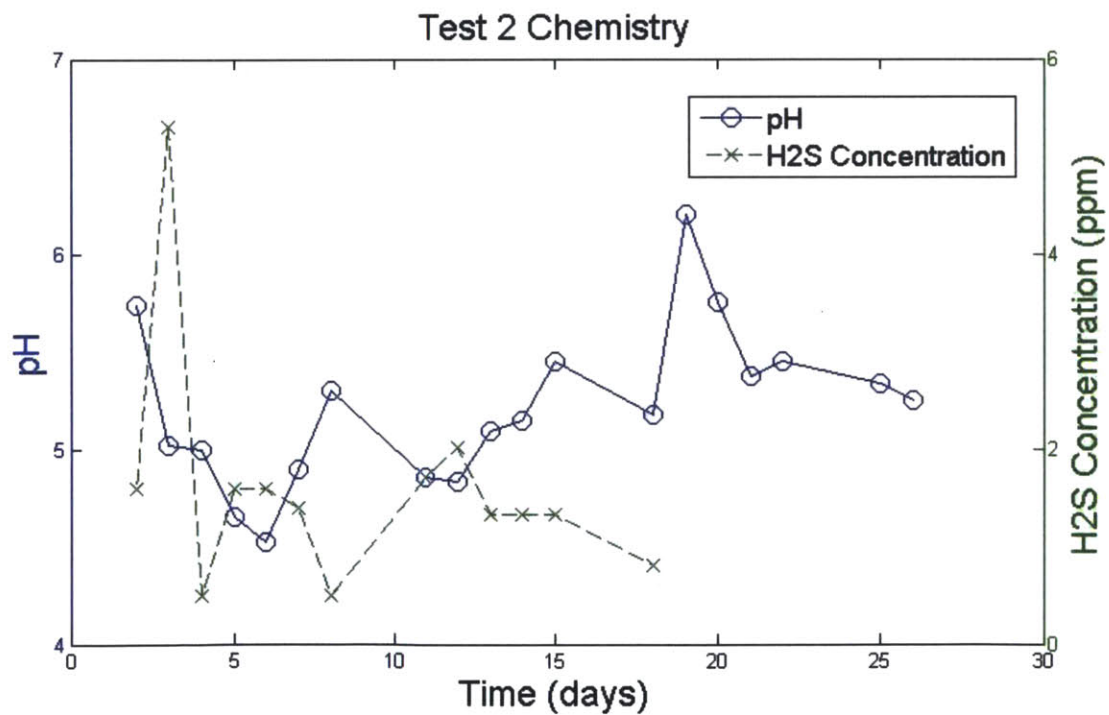
Figure 46-Chemistry data recorded during operation of Test 2. The uncertainty was 0.01 for the pH measurements, and 0.15 for the hydrogen sulfide concentration.
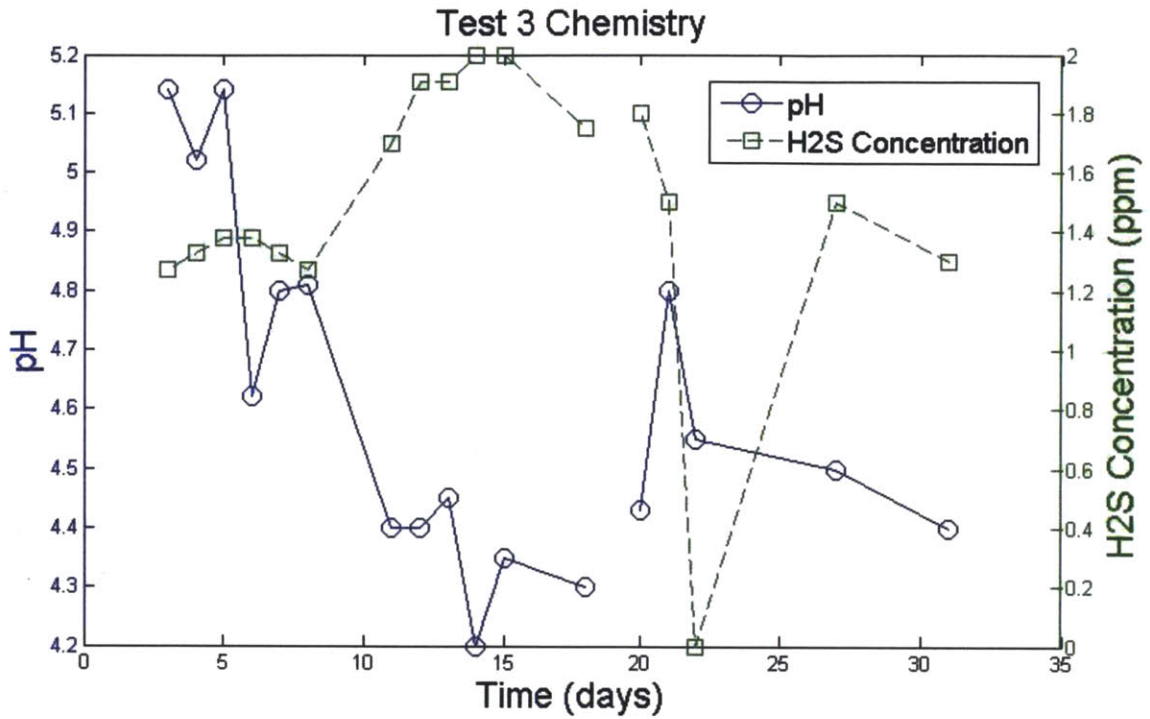
Figure 47-Chemistry data recorded during operation of Test 3. The uncertainty was 0.01 for the pH measurements, and 0.15 for the hydrogen sulfide concentration.
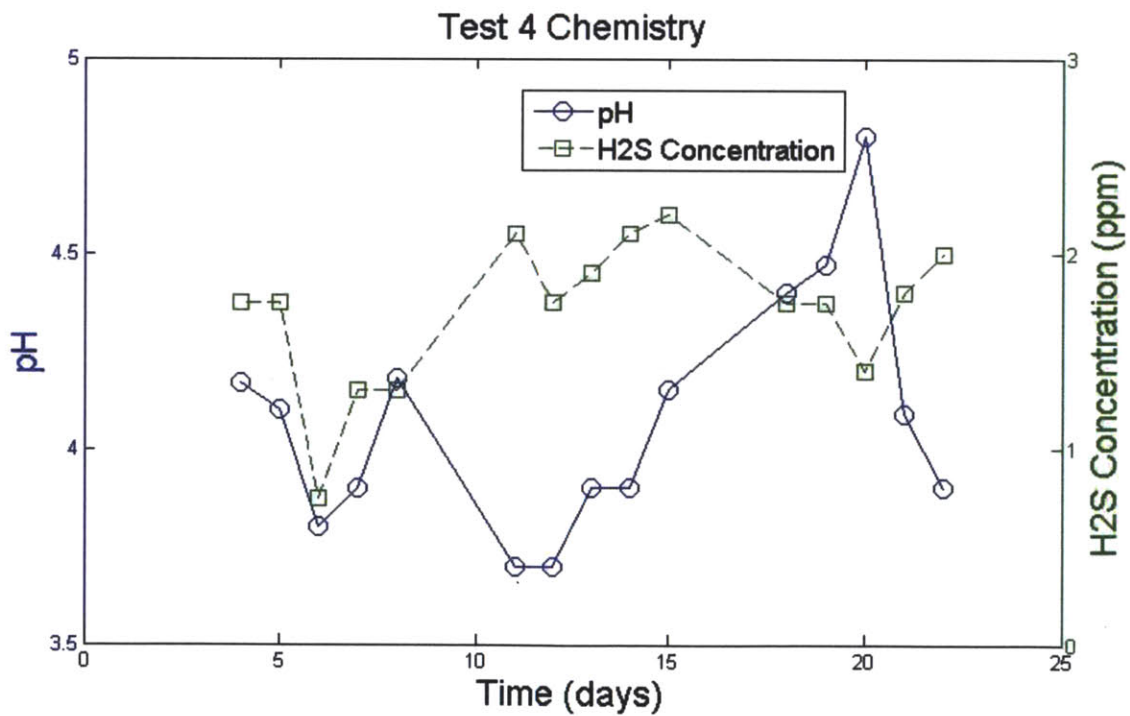
Figure 48-Chemistry data recorded during operation of Test 4. The uncertainty was 0.01 for the pH measurements, and 0.15 for the hydrogen sulfide concentration.

Maintaining the operational chemistry goals were challenging for two main reasons. Firstly, maintaining an elevated hydrogen sulfide concentration was difficult because sealing the top of the tank was not trivial. To maintain elevated hydrogen sulfide levels the tank must become pressurized but there was not a perfect seal between the lid and the body of the tank. This problem was eventually solved by a two pronged approach. The original rubber liner between the lid and body of the tank was removed and silicone was applied around the entire lid before clamping it down. While this did not completely stop the leaking of hydrogen sulfide, it did significantly impede the loss of hydrogen sulfide (it should be noted that the leaking hydrogen sulfide was always contained within the tarp set up around the tank and immediately vented so it never posed a threat to anyone in the lab). The second change that resulted in higher hydrogen sulfide levels was the switching of gas from a 750 ppm H_2S with argon (Validation and Test 1) to a 14500 ppm H_2S with argon (Tests 2, 3, and 4). The new concentration was also chosen so that a single tank would last through an entire trial. A higher concentration results in less required flow rate which extends the life of the tank.

The second major challenge involved keeping the pH above the 5.5 limit. Initially this was not a challenge because of the low hydrogen sulfide levels, but once the leak was addressed and the hydrogen sulfide concentration was consistently above 1 ppm the pH began to drop quickly. This is best illustrated in Figure 37 where the hydrogen sulfide concentration was elevated only for short time but never recovers afterward. Thus, outside assistance was necessary to maintain the pH which was done by the insertion of ammonium hydroxide. During the later tests it appears from the data that the pH was consistently below the 5.5 limit, but this data is misleading. The pH of the system was always recorded before the insertion of ammonium hydroxide which means the recorded number was the lowest pH of the day. Since ammonium was added daily, there was a daily cycle where the pH would be at its maximum after ammonium insertion, and it would then work its way back down during the next 24 hours. The pH would then be recorded before the ammonium was added again which would result in the lowest value for the pH possible. Therefore, while the system did operate outside of the desired pH range for some of the time, the majority of the operational time was spent in the desired range. This is just not well represented by Figures 46 through 48.

5.2.1.2 Operational Heat Transfer

The heat transfer capability of the coatings is an important property to consider due to the intent to apply it to a heat exchanger. In order to quantify the heat transfer performance of the samples during operation, the temperature of the fluid was taken at the inlet and outlet of each sample along with the flow rate through each sample. There is no data available for the validation trial since the thermocouples on the individual samples were not installed until Test 1. This data was then applied to the following equation to determine the heat transfer at the time of the measurement.

$$q'' = \frac{\dot{m}c_p(T_{in} - T_{out})}{A}$$

The area (A) will be the surface area on the outside of the sample that interfaces with the chilled water. This will allow for a more consistent area to be used between the samples, and the thickness of the coatings does not have to be measured precisely. The coating thickness will still influence the heat flux, but it will be through the temperature drop rather than the surface area with this analysis. It is also assumed that the specific heat (c_p) is the specific heat of water at 35 °C. This assumption is justified because the mixture is primarily water, and the same fluid will be in each sample so any small discrepancies will be applied to each sample allowing for accurate comparisons. The heat flux data for each test is presented in Figures 49 through 52.
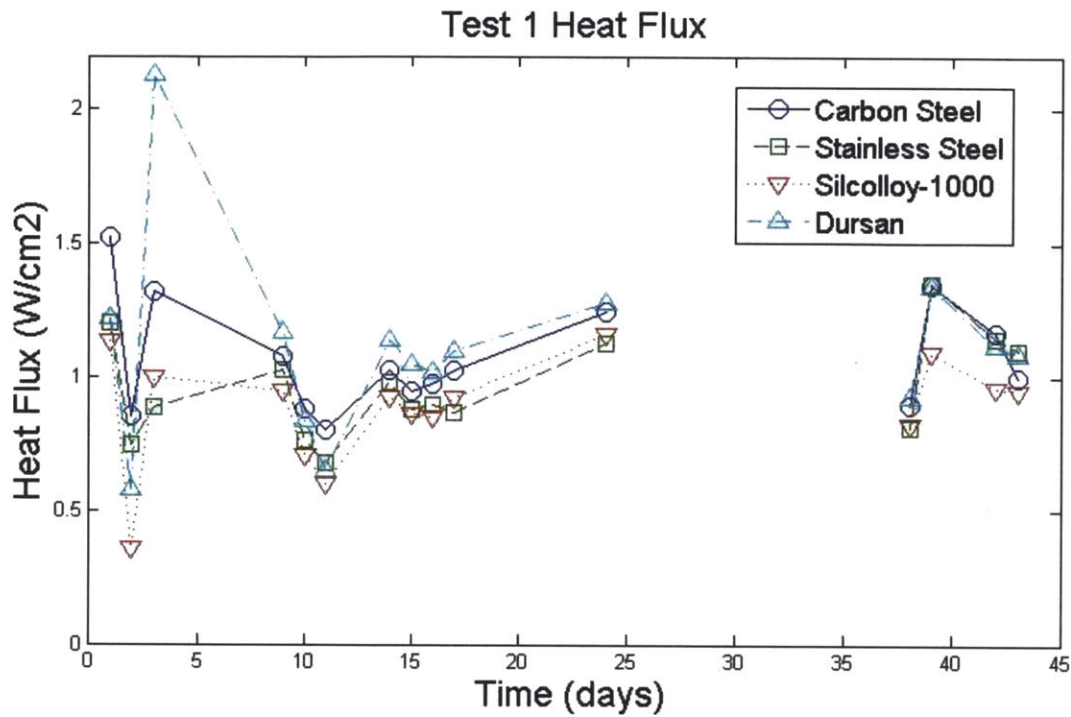
Test 1 Heat Flux

Figure 49-Heat flux data for each sample tested during Test 1. Wall thickness on the carbon steel sample was 0.035", and 0.028" for the stainless steel sample.
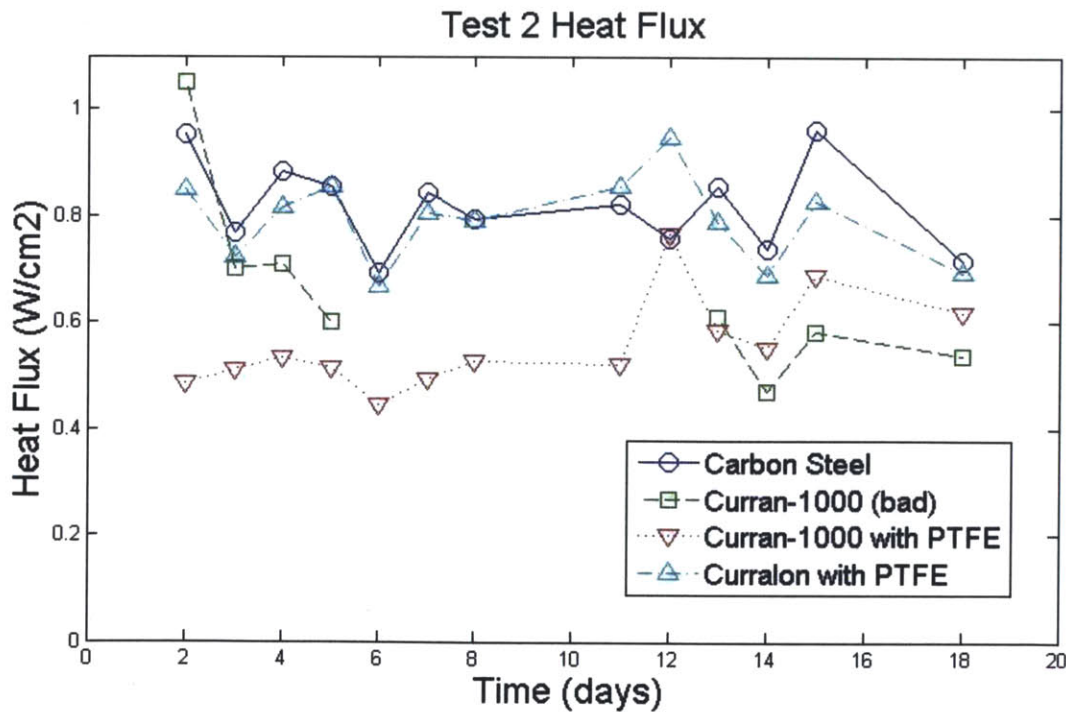
Test 2 Heat Flux

Figure 50-Heat flux data for each sample tested during Test 2.
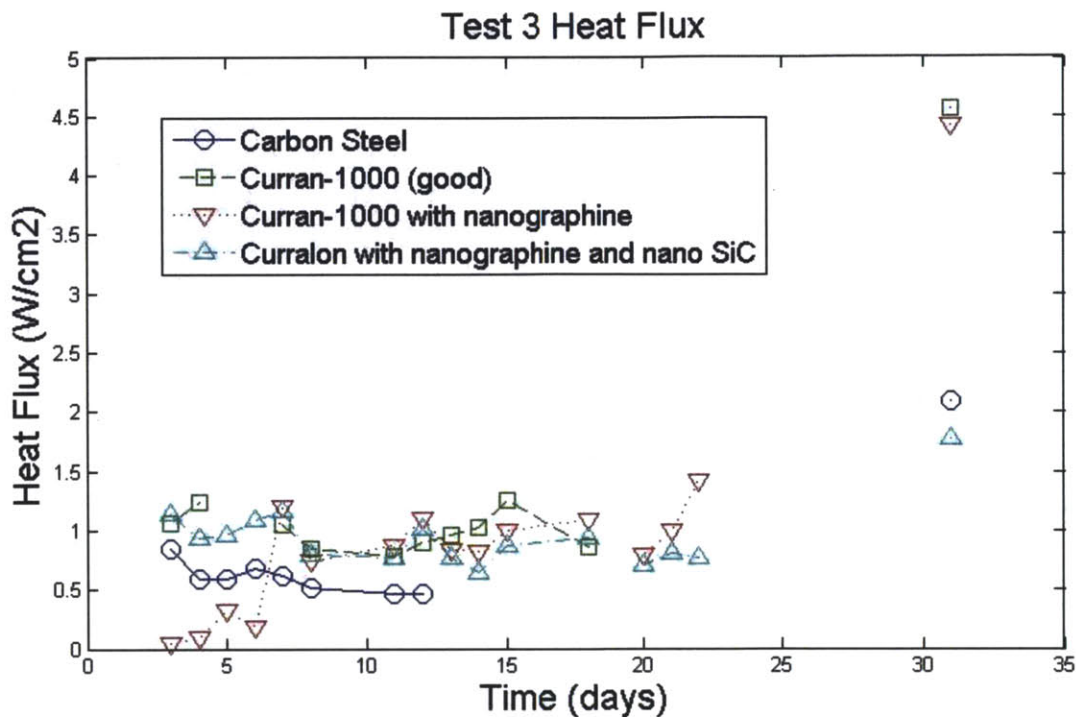
Test 3 Heat Flux

Figure 51-Heat flux data for each sample tested during Test 3.
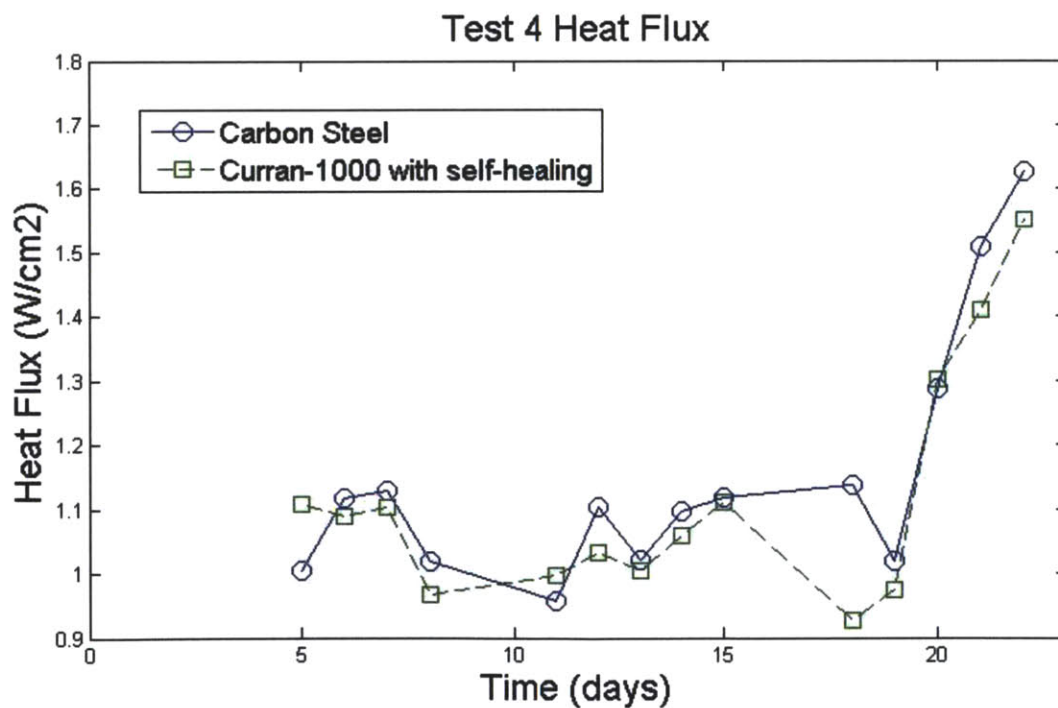
Test 4 Heat Flux

Figure 52-Heat flux data for each sample tested during Test 4.

The basis for comparison between each of these figures is the carbon steel sample which was present in each testing period. This allows for a general sense of the heat transfer capability of samples across different testing periods. There are a few points of note about these graphs. Firstly, the rising and falling of the heat flux of all the samples over time is not caused by changes in the operating loop, but rather by changes in the flow rate of the chilled water. This flow rate was variable and outside of the control of the lab. Secondly, the lack of data for some samples was due to holidays, low flow rates, or inability to take data due to the discoloration of the rotameter by the working fluid. The samples in Test 2 ran for 26 days but there is no heat transfer data after 18 days because the flow rate was impossible to determine due to the black discoloration of the fluid. Lastly, the difference in the carbon steel heat flux across the tests was partially due to the amount of deposition and fouling which was different in each test. Specifically, the fouling was considerable less in Tests 1 and 2 compared to Tests 2 and 3, and the heat flux is noticeably higher in Figures 49 and 52 which further justifies the need for this study.

5.2.1.3 Heat Transfer Confidence Intervals

The operational heat transfer data presented in Figures 49 through 52 visually seems to indicate that some samples allowed for increased heat transfer under similar operating conditions. However, statistical confidence interval testing must be applied to determine the confidence level that the data presented in the figures genuinely demonstrates a higher heat transfer in one sample compared to another. To apply this method, the mean and standard deviation of the data presented must be obtained for each data set (the heat flux data for each sample) which can be found by using the following equations.

$$\bar{X} = \left(\frac{1}{n}\right) \sum_{i=1}^{n} X_i$$

$$\sigma = \sqrt{\left[\frac{1}{(n-1)}\right] \sum_{i=1}^{n} (X_i - \bar{X})^2}$$

In the equations above X_i is a specific value in the sample, n is the total number of data points in the sample, $\bar{X}$ is the average of the sample, and σ is the standard deviation of the sample (these equations are for samples not populations). The equation to determine the confidence interval between two samples with true means μ_1 and μ_2 is given below.

$$\overline{X_1} - \overline{X_2} - Z_{\alpha/2}\sqrt{\frac{\sigma_1^2}{n_1} + \frac{\sigma_2^2}{n_2}} \leq \mu_1 - \mu_2 \leq \overline{X_1} - \overline{X_2} + Z_{\alpha/2}\sqrt{\frac{\sigma_1^2}{n_1} + \frac{\sigma_2^2}{n_2}}$$

Values of $Z_{\alpha/2}$

Confidence Interval	$Z_{\alpha/2}$
80%	1.2816
85%	1.4350
90%	1.6449
95%	1.9600
96%	2.0537
98%	2.3263
99%	2.5758

Table 8-Values of $Z_{\alpha/2}$ corresponding to the appropriate confidence interval.

Applying this method to the data presented in Figures 49 through 52 results in Table 9 presented below. In Table 9, each sample is compared to the carbon steel sample from the same test, and the confidence defined is the confidence that carbon steel demonstrated a higher heat flux. NC stands for "No Confidence" which means these samples failed each confidence interval test. There were no samples that demonstrated with confidence that they operated with a higher heat flux than the carbon steel samples. However, as seen below, several likely operated with a lower heat flux.

Heat Flux Confidence Between Samples

Test	Sample	n	X	σ	Confidence that carbon steel had a higher heat flux (NC-no confidence)
1	Carbon Steel	15	1.0731	0.2061	-
1	Stainless Steel	15	0.9654	0.1905	85%
1	Silcolloy 1000	15	0.8879	0.2081	98%
1	Dursan	15	1.1098	0.3539	NC
2	Carbon Steel	13	0.8188	0.0846	-
2	Curran 1000 (bad)	8	0.6574	0.1780	98%
2	Curran 1000 with PTFE	13	0.5556	0.0889	99%
2	Curralon with PTFE	13	0.7927	0.0810	NC
3	Carbon Steel	9	0.7642	0.5095	-
3	Curran 1000 (good)	11	1.3200	1.0845	NC
3	Curran 1000 with nano graphene	16	0.9955	1.0003	NC
3	Curran 1000 with nano graphene and nano silicon carbide	16	0.9461	0.2685	NC
4	Carbon Steel	14	1.1533	0.1947	-
4	Carbon Steel with self-healing	14	1.1171	0.1802	NC

Table 9-Confidences on the heat flux compared to the carbon steel sample for each sample. "NC" stands for No Confidence.

Many of the conclusions drawn from Table 9 were expected. The heat flux of the carbon steel was higher than the stainless steel with 85% confidence which was expected as carbon steel has a thermal conductivity of 51.9 W/mK while stainless steel is 16.2 W/mK. However, the stainless steel sample was thinner than the carbon steel which potentially offset this thermal conductivity difference. Also, the difference between the correct mixture and incorrect mixture of the Curran-1000 was apparent because the incorrect mixture performed considerably worse than the carbon steel in Test 2 with 98% confidence, and the correct mixture performed close enough to the carbon steel during Test 3 to result in minimal confidence. Additionally, the PTFE does not appear to help the heat transfer because the Curran 1000 in Test 3 resulted in "No Confidence" but the Curran 1000 with PTFE in Test 2 had a lower heat flux with 99% confidence. Also, from the data in Table 9 it can be suspected but not proven that the nanoparticles performed well during testing from a heat transfer point of view. There thermal conductivity of the samples will

be investigated in the section 5.2.2.

5.2.1.4 Heat Transfer Error Propagation

An error propagation analysis of the operational heat transfer data is appropriate because the measurements used to obtain the heat flux have their own inherent uncertainties, and it is important to determine how these uncertainties propagate through the data. The method used to do this is indicated by the formula below for a function, $f = f(x, y)$.

$$\sigma_f^2 \approx \left(\frac{\partial f}{\partial x}\right)^2 \sigma_x^2 + \left(\frac{\partial f}{\partial y}\right)^2 \sigma_y^2$$

For the heat flux equation given earlier, $q'' = \frac{\dot{m}c_p(T_{in} - T_{out})}{A}$, the following equation can be derived for the standard deviation of the heat flux where $\dot{m}$ is the flow rate, T_H is the fluid temperature entering the heat exchanger, and T_C is the fluid temperature exiting the heat exchanger.

$$\sigma_{q''} = q'' \sqrt{\frac{\sigma_{\dot{m}}^2}{\dot{m}^2} + \frac{\sigma_{T_H}^2}{(T_H - T_C)^2} + \frac{\sigma_{T_C}^2}{(T_H - T_C)^2}}$$

Thus, to obtain the standard deviation of a heat flux data point, the values for the flow rate and temperatures across the heat exchanger are input to the equation above with the correct standard deviation. The standard deviation for the temperatures was obtained by calibration of the thermocouples, and the results are listed in Table 10. The variance for the flow rate was assumed to be 3% of the measured flow rate.

Thermocouple Calibration Results

Thermocouple	Variance (σ^2)	Standard Deviation (σ)
H1	0.21	0.4583
H2	0.03	0.1732
H3	0.018	0.1342
H4	0.064	0.2530
C1	0.042	0.2049
C2	0.036	0.1897
C3	0.226	0.4754
C4	0.1	0.3162

Table 10-Thermocouple calibration results obtained from inserting the thermocouples in freezing and boiling water. "H" and "C" indicate the hot and cold side of the heat exchanger, and the number identifies the thermocouple.

Given these inputs, the standard deviations that result are quite large compared to the heat flux values. The standard deviations are large enough that it brings into question any concrete conclusions drawn from the operational heat transfer data. Figure 53 is an example of the comparison between two samples taking the error propagation into account.
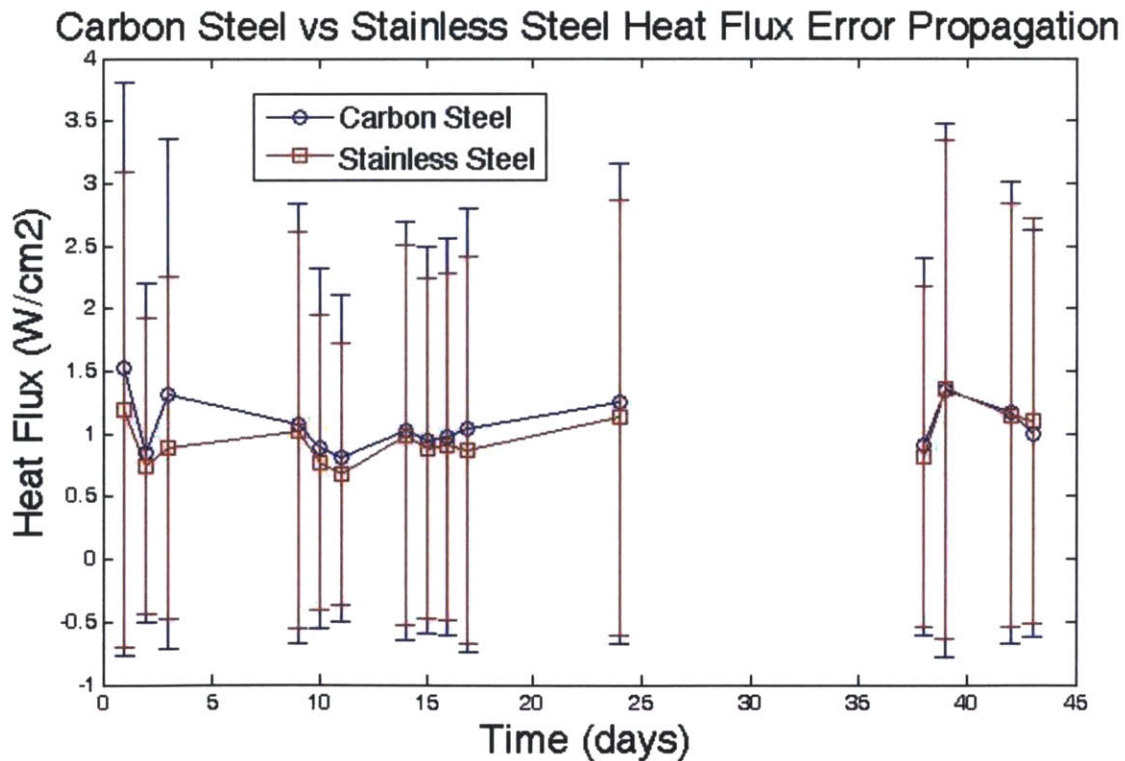
Figure 53-Carbon steel versus stainless steel heat flux displaying the error propagation.

The high and low bars for each data point signify the range in which the true value is likely to be. However, there is so much overlap between the two samples that it becomes extremely tricky to say that one value is significantly different than the other. Therefore, no concrete conclusions should be drawn from the operations heat flux data. The weak point in the data gathering was the measurement of the flow rate because the heat flux standard deviation is dominated by the contribution from the flow rate term because the variance was only assumed to be 3%. If a smaller variance is assumed then the data might appear to be more significant, but given the flow rate measurements there is no reason to assume a smaller variance.

5.2.2 Thermal Conductivity

To measure the thermal conductivity a NETZSCH NanoFlash LFA 447 will be used which measures thermal conductivity according to ASTM E-1461. This instrument measures the thermal diffusivity of the sample and calculates the thermal conductivity from the user input data using the equation below.

$$k \left(\frac{W}{mK} \right) = c_p \left(\frac{J}{kgK} \right) \rho \left(\frac{kg}{m^3} \right) \alpha \left(\frac{m^2}{s} \right)$$

Due to a lack of information about each of the coatings, each sample was treated as a one layer system rather than a two layer system. This one layer approach will give the total thermal conductivity of the sample with the coating and carbon steel together. To allow for a good comparison between the coatings, the specific heat and density of each sample were assumed to be that of 1010 carbon steel which is 448 J/kgK and 7872 kg/m^3, respectively. Therefore, the thermal conductivity measurement might not be the exact value, but this analysis allows for an accurate comparison between the samples. Unfortunately, only coatings from Curran International could be tested.
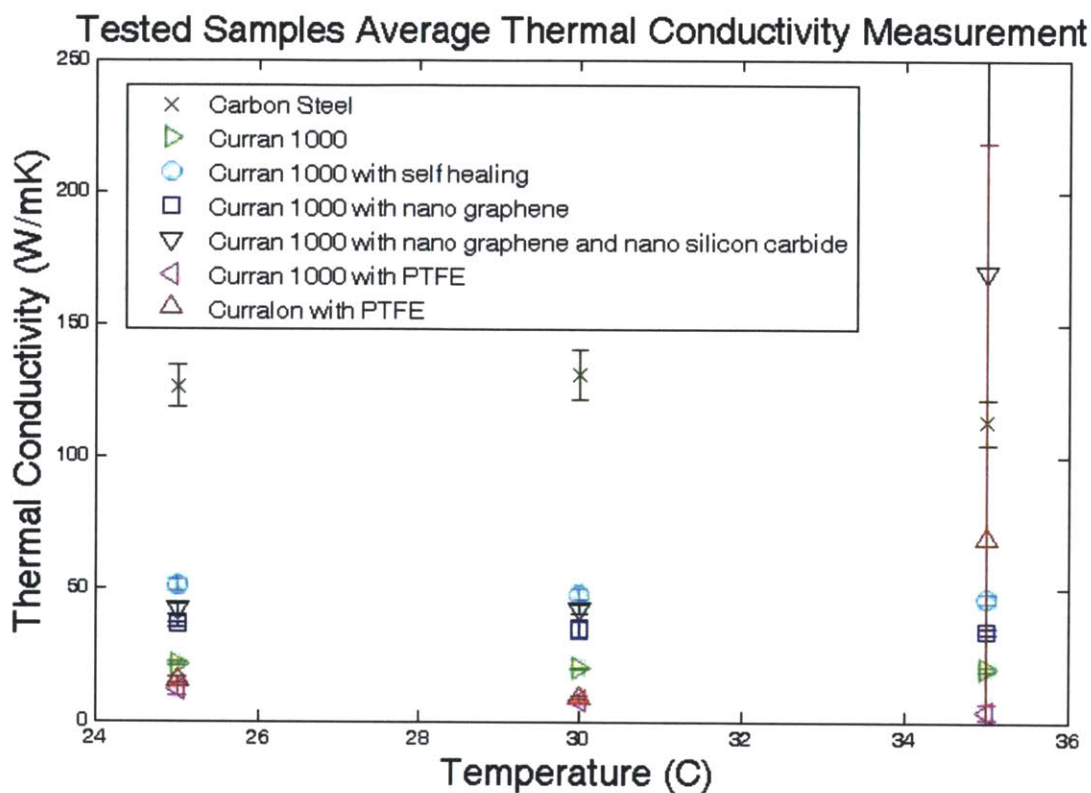
Figure 54-The average thermal conductivity measurement of each of the samples at different temperatures.

The data presented in Figure 54 appears to be consistent with the exception of two data points which are the Curran 1000 with nanographene and nanosilicon carbide and the Curralon with PTFE at 35 °C. The error bars for these two measurements are quite large as demonstrated by the red bar running through the 35 °C data and the black bar behind it. The four other samples demonstrate similar thermal conductivities at each temperature, and the measurements at 25°C and 30°C are comparable for the Curran 1000 with nanographene and nanosilicon carbide and the Curralon with PTFE. Therefore, due to the high potential error and inconsistency with the other data any possible implications from these two data points will be noted as questionable.

There are a few insightful implications into the heat transfer capacity of each coating from the data presented in Figure 54. Firstly, it is demonstrated that PTFE drastically inhibits the thermal conductivity of the coatings. Both of the coatings with PTFE were measured with the lowest thermal conductivities except for the Curralon with PTFE coating at 35°C which has already been pointed out as suspicious. Also, the difference between the Curran 1000 coating with and

without the PTFE is clearly demonstrated, and the PTFE significantly lowers the thermal conductivity. The second major implication is that the addition of nanoparticles to the coating drastically enhances the thermal conductivity. At each of the temperatures measured, the Curran 1000 coating with nanographene demonstrates a significant thermal conductivity margin above the Curran 1000 which implies that the nanoparticles transfer heat more efficiently than the microparticles typically used in the Curran 1000. Additionally, the addition of more nanoparticles in nanosilicon carbide enhanced the thermal conductivity more. Even if you discount the drastically high thermal conductivity measurement at 35 °C, the data still indicates an enhancement of the thermal conductivity from the nanosilicon carbide. This thermal conductivity enhancement was expected and was the reason nanosilicon carbide was chosen for testing. Thirdly, the coating that appeared to display the best thermal conductivity was the Curran 1000 with self healing properties. The boehmite that was added has a crystal structure which usually indicates a high thermal conductivity which when added to the Curran 1000 was able to increase the thermal conductivity of the coating. Lastly, the plain carbon steel demonstrated the highest thermal conductivity of any sample by a large margin which was to be expected.

5.2.3 Sample Weight Change Data

The sample weight change data will be used to determine the performance of the coatings from a corrosion and fouling perspective. Due to the nature of the problems at the plant, this is the major concern and will carry a large portion of the weight of the coating selection. Most of the coatings were applied to inside of a 6' long ¼" 1010 carbon steel tube. The carbon steel tubes that the coatings were applied to were identical to the plain carbon steel tube that was tested. The interaction area that is specified below in Table 11 is the initial area of interaction between the fluid and the inside of the sample. It is assumed that the interaction area of the coated samples is the same as the uncoated carbon steel sample. The stainless steel sample was not as thick as the carbon steel sample which results in a larger interaction area. The Dursan sample was the only tube sample that was not 6' because the chamber at SilcoTek could not support a 6' sample.

GEAL Samples General Information

Trial	Material	Coating	Sample Configuration	Interaction Area (cm2)	Testing Length (days)	Color of Fluid	Average H2S Concentration (ppm)
Val	1010 Carbon Steel	None	6' 1/4" tube	263.25	46	Red	0.31
Val	304 Stainless Steel	None	6' 1/4" tube	283.11	46	Red	0.31
Val	1010 Carbon Steel	None	6' 1/4" tube	263.25	46	Red	0.31
Val	1010 Carbon Steel	None	6' 1/4" tube	263.25	46	Red	0.31
1	1010 Carbon Steel	None	6' 1/4" tube	263.25	43	Red	0.24
1	304 Stainless Steel	None	6' 1/4" tube	283.11	43	Red	0.24
1	1010 Carbon Steel	Silcolloy 1000	6' 1/4" tube	263.25*	43	Red	0.24
1	1010 Carbon Steel	Dursan	51" 1/4" tube	186.47*	43	Red	0.24
2	1010 Carbon Steel	None	6' 1/4" tube	263.25	26	Black	1.61
2	1010 Carbon Steel	Curran 1000 (incorrect mixture)	6' 1/4" tube	263.25*	11	Black	1.61
2	1010 Carbon Steel	Curran 1000 (incorrect mixture)	6' 1/4" tube	263.25*	15	Black	1.61
2	1010 Carbon Steel	Curran 1000 with PTFE	6' 1/4" tube	263.25*	26	Black	1.61
2	1010 Carbon Steel	Curralon with PTFE	6' 1/4" tube	263.25*	26	Black	1.61
3	1010 Carbon Steel	None	6' 1/4" tube	263.25	31	Black/Red	1.49
3	1010 Carbon Steel	Curran 1000 (correct mixture)	6' 1/4" tube	263.25*	31	Black/Red	1.49
3	1010 Carbon Steel	Curran 1000 with nano graphene	6' 1/4" tube	263.25*	31	Black/Red	1.49
3	1010 Carbon Steel	Curran 1000 with nano graphene and nano silicon carbide	6' 1/4" tube	263.25*	31	Black/Red	1.49
4	1010 Carbon Steel	None	6' 1/4" tube	263.25	22	Black	1.71
4	1010 Carbon Steel	Curran 1000 with self healing properties	6' 1/4" tube	263.25*	22	Black	1.71

Table 11-General information for the samples tested in the GEAL. *assumed the same ID as the uncoated carbon steel sample.

The color of the fluid during testing changed once the addition of ammonium hydroxide became necessary. As seen above, the validation trial and Test 1 had low hydrogen sulfide concentrations which did not require the use of ammonium hydroxide to maintain the pH, and the fluid in the system had a light red tint. During Test 2 the addition of ammonium was necessary and the fluid turned black. The discoloration was extensive enough to prevent the measurement of the flow rate and the determination of the hydrogen sulfide concentration. It is possible that there was too much ammonium added during Test 2 than required which resulted in the deep black discoloration. During Test 3 the ammonium was added more sparingly and the system would be black after the addition and transition back to a red tint. However, the pH was not as well maintained during Test 3 as it was during Test 2. There is a tradeoff with the addition of

ammonium between maintaining the pH and the discoloration of the system, and it was selected to allow for lower maintenance of the pH because if the discoloration becomes bad then data acquisition becomes challenging. During Test 4 the ammonium was added at the same rate as in Test 3, but the fluid turned black anyway. It did not reach a point where the rotameters could not be read, but it did not have the red tint that Test 3 had. A point worthy of note is that deposition on the samples is red by the time they are ready for inspection whether or not the fluid was black or red.

The information in Table 11 is important for quantifying the deposition on the samples. To compare the samples the weight change of the sample from before and after testing will be determined. However, to normalize this data across many different exposure times and surface area discrepancies the weight change per day per cm^2 will be calculated. Both of these values are calculated using the equations below with the data from both Tables 11 and 12.

$$\% \, Weight \, Change = \frac{Initial \, Weight - Final \, Weight}{Initial \, Weight}$$

$$\% \, Weight \, Change \left(\frac{1}{days * cm^2}\right) = \frac{\% \, Weight \, Change}{Testing \, Length * Interaction \, Area}$$

The last discrepancy between the trials to account for is the change in the corrosive and fouling environment. Therefore, weight change of each sample will be compared to the weight change of the carbon steel sample from that trial to obtain a comparison to a benchmark. The weight change data for each sample along with this analysis is presented below in Table 12.

GEAL Samples Weight Change Data

Trial	Material	Coating	Initial Weight (g)	Final Weight (g)	% Weight Change	% Weight Change per day per area (1/d*cm2)	Relative to Carbon Steel
Val	1010 Carbon Steel	None	224.23	232.56	3.71	3.064E-04	-
Val	304 Stainless Steel	None	185.29	185.19	-0.05	-3.839E-06	-
Val	1010 Carbon Steel	None	224.29	234.33	4.48	3.700E-04	-
Val	1010 Carbon Steel	None	225.84	234.07	3.64	3.006E-04	-
1	1010 Carbon Steel	None	224.65	228.31	1.63	1.440E-04	1.000
1	304 Stainless Steel	None	178.04	178.05	0.01	8.214E-07	0.006
1	1010 Carbon Steel	Silcolloy 1000	225.17	227.16	0.88	7.774E-05	0.540
1	1010 Carbon Steel	Dursan	159.35	160.58	0.77	9.603E-05	0.667
2	1010 Carbon Steel	None	219.79	232.37	5.72	8.357E-04	1.000
2	1010 Carbon Steel	Curran 1000 (incorrect mixture)	226.89	235.71	3.89	1.343E-03	1.607
2	1010 Carbon Steel	Curran 1000 (incorrect mixture)	227.06	237.32	4.52	1.145E-03	1.370
2	1010 Carbon Steel	Curran 1000 with PTFE	231.67	233.01	0.58	8.474E-05	0.101
2	1010 Carbon Steel	Curralon with PTFE	218.98	219.03	0.02	2.922E-06	0.003
3	1010 Carbon Steel	None	224.52	249.23	11.01	1.349E-03	1.000
3	1010 Carbon Steel	Curran 1000 (correct mixture)	223.78	223.55	-0.10	-1.259E-05	-0.009
3	1010 Carbon Steel	Curran 1000 with nano graphene	220.15	220.07	-0.04	-4.453E-06	-0.003
3	1010 Carbon Steel	Curran 1000 with nano graphene and nano silicon carbide	219.96	222.33	1.08	1.32E-04	0.098
4	1010 Carbon Steel	None	224.43	227.89	1.54	2.662E-04	1.000
4	1010 Carbon Steel	Curran 1000 with self healing properties	220.55	220.66	0.05	8.612E-06	0.032

Table 12-The weight change data for the samples tested in the GEAL.

The results of the weight change analysis display a full range of results varying from almost no weight gain to more than the carbon steel and everything in-between. The obvious standouts are the Curralon with PTFE, the Curran 1000 (correct mixture), and the Curran 1000 with nanographene. Each displayed very similar weight change data to that of stainless steel. It is a concern for both the Curran 1000 with and without the nanographene that there was a loss of material during testing which suggests that the coating is possibly being worn down. During long exposure in a plant setting this would result loss of the coating and fouling of the heat exchanger. The second tier coatings are the Curran 1000 with PTFE, the Curran 1000 with nanographene and nanosilicon carbide, and the Curran 1000 with self healing. These coatings significantly hindered the fouling of the tubes but were clearly a step behind the best coatings.

The rest of the coatings did not perform well, and should not be considered for this application. Given the data presented in Table 12, it seems as though Curralon with PTFE would be the best coating for this application. It sets itself apart from the Curran 1000 coatings for two reasons. First, it does not have the loss of material concern the Curran 1000 coating have as discussed earlier. Second, an incorrect mixture of the Curran 1000 would lead to extremely terrible performance as demonstrated during Test 2. However, Curralon is more difficult to apply to a heat exchanger tube than the Curran 1000 so it may not be the best choice for application reasons. These conclusions drawn here from the data in Table 12 will be supplemented with an analysis of the deposition on the tubes in the next section.

5.2.4 Deposition Analysis

The weight change data provides a comparison for the amount of deposition on the sample surfaces, but the samples must be inspected more closely to determine the differences in the deposition. Figures 55 through 68 are images of the samples after testing.

Figure 55-Deposition on the carbon steel sample tested during Test 1. Tick marks are 1/64th of an inch.

Figure 56-Deposition on the stainless steel sample tested during Test 1. Tick marks are 1/64th of an inch.
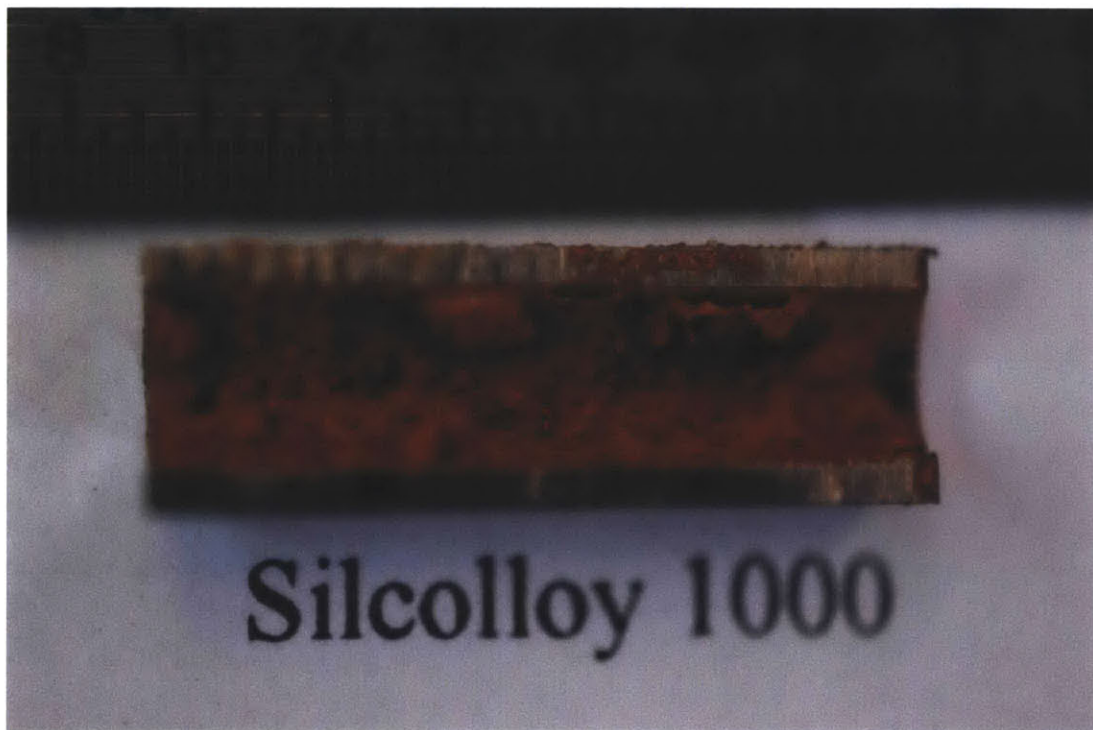
Figure 57-Deposition on the Silcolloy 1000 sample tested during Test 1. Tick marks are 1/64th of an inch.
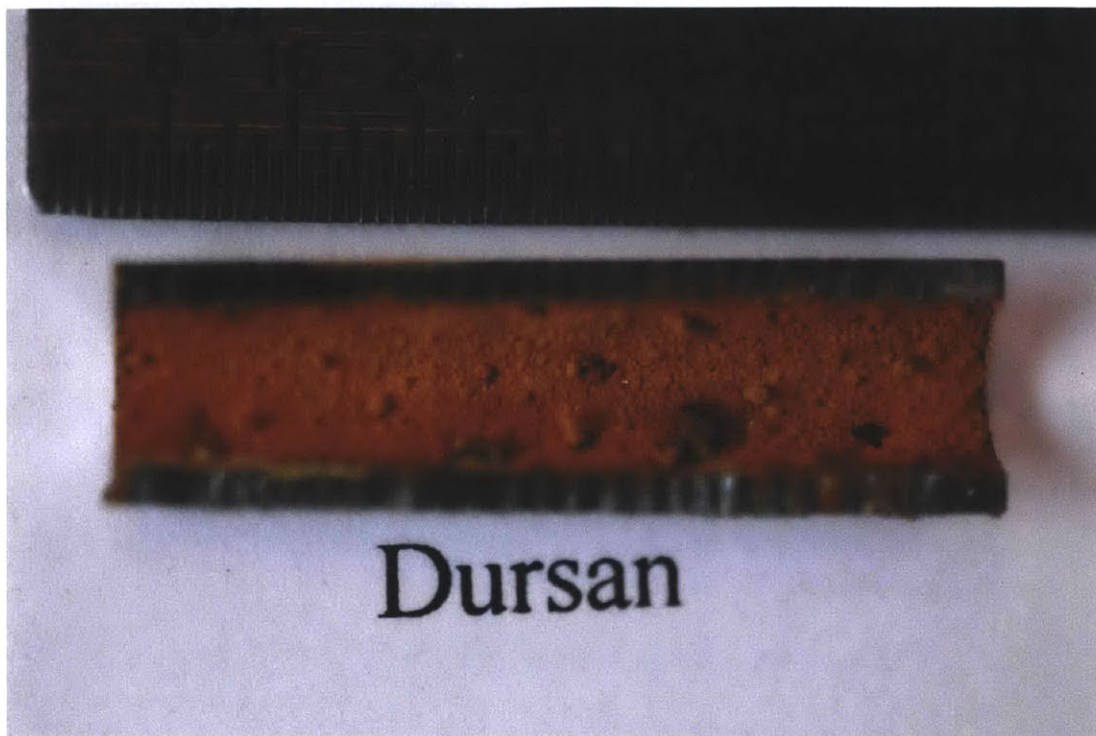
Figure 58-Deposition on the Dursan sample tested during Test 1. Tick marks are 1/64th of an inch.
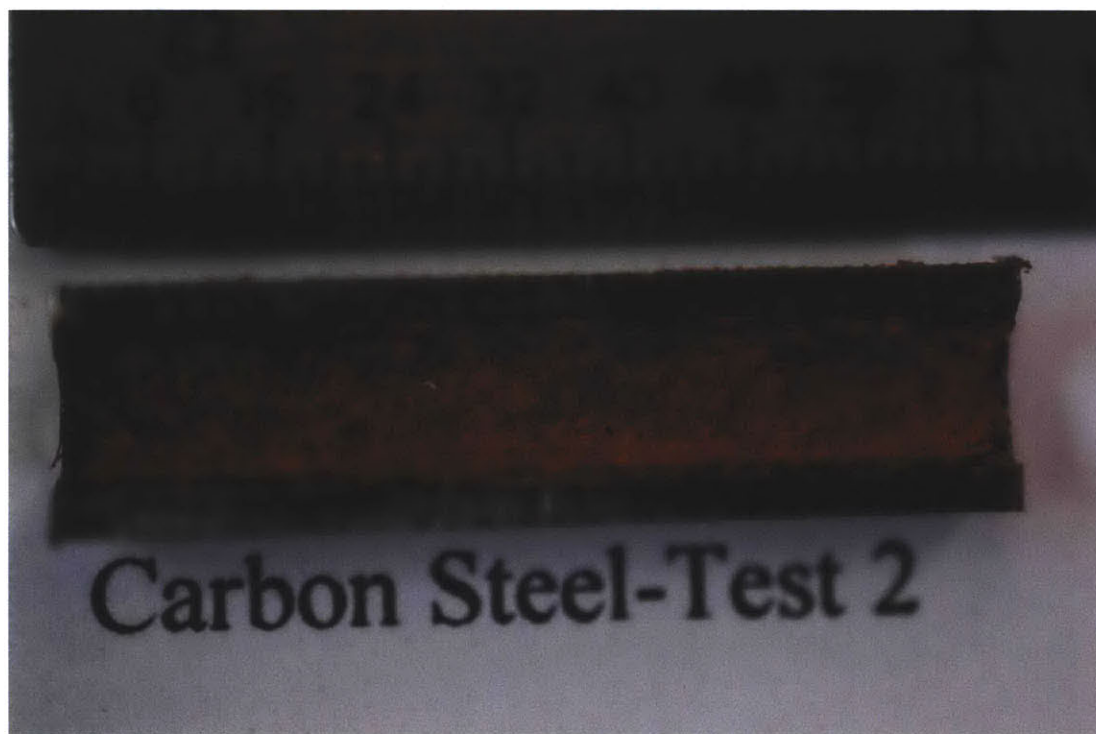
Figure 59-Deposition on the carbon steel sample tested during Test 2. Tick marks are 1/64th of an inch.

Figure 60-Deposition on the Curran 1000 sample tested during Test 2. Tick marks are 1/64th of an inch.
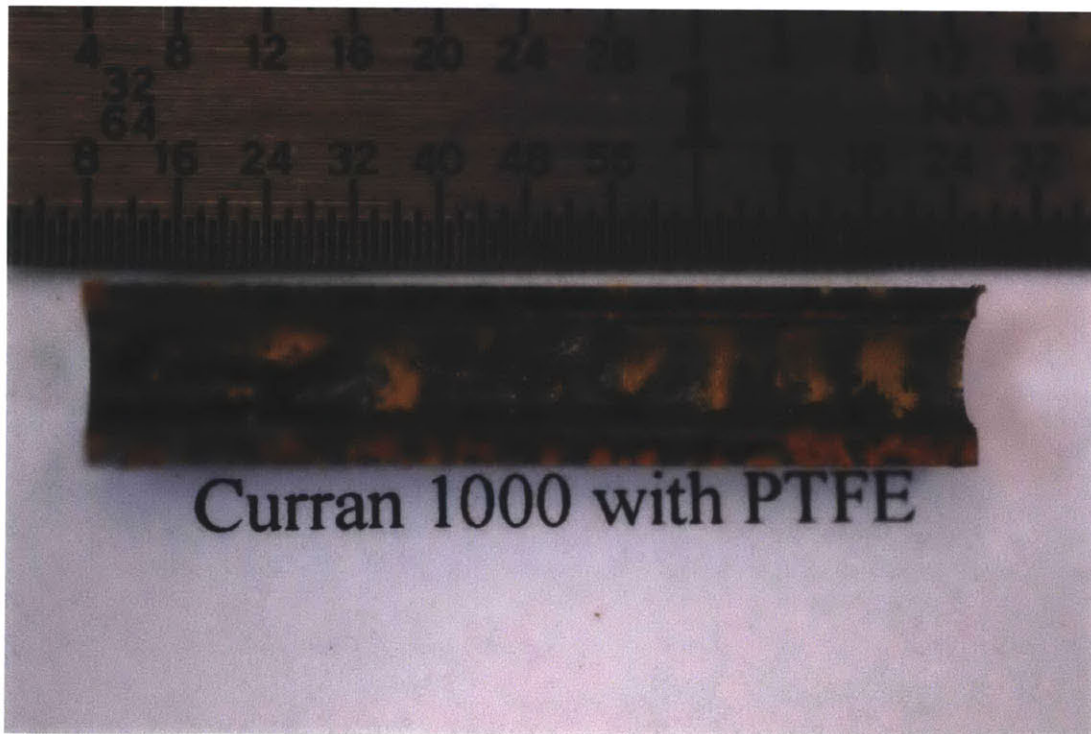
Figure 61-Deposition on the Curran 1000 with PTFE sample tested during Test 2. Tick marks are 1/64th of an inch.
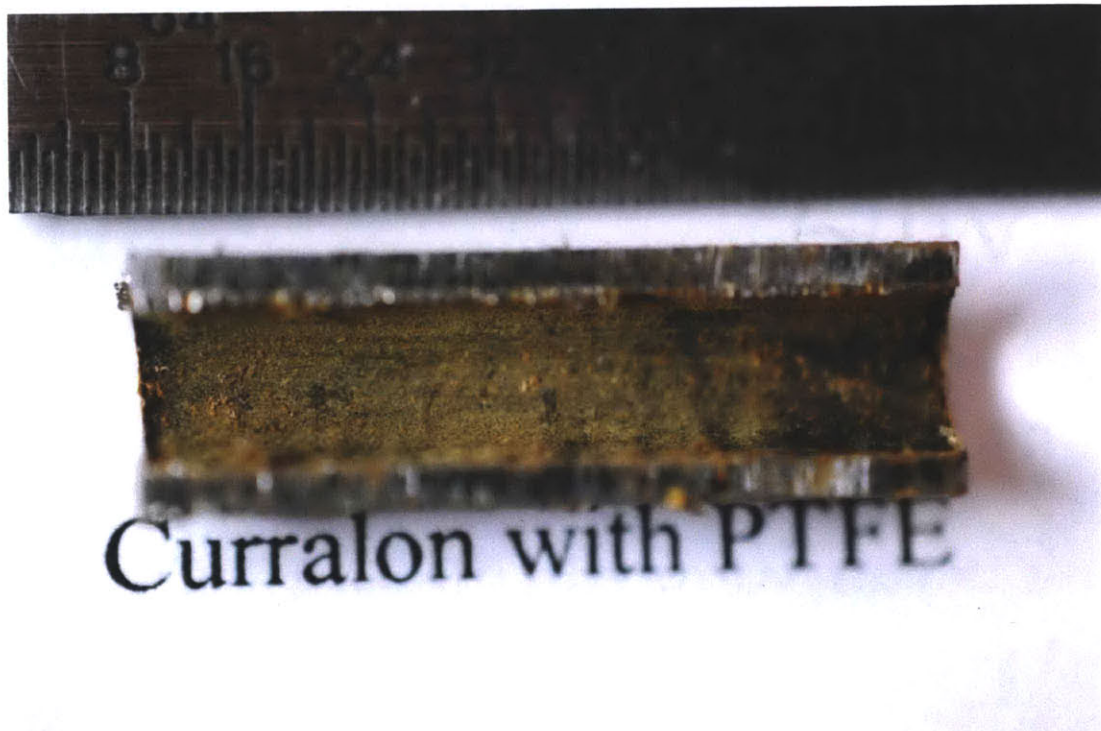
Figure 62-Deposition on the Curralon with PTFE sample tested during Test 2. Tick marks are 1/64th of an inch.
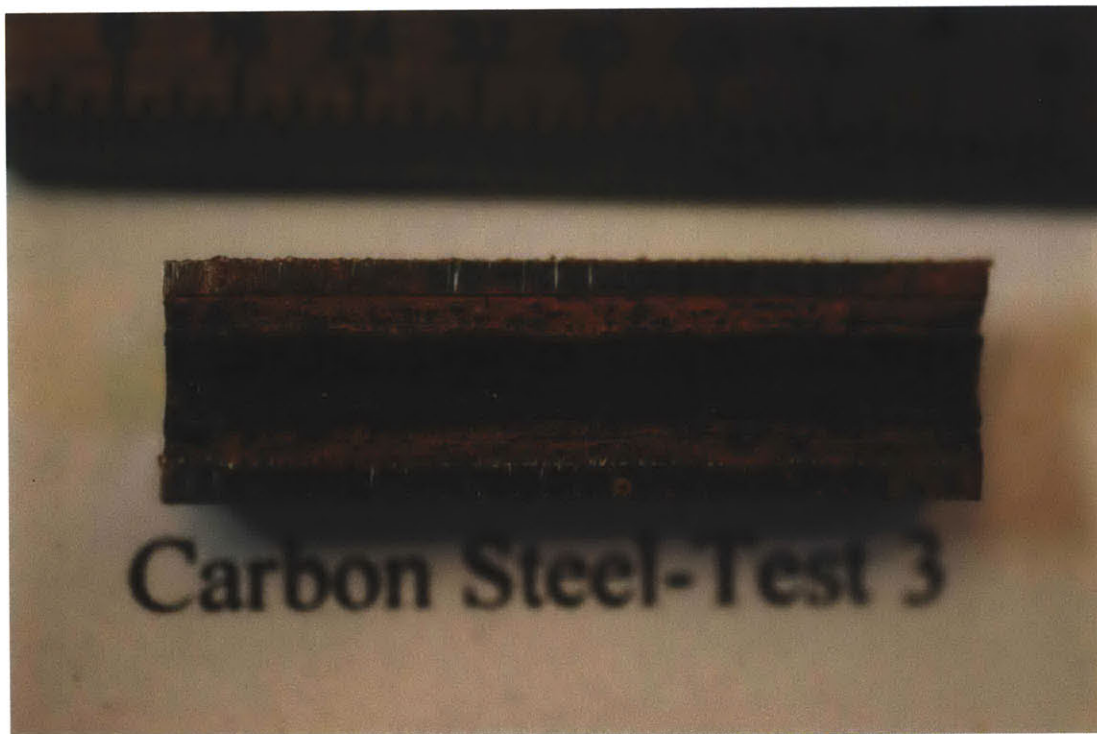
Figure 63-Deposition on the carbon steel sample tested during Test 3. Tick marks are 1/64th of an inch.
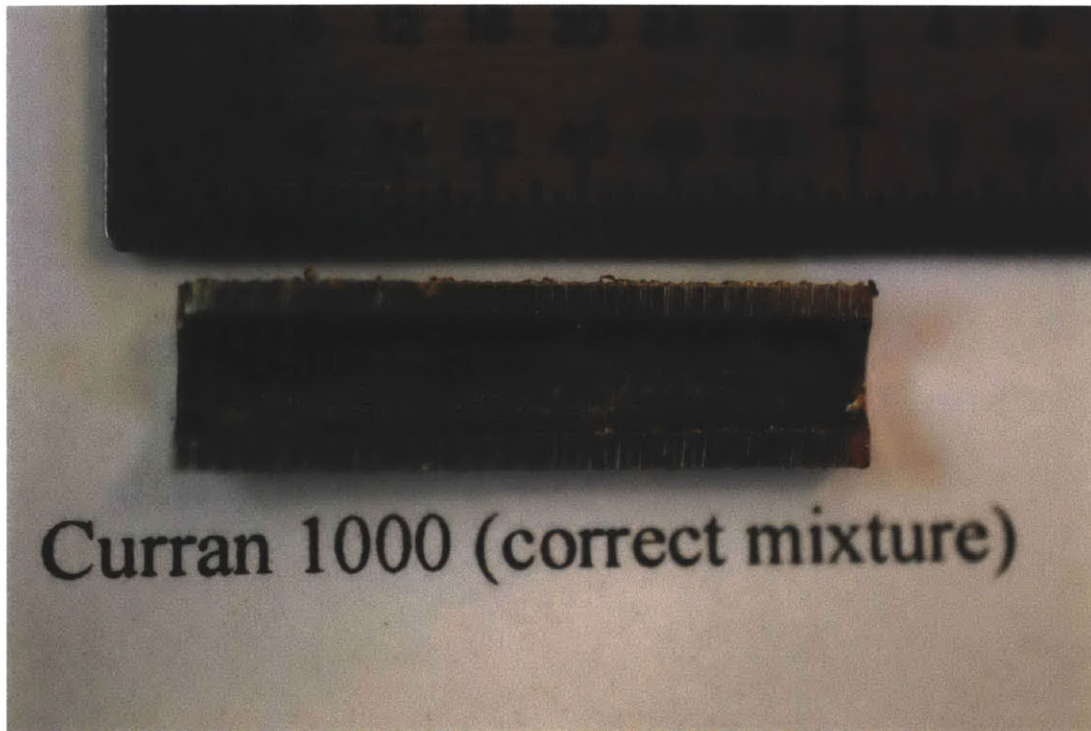
Figure 64-Deposition on the Curran 1000 sample tested during Test 3. Tick marks are 1/64th of an inch.
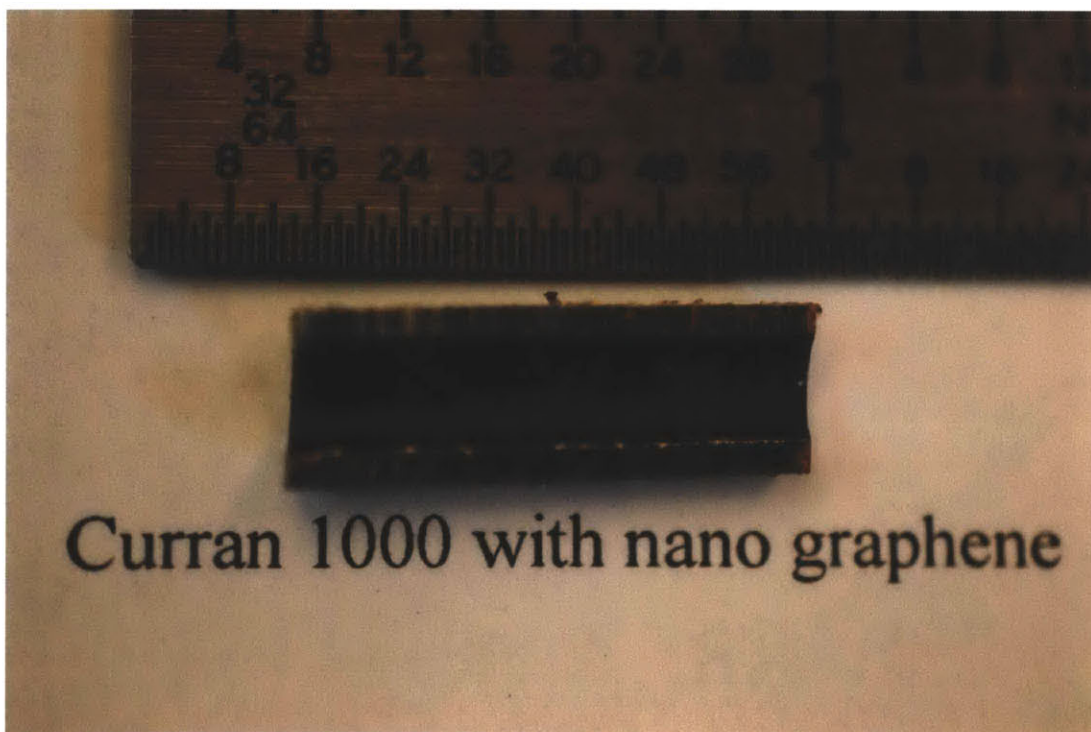
Figure 65-Deposition on the Curran 1000 with nanographene sample tested during Test 3. Tick marks are 1/64th of an inch.
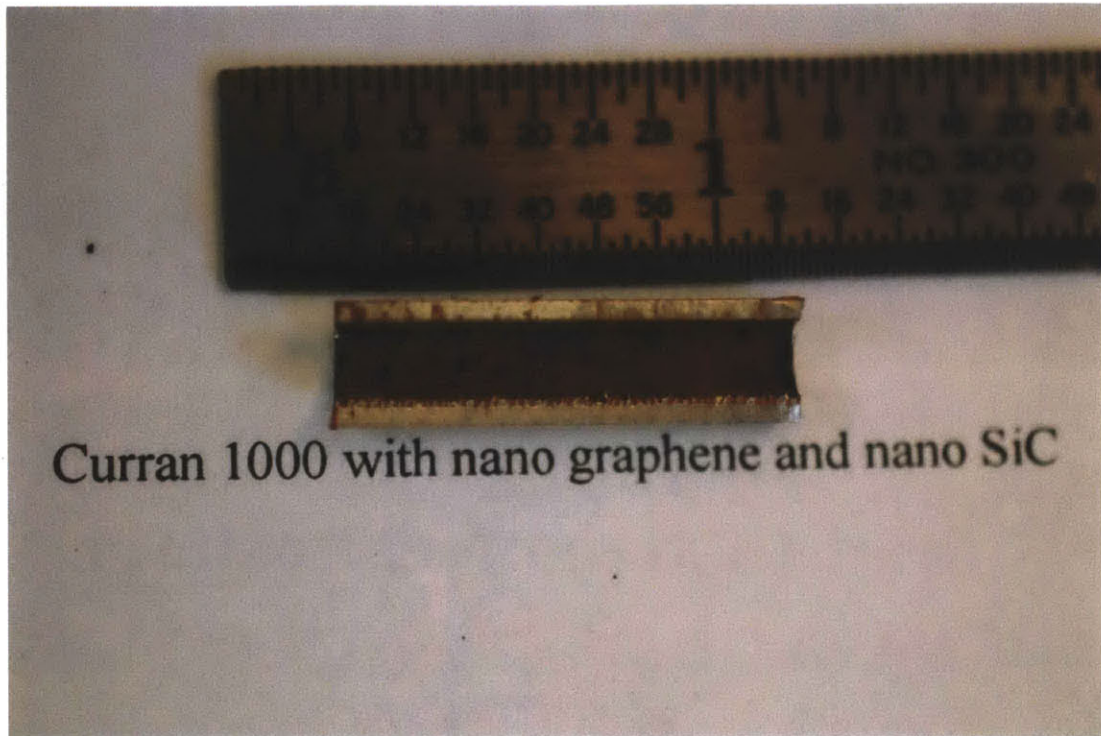
Figure 66-Deposition on the Curran 1000 with nanographene and nanosilicon carbide sample tested during Test 3. Tick marks are 1/64th of an inch.
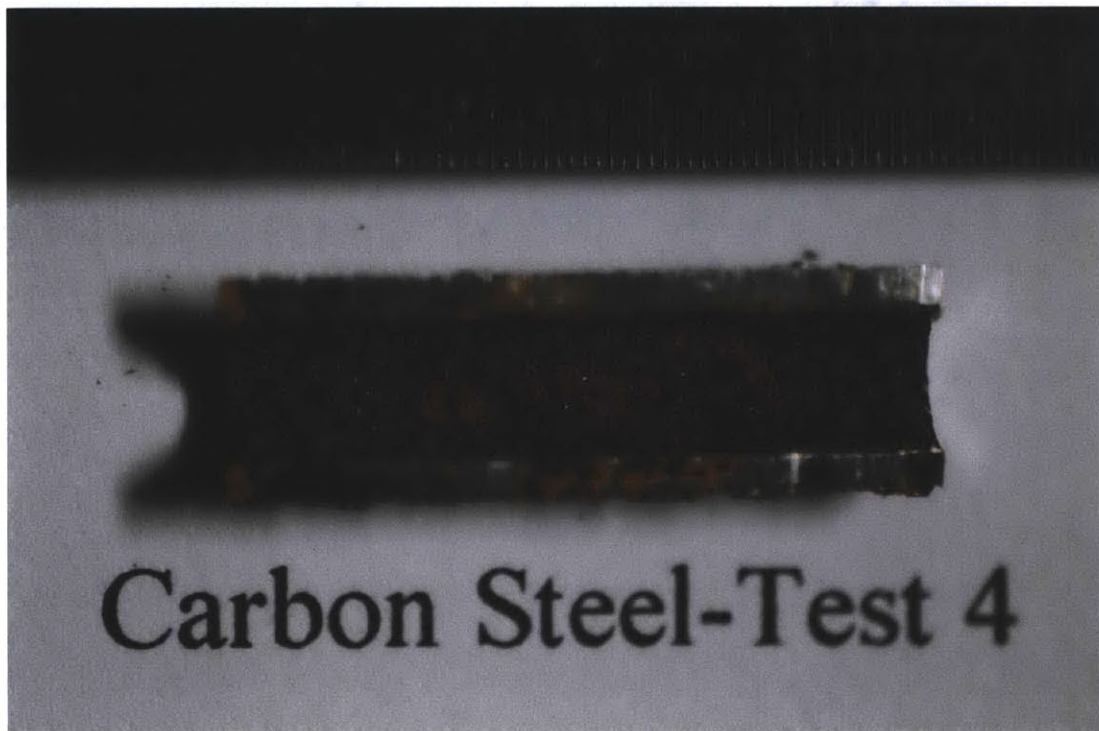
Figure 67-Deposition on the carbon steel sample tested during Test 4. Tick marks are 1/64th of an inch.

Figure 68-Deposition on the Curran 1000 with self healing tested during Test 4. Tick marks are 1/64th of an inch.

One of the more interesting observations is the difference between the carbon steel samples. The deposition on the sample from Test 1 was a light uniform powder while the sample from Test 2 had thicker, inconsistent deposition. While both of these samples displayed red deposition, the sample from Test 3 had a sub-layer of red deposition with a layer of black deposition on top. The increase in deposition on the samples from Tests 2 and 3 was due to the drastic increase in hydrogen sulfide during those tests, but it is unclear what prompted the two layer deposition in the Test 3 sample. The sample from Test 4 shows deposition similar to Test 2 in a smaller quantity.

Each of the coated samples displayed slightly different deposition that provided an insight into the performance of the surface. During Test 1, the stainless steel sample had minimal deposition with small areas where a thin light powder had attached itself. The advantage of using stainless steel is its continued resistance against both corrosion and fouling even after it has started. The opposite example of this is shown in the Silcolloy 1000 and Dursan samples. These samples display evidence of pitting because of the drastically increased deposition in some areas. It is likely that the coatings failed in these areas which lead to pitting corrosion which accelerated the

deposition process in these areas. The Dursan sample performed better than the Silcolloy 1000, but both did poorly enough that the difference between them is inconsequential.

During Test 2, the Curran 1000 sample displayed a surprisingly large amount of deposition which was later identified to be due to the coating being mixed incorrectly. The incorrect mixture allowed the sample to soak up water and for the fluid to permeate the coating which corroded the carbon steel. This sample had a larger weight gain than the carbon steel because of the weight gain from absorbing water. The other two samples both contained PTFE which had a large affect on the ability of the deposition to adhere to the surface. The deposition on these samples was light and easily removable with a single wipe of a cloth. The sample with the Curralon as the base did better than the one with the Curran 1000 as the base, but both were affective in slowing the fouling (it should be noted that the sample with the Curran 1000 with PTFE had the correct mixture for the Curran 1000).

During Test 3, the Curran 1000 was tested again along with the addition of nanoparticles. The Curran 1000 with the correct mixture did very well displaying only slight deposition that could be easily removed. The Curran 1000 with nanographene displayed even less deposition than the Curran 1000 which is only visible during a close inspection. While the Curran 1000 performs well by itself, it does appear that the nanographene enhances the surface's antifouling ability. While the nanographene helped the Curran 1000, the addition of nanosilicon carbide had the opposite effect. There was a considerable amount of mostly uniform deposition present on the Curran 1000 with nanographene and nanosilicon carbide sample which indicates the inability of the surface to prevent fouling rather than a breakdown in the coating due to pitting. The silicon carbide was added to increase the thermal conductivity of the coating, but it appears that this results in a loss of the protective capability of the coating. Therefore, the nanosilicon carbide should not be applied to coatings for this application.

During Test 4, the Curran 1000 with self healing performed well with a slight weight gain. However, upon visual inspection of the sample it appears that the coating has remained clear of any deposition. It is likely that most of the weight gain was due to the absorption of water by the

boehmite and not by any deposition on the coating. Therefore, the Curran 1000 with self healing properties should be included with the list of promising coatings from a corrosion and fouling perspective, but it should be noted that the intake of water will likely decrease the thermal conductivity of the coating.

5.2.5 Abrasion Resistance

Given the high cost to reapply the coating to the heat exchanger tubes in this application it is important that the selected coating be able to withstand prolonged exposure. The abrasion resistance should be quantified to determine each coatings resistance to erosion from the flow and potential to endure water lancing if necessary.   Thus, the Taber abrasion resistance was determined according to ASTM D 4060 with 1000 cycles of the CS-17 abrasion wheel with a 1000 g load. The results of this test are given below in Figure 69.

Taber Abraision Resistance Data

Figure 69-Taber abrasion resistance data for carbon steel and the six coatings from Curran International, Inc.

The standout coatings from the abrasion resistance tests are the Curran 1000 and the Curralon with PTFE which both displayed less weight loss than the carbon steel. The use of nanographene in the Curran 1000 results in a loss of abrasion resistance, and the addition of nanosilicon carbide likely further decreases the resistance. However, the uncertainty in the Curran 1000 with nanographene and nanosilicon carbide and the Curran 1000 with PTFE is large enough that it is difficult to draw conclusions. Although it does seem apparent that the addition of anything to the Curran 1000 nullifies its abrasion resistance advantage over carbon steel.

5.2.6 Economic Analysis

The final step is to determine the relative cost of each of the coating options available, and determine if they are practical to implement. This will be a rough analysis since the coating suppliers could not provide an exact price due to the unknowns involved with the potential order. However, this analysis should demonstrate the economic potential of applying a coating rather than using stainless steel. To determine the cost of 304 stainless steel and 1010 carbon steel, the price of the pipes on McMaster-Carr was used. The cost of 304 stainless steel (PN# 1750T156, 6' long, 1" OD, 0.902" ID) is $11.23 per foot, and 1010 carbon steel (PN# 7767T37, 6' long, 1" OD, 0.76" ID) is $3.38 per foot. As for the coatings, the Curran 1000 is $1.50 per foot with additives being $0.50 per foot, and the Curralon system is $10 per foot. SilcoTek was unable to provide a cost estimate because they would have to purchase new machinery for this order. The XPROTECT coating costs $0.457 per square meter for the material, prefinishing, and electrical plating. This translates to approximately $0.01 per foot for this application. This information is summarized in Table 13 below.

Heat Exchanger Tube Costs Per Foot

Tube Material	Coating	Cost ($/ft)
304 Stainless Steel	None	11.23
1010 Carbon Steel	Curran 1000	4.88
1010 Carbon Steel	Curran 1000 with self healing	5.38
1010 Carbon Steel	Curran 1000 with nanographene	5.38
1010 Carbon Steel	Curran 1000 with nanographene and nanosilicon carbide	5.88
1010 Carbon Steel	Curran 1000 with PTFE	5.38
1010 Carbon Steel	Curralon with PTFE	13.38
1010 Carbon Steel	XPROTECT	3.39

Table 13-The relative costs to build the DCT heat exchanger tubes with a variety of coatings and tube materials.

The main conclusion from this rough analysis is that there are many coatings that are economically viable. The Curran 1000 with nanographene and nanosilicon carbide is more expensive than its alternative Curran 1000 coatings because it has two additives. The only coating that is too expensive for this application is the Curralon with PTFE which is an important conclusion because it was one of the top performing coatings in terms of corrosion and fouling prevention. The rest of the coatings result in significant savings over stainless steel, but some are cheaper than others. It will ultimately be up to the sponsor to decide if the price difference between the coatings is enough to sway a decision, but more likely than not it will be the performance of the coatings in other areas that dictates the choice of coating.

6. Conclusions

6.1 Solar Receiver Study Conclusions

While the study to identify a nanosurface that could be applied to a solar thermal receiver did not achieve its goal, there was a considerable amount of information and conclusions drawn to narrow the search. The timeline for this project did not allow for multiple rounds of testing that was required. The main challenge involved in this work is the difficulty of maintaining a nanostructure at the high operating temperatures of this project. This first round of testing demonstrated that various candidate surfaces including nanosurfaces can be successfully fabricated, analyzed using the techniques established during this work, and insightful conclusions can be drawn. The main conclusions drawn from this work are outlined below.

- Established analytical techniques to: 1) evaluate optimum film thickness (Macleod, section 3.4.1.1), 2) measure reflectivity/absorptivity/emissivity (section 5.1.2), and 3) determine the solar selectivity and thermal efficiency of candidate surfaces from reflectivity data where established (section 5.1.2.1).

- Thermal efficiency not the solar selectivity ratio (α/ε) was determined to be the proper metric to compare the thermal performance of the candidate surfaces.

- The NiO sample had the highest solar selectivity ratio (α/ε), but not always the highest thermal efficiency.

- At a higher operating temperature of 1,000 °C the NiO sample showed the highest thermal efficiency due to its solar selectivity. In other words, the reduced emittance results in the highest thermal efficiency of all candidate materials at very high temperatures where emittance losses are extreme, and this region begins at 1000 °C.

- At the operating temperature of 750 °C and incident power of 500 kW the SiC showed the highest thermal efficiency of 78.4%, followed by 617 at 76.3%, and NiO had an efficiency of 71.3%. The NiO sample's lower efficiency, despite it solar selectivity, results from the penalty of its decreased absorptivity in the solar bandwidth.

- The reflectivity/absorptivity data, Figure 40, indicates that the Pt layer of the NiO/Pt/617 and 617/Pt nano-layered systems likely failed, and therefore this solar selective surface of 550 nm of nickel oxide (NiO) on 150 nm of platinum did not exhibit favorable optical properties compared to Inconel 617 or NiO samples.

- Given the difficulty of producing a solar selective surface that can operate at 750 °C, it is possible that at the operating temperature of 750 °C and solar flux of 500 kW a black body would be a more practical choice than a solar selective surface.

6.1.1 Solar Receiver Future Work

At the operating temperatures for the design of this solar receiver, it has been shown that a black body surface should be investigated rather than a selective surface. Therefore, the next step would be to investigate the potential use of carbon nanotubes which create a surface with the highest absorptivity/emissivity of any known material. However, similar to the nanosurfaces already investigated and tested for this application, the thermal stability of the CNTs is extremely important and would need to be tested for stability. This will also require testing of different substrates for the CNTs to determine a substrate that does not diffuse into the CNTs and disrupt their properties. Once a nanosurface is identified the main limitations of knowledge would be the durability of the surface in the environment of the site (factors beyond oxidation), and the surface's ability to cope with the daily thermal loading and unloading.

6.2 Geothermal Antifouling Study Conclusions

Given the timeline for this project, these are the conclusions near the end of the first round of testing with the GEAL. There have been many failed coatings along with more than one that has produced results similar to that of stainless steel. However, identification of an ideal coating for this application involves the consideration of other features of the coating beside its fouling resistance which have been discussed in the previous chapter and will be reviewed here. The main conclusions are outlined below.

- An effective apparatus and testing method for fouling of heat exchanger tube samples has been build and established. The main challenge involved with operation of the GEAL was maintaining chemistry control.

- The use of stainless steel for heat exchanger tubes hinders the heat transfer capacity of the DCT, and the application of a coating to carbon steel allows for higher heat transfer capacity along with similar fouling resistance.

- Nanoparticles were shown to increase the thermal conductivity of the coatings, but not necessarily enhance the corrosion and fouling resistance. The addition of the nanographene particles did not adversely affect the corrosion and fouling resistance, but the nanosilicon carbide particle negatively impacted the surface.

- The addition of a PTFE layer to the coatings was shown to enhance the corrosion and fouling resistance, but drastically decreased the thermal conductivity.

- The best coatings at inhibiting corrosion and fouling in the hydrogen sulfide environment tested were the Curran 1000, the Curran 1000 with nanographene, the Curran 1000 with self healing, and the Curralon with PTFE coating. There is little difference between the Curran 1000 with micro or nanographene, but creating the correct mixture of the coating is extremely important.

- The Curran 1000 and the Curralon with PTFE were identified to possess increased abrasion resistance compared to carbon steel. The Curran 1000 with nanographene demonstrated similar abrasion resistance to carbon steel.

- The cost of application of most of the coatings is economical over stainless steel. The only coating that is not economical over stainless steel was the Curralon with PTFE coating.

- The coatings of promise and in need of more testing are the Curran 1000, the Curran 1000 with nanographene, and the Curran 1000 with self healing for their good corrosion and fouling prevention and low cost. Also, none of these coatings have a very undesirable trait that rules them out immediately.

- Among these three promising coatings the Curran 1000 with nanographene should be considered the front runner because it enhances both the thermal conductivity and corrosion and fouling resistance compared to the Curran 1000. The Curran 1000 does possess superior abrasion resistance, but the Curran 1000 with nanographene has a similar abrasion resistance to carbon steel which has been proven to be adequate for water lancing. The Curran 1000 with self healing falls behind because it has a lower abrasion resistance compared to the other two, and will likely lose its best feature, its thermal conductivity, after it absorbs water.

6.2.1 Geothermal Antifouling Future Work

Before the selection of a coating there will be one more coatings tested along with a second round of testing consisting of the more promising samples. There is a promising coating called XPROTECT that is manufactured by Xtalic which will be tested to conclude the first round of testing. There will then be an evaluation period where the second round of testing is planned.

The most promising coatings will be tested and inserted into the GEAL for an extended period of time to determine their performance during longer exposure. Following this round of testing, a recommendation will be made to ENEL on which coating to pursue. The next step will likely involve a test at the site to assess the performance of the coating in industrial conditions.

6.3 Acknowledgments

Bibliography

Agnihotri and Gupta. "Solar Selective Surfaces." John Wiley & Sons (1981).

Akaku. "Geothermal study of mineral precipitation from geothermal waters at the fushime field, Kyushu, Japan." Geothermics 19.5 (1990): 455-467.

Alaruri, Sami, Lisa Bianchini and Andrew Brewington. "Effective spectral emissivity measurements of superalloys and YSZ thermal barrier coating at high temperatures using a 1.6 um single wavelength pyrometer." Optics and Lasers in Engineering (1997).

Alexopoulos, Spiros and Bernhard Hoffschmidt. "Solar tower power plant in Germany and future perspectives of the development of the technology in Greece and Cyprus." Renewable Energy (2010).

Angelino, Gianfranco and Costante Invernizzi. "Binary coversion cycles for concentrating solar power technology." Solar Energy (2008).

ASTM Int'l. "Standard tables for reference solar spectral irradiances: Direct normal and hemispherical on 37 tilted surface, G-173-03." 2007.

Baltazar, et al. "Silica scale inhibition experiments: geogard SX application on geothermal brine with ultra high concentration of SiO2." Geothermal Resources Council Transactions (1997).

Barrera, Viveros and Morales. "Preparation of selective surfaces of black cobalt by the sol-gel process." WREC (1996).

Bayati, Janghorban and Shariat. "Thermal stability of corrosion resistance of electroplated black chromium solar selective absorber." Electroplating & Finishing 28.8 (2009): 12-16.

Begtrup, et al. "Extreme thermal stability of carbon nanotubes." Physics Status Solid 11 (2007): 3960-3963.

Blodgett, Leslie and Kara Slack. "Geothermal 101: Basics of Geothermal Energy Production and Use." 2009.

Blum, William and George B. Hogaboom. Principles of Electroplating and Electroforming. McGraw-Hill Book Company, 1949.

Borrmann, Johnston and McBrearty. "Nano-structured calcium silicate-a solution to the formation of silica scale in geothermal water." Geothermal Resources Council Transactions (2009).

Bostrom, et al. "Structure and morphology of nickel-alumina/silica solar thermal selective absorbers." Journal of Non-Crystalline Solids (2010).

Bostrom, Wackelgard and Westin. "Anti-reflection coating for solution-chemically derived nickel-alumina solar absorbers." Solar Energy Materials & Solar Cells (2003).

—. "Solution-chemical derived nickel-alumina coatings for thermal solar absorbers." Solar Energy (2003).

Braendle, Stefan. "Collector coatings evlove from black paint to selective surfaces." Solar Industry (2010).

Brown, Zipfel and Dunstall. "Investigations of the onset of silica scaling around circular cylinders." Geothermal Resources Council Transactions 23 (1999).

Cezairliyan and Miiller. "A dynamic technique for measuring normal spectral emissivity of electrically conducting solids at high temperature with a high-speed spatial scanning pyrometer." International Journal of Thermophysics 14.5 (1993).

Chan, et al. "Geothermal transient fouling heat transfer measurements." Fouling of Heat Transfer Surfaces (1982).

—. "Silica fouling of heat transfer equipment-experiments and model." Journal of Heat Transfer 110 (1988).

Chen, X.H., et al. "Corrosion behavior of carbon nanotubes-Ni composite coating." Surface & Coatings Technology (2005).

Criaud and Fouillac. "Sulfide scaling in low enthalpy geothermal environments: A survey." Geothermics 18.1/2 (1989): 73-81.

Cuomo, J. J., J. F. Ziegler and J. M. Woodall. "A new concept for solar energy conversion." Applied Physics Letters 26.10 (1975).

Cverna, Fran. Thermal Properties of Metals. ASM International, Materials Properties Database Committee, n.d.

Daniels and Farrington. Direct use of the sun's energy. New Haven: Yale University Press, 1974.

Datta. "Materials-use in and developments for solar energy applications." Clean and Safe Energy Forever 3 (1990).

Demadis, et al. "2D and 3D alkaline earth metal carbonxyphosphonate hybrids: Anti-corrosion coatings for metal surfaces." Journal of Solid State Chemistry (2008).

Esposito, et al. "Fabrication of optimization of highly efficient cermet-based spectrally selective coatings for high operating temperatures." Thin Solid Films (2009).

Facts about Solar Energy. Solar Energy History. 2005. <http://www.facts-about-solar-energy.com/solar-energy-history.html>.

Fend, Thomas, et al. "Two novel high-porosity materials as volumetric receivers for concentrated solar radiation." Solar Energy Materials & Solar Cells (2004).

Fridleifsson, Ingvar and Derek Freeston. "Geothermal energy research and development." Geothermics 23.2 (1994): 175-214.

Galione, et al. "Origin of solar thermal selectivity and interference effects in nickel-alumina nanostructured films." Surface & Coatings Technology (2009).

Gallup and Barcelon. "Investigations of organic inhibitors for silica scale control from geothermal brines-II." Geothermics (2005).

Gallup, Darrell. "Production engineering in geothermal technology: A review." Geothermics (2009).

Gillette. "Selectively emissive materials for solar heat absorbers." Solar Energy (1960).

Goldstein, Joseph I., et al. Scanning Electron Microscopy and X-Ray Microanalysis. New York and London: Plenum Press, 1992.

Gorrepati, et al. "Silica precipitation in acidic solutions: mechanisms, pH effect, and salt effect." Langmuir Article (2010).

Greene, Finfrock and Ivrine. "Total hemispherical emissivity of oxidized Inconel 718 in the temperature range 300-1000 C." Experimental Thermal and Fluid Science (2000).

Guinier, A. X-Ray Diffraction: In Crystals, Imperfect Crystals, and Amorphous Bodies. San Francisco and London: W.H. Freeman and Company, 1963.

Hass, et al. "Reflectance, solar absorptivity, and thermal emissivity of SiO2-coated aluminum." Applied Optics (1969).

Hernandez, et al. "Optical fiber reflectometer coupled with a solar concentrator to determine solar reflectivity and absorptivity at high temperature." Journal of Solar Energy Engineering (1999).

Honegger, et al. "Detailed study of sulfide scaling at la courneuve nord, a geothermal exploitation of the paris basin, france." Geothermics 18.1/2 (1989): 137-144.

Hosseini, Smith and Critchley. "Investigation of molybdenum black coatings for use as solar selective absorbers." Surface Technology (1983).

Inagaki, Motomura and Ogata. "Microbial silica deposition in geothermal hot waters." Applied Microbiol Biotechnol (2003).

Incropera, et al. Fundamentals of Heat and Mass Transfer. John Wiley & Sons, Inc., 2007.

Iqbal, Fish and Starling. "Advantages of using mixtures as working fluids in geothermal binary cycles." University of Oklahoma (n.d.).

—. "Isobutane geothermal binary cycle sensitivity analysis." University of Oklahoma (n.d.).

Jacobson, et al. "Scale and corrosion parameters at a geothermal loop experimental facility." Journal of testing and evaluation (1981).

Jarvinen, Philip O. "Solar-Heated-Air Receivers." Solar Energy 19 (1975): 39-147.

Jaworske. "Brazing of graphite fibers to Inconel 718." International SAMPE Technical Conference (2000).

Jones, A.R., et al. "Nanocrystalline Ni-W alloy coating for engineering applications." Plating & Surface Finishing (2010).

Jorgensen, Schissel and Burrows. "Optical properties of high-temperature materials for direct absorption receivers." Solar Energy Materials (1986).

Kaltenbach, Graf and Kohl. "Assessment of diffusion processes in thin films." Solar Energy Materials & Solar Cells (1998).

Kandalkar, et al. "Synthesis of cobalt oxide interconnected flacks and nano-worms structures using low temperature chemical bath deposition." Journal of Alloys and Compounds (2008).

Karabelas, et al. "Characteristics of scales from the Milos Geothermal Plant." 18.1/2 (1989): 169-174.

Katumba, et al. "Optical, thermal and structural characterisitcs of carbon nanoparticles embedded in ZnO and NiO as selective absorbers." Solar Energy Materials & Solar Cells (2008).

—. "Solar selective absorber functionality of carbon nanoparticles embedded in SiO2, ZnO and NiO matrices." Physica Status Solidi (2007).

—. "The investigation of carbon nanoparticles embedded in ZnO and NiO as selective solar absorber surfaces." Solar Collector Technologies and Systems (2007).

Kirilov, et al. "A high effective selective absorbing coating for solar thermal collectors." Diffusion and Defect Data Pt. B Solid State Phenomena (2010).

Kokoropoulos and Evans. "Infrared spectral emissivities of cobalt oxide and nickel oxide." Solar Energy (1964).

Kokoropoulos, Salam and Daniels. "Selective radiation coatings, preparation and high temperature stability." Solar Energy (1959).

Kreith, Frank and Jan F. Kreider. Principles of Solar Engineering. Hemisphere Publishing Corporation, 1978.

Kumlutas, Dilek and Ismail Tavman. "A numerical and experimental study of thermal conductivity of particle filled polymer composites." Journal of Thermoplastic Composite Materials (2006).

Kung. "Rough metallic selective surfaces for solar energy applications." Solar & Wind Technology 3.2 (1986): 147-155.

Lanxner and Elgat. "Solar selective absorber coating for high service temperatures, produced by plasma sputtering." Proceeding of SPIE-The International Society for Optical Engineering 1272 (1990): 240-249.

Lei, Hao, et al. "Preparation and thermal stability on non-vacuum high temperature solar selective absorbing coatings." Chinese Science Bulletin (2009).

—. "Thermal stability of nitride solar selective absorbing coatings used in high temperature parabolic trough current." Science China: Technological Sciences (n.d.).

Lewis and Ralph. "A DOE-funded design study for pioneer baseload application of an advanced geothermal binary cycle at a utility plant in western Utah." POWER Engineers Inc. (2002).

Lewis, Nathan S. "Toward Cost-Effective Solar Energy Use." Science 315 (2007): 798-801.

Lin, et al. Nano water paint having nano particles surfaced with self-assembly monolayers. US Patent Application Publication: Patent US 20060063873 A1. 2006.

Lira-Cantu, Monica, et al. "Electrochemical deposition of black nickel solar absorber coatings n stainless steel AISI316L for thermal solar cells." Solar Energy Materials & Solar Cells (2004).

Liu, Hongqin, et al. "Preparation of super hydrophobic coatings on zinc as effective corrosion

barriers." Applied Materials & Interfaces 1.6 (2009): 1150-1153.

Ma, Houyi, et al. "The influence of hydrogen sulfide on corrosion of iron under different conditions." Corrosion Science (1999).

Madrigal, Alexis. Powering the Dream: The History and Promise of Green Technology. Da Capo Press, 2011.

Mareichev, et al. "Thermoradiational characteristics of thin-layer black-chrome coatings on metallic surfaces." Applied Solar Energy 20 (1984).

McDonald, G. "A preliminary study of a solar selective coating system using a black cobalt oxide for high temperature solar collectors." Thin Solid Films (1980).

Moller and Weare. "Technology for increasing geothermal energy productivity." University of California-San Diego (2004).

Neuer and Jaroma-Weiland. "Spectral and total emissivity of high-temperature materials." International Journal of Thermophysics 19.3 (1998).

Neuer, Kochendorger and Gern. "High temperature behaviour of the spectral and total emissivity of CMC materials." High Temperature-High Pressures (1996).

Nielsen, Marie Bech, et al. "Concentrated Solar Power in Sahara." (2009).

Oelhafen and Schuler. "Nanostructured materials for solar energy conversions." Solar Energy (2004).

Oloomi, Saboonchi and Sedaghat. "Effects on thin film thickness on emittance, reflectance, and transmittance of nano scale multilayers." International Journal of the Physical Sciences 5 (2010): 465-469.

Papini, Marie. "Influence of sol-gel SiO2/TiO2 protective coatings on the optical and thermal properties of nickel-phosphorus selective surfaces." Journal of Applied Physics (1991).

Phalippou, Jean. Sol-Gel: A low temperature process for the materials of the new millennium. 2000. <http://www.solgel.com/articles/June00/phalip/introsolgel.htm>.

Pompei, Francesco. "A certified-emissivity black body for calibrating infrared thermometers." Sensor Technology and Design (2002).

Sainte-Catherine, et al. "Study of dynamic absorptivity at 10.6 um and 1.0 um wavelengths as a function of temperature." Journal de Physique (1991).

Sattler, Klaus D. "Nanoparticles and Quantum Dots." CRC Press (2001-2-3).

Schell, Steve. "Design and evaluation of esolar's heliostat fields." Solar Energy (2010).

Sellaiyan, et al. "Understanding the effect of nanoporosity on optimizing the performance of self-healing materials for anti-corrosion applications." Journal of Physics: Conference Series (2011).

Shi, Xianming. "On the use of nanotechnology to manage steel corrosion." Bentham Science Publishers Ltd. (2010).

Special Metals Corporation. "Inconel alloy 617." 2005.

Sreevatsa, Sreeya and Haim Grebel. "Carbon nanotube structures as ionic barriers: A new corrosion prevention concept." ECS Transactions (2009).

"Standard Test Method for Determination of Solar Reflectance Near Ambient Temperature using a portable solar reflectometer." C1549-09, ASTM Int'l (n.d.).

"Standard Test Method for Total Emittance of Surfaces up to 1400 C." C 835-06, Int'l (n.d.).

Subramaniam and Vattoliparambil. Process for preparing dispersion additives useful for corrosion protective coatings. Patent US 20060138713 A1. 2006.

Sugama, T. "Cerium actete-modified aminopropylsilane triol: A precursor of corrosion-preventing coating for aluminum-finned condensers." JCT Research 2.8 (2005).

—. "Polyphenylenesulfide/montomorillonite clay nanocomposite coatings: their efficacy in protecting steel against corrosion." Materials Letters (2006).

Sugama, Toshifumi and Keith Gawlik. "Anti-silica fouling coatings in geothermal environments." Materials Letters (2002).

Sugama, Toshifumi. "High Performance Coating Materials." Brookhaven National Lab (2006).

Sugama, Toshifumi, Thomas Butcher and Lynne Ecker. "Experience with the development of advanced materials for geothermal systems." The American Ceramic Society (2011).

Surface Optics Corporation. "Hemispherical Directional Reflectance (HDR) Measurements on Five (5) M.I.T. Sample Coupons (6.1, 6P.1, 6PN.2, S.1, and N.1)." 2011.

Suryanarayana, C. and M. Grant Norton. X-Ray Diffraction: A Practical Approach. New York, New York: Plenum Press, 1998.

Tabak, John. Solar and Geothermal Energy. New York, New York: Facts on File, Inc., 2009.

Tapping and Davidson. "The composition of thin films formed on stainless steel in H2S-saturated water." National Resource Consul of Canada (1984).

Telegdi, J., T. Rigo and E. Kalman. "Nanolayer barriers for inhibition of copper corrosion." Maney for the Institute of Materials, Minerals, and Mining (2004).

Thornton and Lamb. "Sputter-deposited Pt-Al2O3 graded cermet selective absorber coatings." Solar Energy Materials 9.4 (1984): 415-431.

—. "Thermal stability studies of sputter-deposited multilayer selective absorber coatings." Thin Solid Films (1982).

Thornton, Penfold and Lamb. "Sputter-deposited Al2O3/Mo/Al2O3 selective absorber coatings." Thin Solid Films 72.1 (1980): 101-109.

Timans. "Emissivity of silicon at elevated temperatures." Journal of Applied Physics (1993).

Tuteja, Anish, et al. "Design parameters for superhydrophobicity and superoleophobicity." MRS Bulletin 33 (2008).

Varanasi, et al. "Dynamic wetting on superhydrophobic surfaces: droplet impact and wetting hysteresis." IEEE Intersociety Conference on Thermal and Thermomechanical Phenomena in Electronic Systems (2010).

Wall, Chuang and Ishida. "Exergy Study of the Kalina Cycle." ASME 10-3 (1989): 73-77.

Wardle, et al. "Fabrication and multifunctional properties of a hybrid laminate with aligned carbon nanotube grown in situ." Composites Science and Technology (2008).

—. "High-yield growth and morphology control of aligned carbon nanotubes on ceramic fibers for multifunctional enhancement of structural composites." Carbon (2008).

Wardle, Hart and Garcia. "Joining prepreg composite interfaces with aligned carbon nanotubes." Composites: Part A (2008).

Wazwaz, Salmi and Bes. "The effects of nickel-pigmented aluminum oxide selective coating over aluminum alloy on the optical properties and themal efficiency of the selective absorber prepared by alternative and reverse periodic plating technique." Energy Conversion and Management (2010).

Wesoff, Eric. "Update: Solar Junction Breaking CPV Efficiency Records, Raising $30M." greentechmedia (2011).

Wu, Lili, et al. "Synthesis and characteristics of NiO nanowire by a solution method." Materials Letters (2004).

Yang, Qing, et al. "Synthesis of NiO nanowires by a sol-gel process." Materials Letters (2005).

Yao, Bin, et al. "Corrosion inhibition of carbon steel by polyaniline nanofibers." <u>Materials Letters</u> (2008).

Yianoulis and Giannouli. "Thin solid films and nanomaterials for solar energy conversion and energy saving applications." <u>Journal of Nano Research</u> 2 (2008): 49-60.

Zhai, Lei, et al. "Patterned superhydrophobic surfaces: Toward a synthetic mimic of the Namid Desert Bettle." <u>Nano Letters</u> (2006).

—. "Stable superhydrophobic coatings from polyelectrolyte multilayers." <u>Nano Letters</u> (2004).

Zhao, Shuxi and Ewa Wackelgard. "Optimization of solar absorbing three-layer coatings." <u>Solar Energy Materials & Solar Cells</u> (2005).

Appendices

GEAL Design Calculations

Reservoir Heater Calculation

This calculation is done to determine the feasibility of using the parameters given for the reservoir in our experimental loop. The calculation will be done with a velocity of .27 m/s and .08 m/s which, respectively, translate to matching the Reynold's number of the system, and the lowest velocity possible to remain in the turbulent region.

Given: 4 samples, 1" I.D. tube samples, 1800 W heater, 10 °C delta T across reservoir

Assumptions: No losses to environment, the insertion of hydrogen sulfide and argon has a negligible effect on the mass and energy balance of the system

$$\dot{m}_{out} = 4 * A * \rho * v$$

$$\dot{m}_{out} = 4\pi \left(\frac{.0254\,m}{2}\right)^2 997.1\frac{kg}{m^3} 0.27\frac{m}{s} = 1.09\frac{kg}{s}$$

To conserve mass,

$$\dot{m}_{out} = \dot{m}_{in}$$

To conserve energy,

$$\frac{dE}{dt} = 1800\,W + \dot{m}_{in}c_p T_{in} - \dot{m}_{out}c_p T_{out}$$

$$\frac{dE}{dt} = 1800\,W - 1.09\frac{kg}{s}\, 4.186\frac{J}{g°C}\, 10\,°C$$

$$\frac{dE}{dt} = -43.83 \; kW$$

With this rate of energy loss, how quickly will a 100 gallon tank cool?

$$Q_{cap} = M c_p \Delta T$$

$$Q_{cap} = 100 \; gal \; \left(4.186 \frac{J}{g\,^\circ C}\right) 1\,^\circ C = 1.582 \; MJ$$

$$t = \frac{Q_{cap}}{\frac{dE}{dt}} = \frac{1.582 \; MJ}{43.83 \; kW} = 36.1 \; s$$

At a velocity of .27 m/s, it will take a 100 gallon tank about 36 seconds to lose 1 °C. A similar calculation for a velocity of 0.08 m/s results in the tank losing 1 °C in 2 minutes and 15 seconds. Therefore, it will be impossible to maintain these operating conditions for an extended period of time, and a revision of the operating conditions is necessary.

With an 1800 W heater, what is the maximum flow rate that can be used while maintaining the temperature in the tank?

$$\frac{dE}{dt} = 0 = 1800 \; W + \dot{m}_{in} c_p T_{in} - \dot{m}_{out} c_p T_{out}$$

$$1800 \; W = \dot{m} * 4.186 \frac{J}{g\,^\circ C} \; 10 \,^\circ C$$

$$\dot{m} = .043 \; \frac{kg}{s}$$

With this flow rate, what tube size should be used to ensure that the flow is turbulent? For

internal flow, the turbulent region begins at a Reynold's number of 2300.

$$2300 = \frac{997.1 \frac{kg}{m^3} \, D \, v}{\mu}$$

$$.043 \, \frac{kg}{s} = 4 \left(\pi \left(\frac{D}{2} \right)^2 \right) \left(997.1 \frac{kg}{s} \right) (v)$$

$$D = 7.46 \, mm$$

$$v = .247 \, \frac{m}{s}$$

With this mass flow rate, how long will it take to fill a 50 gallon tank (most likely tank size to be used)?

$$50 \, gal \left(997.1 \frac{kg}{m^3} \right) = 189.45 \, kg$$

$$t = \frac{189.45 \, kg}{.043 \, \frac{kg}{s}} = 73.4 \, min$$

Therefore, it is likely that the water entering the tank will be in the tank for about 73 minutes before it is re-injected into the loop. A calculation to determine if the water will be 35 °C when it enters the loop again is required, but is extremely complex and would required use of Computational Flow Dynamics. Therefore, the lumped mass assumption will be made for the entire mass of water that is inserted into the tank over one minute. This is a model of the system where all of the water injected into the tank over the course of one minute stays clumped together in a sphere. The calculation of the time required to raise the mass in temperature will be a maximum time required to heat the water.

$$\frac{Mc_p}{hA_s} \ln \frac{T_i - T_\infty}{T(t) - T_\infty} = t$$

The total mass of the lumped mass is calculated below.

$$M = 60 \ s * 0.043 \ \frac{kg}{s} = 2.58 \ kg$$

The surface area is calculated below.

$$2.58 \ kg \frac{1m^3}{997.1 \ kg} = 0.0026 \ m^3$$

$$0.0026 \ m^3 = \frac{4}{3} \pi R^3$$

$$A_s = 4\pi R^2 = .091 \ m^2$$

The convective heat transfer coefficient will be calculated only considering natural circulation. All properties are considered for water at 1 atmosphere and 35 °C.

$$Nu = 2 + \frac{0.589(Ra)^{\frac{1}{4}}}{\left[1 + \frac{0.469^{\frac{9}{16}}}{Pr}\right]^{\frac{4}{9}}}$$

$$Ra = \frac{g\beta(T_\infty - T_s)x^3}{\nu\alpha} = \frac{9.81 \ \frac{m}{s^2}\left(361 * 10^{-6}\frac{1}{°C}\right)(35°C - 25°C)0.0852 \ m^3}{7.24 * 10^{-7}\frac{m^2}{s} 1.47 * 10^{-7}\frac{m^2}{s}} = 2.1 * 10^8$$

$$Pr = \frac{(7.2 * 10^{-4} Pa * s)\left(4186 \frac{J}{kg°C}\right)}{0.6107 \frac{W}{m^2°C}}$$

$$Nu = 63.8$$

$$h = \frac{63.8\left(0.6107 \frac{W}{m°C}\right)}{0.1704\, m} = 228.82\ \frac{W}{m^2°C}$$

Therefore, the time for the water to rise to 34 °C can be calculated (with this analysis 35 °C cannot be calculated).

$$t = \frac{2.58\, kg \left(4186 \frac{J}{kg°C}\right)}{228.82 \frac{W}{m^2°C}(.091\, m^2)}\, ln\left[\frac{-10}{-1}\right] = 19.9\, min$$

Since the lumped capacitance yields a time of heating that is far below the estimated time for the water to pass through the reservoir, it is acceptable to assume that the reservoir is large enough to allow sufficient time for the water to rise to the appropriate temperature.

Conclusion: A 1/4" pipe will need to be used instead of a 1" pipe to provide turbulent flow with an 1800 W heater. With a 1/4" pipe the mass flow rate will be 0.037 kg/s to provide a velocity of 0.29 m/s which makes the time the water in the reservoir about 85 minutes. However, a 1/4" pipe will make creating the surface difficult. Therefore, the number of samples needs to be decreased or the heater size needs to be increased to make the experiment practical.

Heat Exchanger Calculation

The goal of this calculation is to determine the dimensions of the heat exchanger needed to produce the desired output temperature that is required. The main dimensions in question are the diameter of the outside pipe, the length of the heat exchanger, and the mass flow rate of the cooling liquid.

Given: Inlet temperature of the brine is 35 °C, outlet temperature of the brine is 25 °C, the mass flow rate of the brine is 0.01 kg/s, diameter of the inside pipe is 1/4", and the inlet temperature of the cooling water is 10 °C

Assumptions: I assume negligible losses to the environment, negligible wall thermal resistance, no fouling, pipe is a thin shell, and constant properties

The most efficient manner in which to determine the optimum dimensions is to guess a diameter and flow rate, and calculate the necessary length of the heat exchanger. Then the diameter and flow rate can be varied to determine the shortest possible length to conserve material. The method that will be used involves using the log mean temperature difference in the following equations.

$$q = UA\Delta T_{lm}$$

$$U = \frac{1}{\frac{1}{h_i} + \frac{1}{h_o}}$$

$$\Delta T_{lm} = \frac{(T_{h,i} - T_{c,o}) - (T_{h,o} - T_{c,i})}{ln\left[\frac{T_{h,i} - T_{c,o}}{T_{h,o} - T_{c,i}}\right]}$$

The use of this method requires the characterization of the flow parameters on both sides of the heat exchanger. Since the parameters involved with the brine loop are given, the characterization of the inside flow will be done first. Properties for the water were taken at 30 °C and 1.2 atmospheres, the average temperature in the channel.

$$q = 0.01 \frac{kg}{s}\left(4186 \frac{J}{kg°C}\right) 10 °C = 418.6 \, W$$

$$Re = 2300 = \frac{997.1 \frac{kg}{m^3} \, (6.35 \, mm) \, 0.29 \frac{m}{s}}{7.977 * 10^{-4} Pa * s}$$

$$Pr = \frac{\mu c_p}{k} = \frac{7.977 * 10^{-4} Pa * s \left(4186 \frac{J}{kg \, °C}\right)}{0.603 \frac{W}{m \, °C}} = 5.54$$

The following two equations technically only apply to flow above a Reynold's number of 3000, but since the flow is turbulent it is assumed the equations will still apply (Incropera, p. 532).

$$f = (0.790 \, ln(2300) - 1.64)^{-2} = 0.05$$

$$Nu = \frac{\left(\frac{f}{8}\right)(Re - 1000)Pr}{1 + 12.7 \left(\frac{f}{8}\right)^{\frac{1}{2}} \left(Pr^{\frac{2}{3}} - 1\right)} = 14.35$$

Therefore, the convective heat transfer coefficient for the flow of the brine can be calculated.

$$h_i = \frac{Nu \, k}{D} = \frac{14.35 * 0.603 \frac{W}{m \, °C}}{6.35 \, mm} = 1363 \, \frac{W}{m^2 °C}$$

The calculation for the outside flow in the heat exchanger is tricky, and will require multiple attempts to provide optimization. Therefore, the calculations below will be for a 1" pipe and a flow rate of 0.1 kg/s (1.6 gal/min).

$$418.6 \, W = 0.1 \frac{kg}{s} \left(4186 \frac{J}{kg°C}\right) (T_{c,o} - 10 \, °C)$$

$$T_{c,o} = 11 \, °C$$

Therefore, all water properties will be taken at 1.1 atmospheres and 10.5 °C. The hydraulic diameter in this case is the outside pipe diameter minus the inside pipe diameter.

$$Re = \frac{4\dot{m}_c}{\pi D \mu} = \frac{4\left(0.1\frac{kg}{s}\right)}{\pi(0.03175m)\ 1.29 * 10^{-3}Pa * s} = 3108.7$$

$$Pr = \frac{1.29 * 10^{-3}Pa * s\left(4186\frac{J}{kg°C}\right)}{0.568\ \frac{W}{m°C}} = 9.51$$

These Reynold's and Prandtl numbers are within the values needed to use the following equations.

$$f = (0.790\ ln(3108.7) - 1.64)^{-2} = 0.045$$

$$Nu = \frac{\left(\frac{f}{8}\right)(Re - 1000)Pr}{1 + 12.7\left(\frac{f}{8}\right)^{\frac{1}{2}}\left(Pr^{\frac{2}{3}} - 1\right)} = 26.14$$

Therefore, the convective heat transfer coefficient can be calculated.

$$h_o = \frac{Nu\ k}{D} = \frac{26.14\left(0.568\ \frac{W}{m\ °C}\right)}{0.01905\ m} = 779.4\ \frac{W}{m^2°C}$$

Thus, the length of the heat exchanger can be calculated by the following progression.

$$\Delta T_{lm} = \frac{(35\ °C - 11\ °C) - (25\ °C - 10\ °C)}{ln\left[\frac{35\ °C - 11\ °C}{25\ °C - 10\ °C}\right]} = 19.15\ °C$$

$$U = \frac{1}{\dfrac{1}{1363 \frac{W}{m^2 \,^\circ C}} + \dfrac{1}{779.4 \frac{W}{m^2 \,^\circ C}}} = 495.9 \frac{W}{m^2 \,^\circ C}$$

$$L = \frac{q}{U\pi D_i \Delta T_{lm}} = \frac{418.6 \, W}{\left(495.9 \frac{W}{m^2 \,^\circ C}\right) \pi \, (0.00635 m)(19.15 \,^\circ C)} = 2.21 \, m$$

The procedure performed above was calculated multiple times to determine the best configuration. Given that the flow rate can vary from 0 kg/s to 0.11 kg/s (translates to 7/4 gal/min), and the diameter can be 1/4" and up, it was concluded that smaller diameters and higher flow rates result in shorter heat exchanger lengths. However, the pipe cannot be too small, and the thickness of the inner pipe must be taken into account.

Conclusion: Therefore, from this analysis it is recommended that a diameter of ½" be chosen to operate with a 0.1 kg/s flow rate which is just under the maximum flow rate. This translates to a heat exchanger length of 1.52 m. This calculation will have to be adjusted after a pipe thickness is chosen. It should also be noted that heat transfer is not an exact science, and margins for error will have to be considered.

AbsorptanceCalculator.m File

```
% Alexander Rehn
% Nanoengineered Surfaces for Improvements in Renewable Energy Systems
% 3/30/2011
% Determines absorptivities from Reflectance Data

% Variables              Purpose
% ---------              -------
% absorptance_data       A matrix that contains the absorptivity values
%                        versus wavelength for each sample.
% solar_spectrum_data    A matrix containing the energy per wavelength in the
%                        solar spectrum
% energy_summation       Adds up the energy per wavelength in
%                        solar_spectrum_data and relates it to the
%                        wavelengths given in absorptance_data
% energy_absorbed        Contains the energy absorbed by each sample per
%                        wavelength.
% alpha_617              The absorptivity of the oxidized Inconel 617 sample.
% alpha_Pt               The absorptivity of the oxidized Platinum layer on
%                        the Inconel 617 sample.
% alpha_Pt_Ni            The absorptivity of the oxidized Platinum and Nickel
%                        layers on Inconel 617 sample.
% alpha_N                The absorptivity of the oxidized Nickel sample.
% alpha_SiC              The absorptivity of the Silicon Carbide sample.

clc;
clear;


% Importing Data
[absorptance_data]=xlsread('Reflectance Data','Absorptance','A3:F724');
[solar_spectrum_data]=xlsread('Reflectance Data','Solar
Spectrum','A3:D2004');
[BB_emissivity_data]=xlsread('Reflectance Data','Emittance','B3:E724');


% Matrix Setup
energy_summation=zeros(722,1);
energy_absorbed=zeros(722,5);
energy_emitted_617=zeros(722,4);
energy_emitted_617_Pt=zeros(722,4);
energy_emitted_617_Pt_Ni=zeros(722,4);
energy_emitted_N=zeros(722,4);
energy_emitted_SiC=zeros(722,4);
emittance_results=zeros(5,4);


%% Absorptivity

% Calculation of incident energy per wavelength
for i=9:722
    for j=2:2002
        if solar_spectrum_data(j,1)>absorptance_data(i,1)
            energy_summation(i,1)=solar_spectrum_data(j-1,4)-...
```

```
                    sum(energy_summation(1:(i-1),1));
                break;
            end
        end
    end

    % Calculation of energy absorbed per wavelength
    for k=2:6
        for l=2:722
            energy_absorbed(l,k-1)=absorptance_data(l,k)*energy_summation(l,1);
        end
    end

    % Calculation of absorptivities
    alpha_617=sum(energy_absorbed(:,1))/899.56;
    alpha_617_Pt=sum(energy_absorbed(:,2))/899.56;
    alpha_617_Pt_Ni=sum(energy_absorbed(:,3))/899.56;
    alpha_N=sum(energy_absorbed(:,4))/899.56;
    alpha_SiC=sum(energy_absorbed(:,5))/899.56;

    %% Emissivity

    % Energy Absorbed per wavelength
    for m=2:6
        for n=1:4
            for p=2:722
                if m==2

    energy_emitted_617(p,n)=BB_emissivity_data(p,n)*absorptance_data(p,m)*(absorp
    tance_data(p,1)-absorptance_data(p-1,1));
                elseif m==3

    energy_emitted_617_Pt(p,n)=BB_emissivity_data(p,n)*absorptance_data(p,m)*(abs
    orptance_data(p,1)-absorptance_data(p-1,1));
                elseif m==4

    energy_emitted_617_Pt_Ni(p,n)=BB_emissivity_data(p,n)*absorptance_data(p,m)*(
    absorptance_data(p,1)-absorptance_data(p-1,1));
                elseif m==5

    energy_emitted_N(p,n)=BB_emissivity_data(p,n)*absorptance_data(p,m)*(absorpta
    nce_data(p,1)-absorptance_data(p-1,1));
                elseif m==6

    energy_emitted_SiC(p,n)=BB_emissivity_data(p,n)*absorptance_data(p,m)*(absorp
    tance_data(p,1)-absorptance_data(p-1,1));
                end
            end
        end
    end

    % Tallying Energy Absorbed
    for r=1:4
        emittance_results(1,r)=sum(energy_emitted_617(:,r));
```

```
        emittance_results(2,r)=sum(energy_emitted_617_Pt(:,r));
        emittance_results(3,r)=sum(energy_emitted_617_Pt_Ni(:,r));
        emittance_results(4,r)=sum(energy_emitted_N(:,r));
        emittance_results(5,r)=sum(energy_emitted_SiC(:,r));
end

emittance_results(:,1)=emittance_results(:,1)/15224.2;  %1445866.635;
emittance_results(:,2)=emittance_results(:,2)/22822.1;  %2374496.362;
emittance_results(:,3)=emittance_results(:,3)/32915.3;  %3665098.592;
emittance_results(:,4)=emittance_results(:,4)/45990.6;  %5380716.49;
```

Daily Data Sheet

Date _____

Time _____

Tank Thermocouple (K type) _____ ℃

Pre-heat Exchanger Thermocouple (T type) _____ ℃

Post-heat Exchanger Thermocouple (T type) _____ ℃

Sample 1 Inlet Thermocouple (T type) _____ ℃

Sample 2 Inlet Thermocouple (T type) _____ ℃

Sample 3 Inlet Thermocouple (T type) _____ ℃

Sample 4 Inlet Thermocouple (T type) _____ ℃

Sample 1 Outlet Thermocouple (T type) _____ ℃

Sample 2 Outlet Thermocouple (T type) _____ ℃

Sample 3 Outlet Thermocouple (T type) _____ ℃

Sample 4 Outlet Thermocouple (T type) _____ ℃

Sample 4 Rotameter _____ gpm

Sample 3 Rotameter _____ gpm

Sample 2 Rotameter _____ gpm

Sample 1 Rotameter _____ gpm

Chilled Water Rotameter _____ gpm

Sparging Rotameter _____ scfh

Sample 1 Pressure Drop Gauge _____ mm H20

Sample 2 Pressure Drop Gauge _____ mm H20

Sample 3 Pressure Drop Gauge _____ mm H20

Sample 4 Pressure Drop Gauge _____ mm H20

Sample 1 Inlet Pressure Gauge _____ **psi**

Water in tank (approx.) _____ **gal**

H_2S Cylinder Pressure (High/Low) _____ **psi**

Compare cylinder pressure with previous day (check mark) _____

Acquire and label 8 oz sample (check mark) _____

H_2S concentration _____ **ppm**

pH _____ **(5.5 to 7 acceptable range)**

H_2S sparging* (Y/N) _____

Fume hood/exhaust working? (Y/N) _____

Water on the floor? (Y/N) _____

Smell of sulfur? (Y/N) _____

Product Data Sheets

Silcolloy 1000

Silcolloy™

US Patent 7,070,833

Anti-corrosion, anti-oxidation and increased material lifetime

Silcolloy™1000 formerly Silcosteel®-CR

Silcolloy™ improves corrosion resistance of stainless steel by up to 10x!

Economical protection against corrosion

Silcolloy 1000 is highly effective protection for equipment exposed to:
- hydrochloric or nitric
- marine environments

Silcolloy 1000 treatment extends the lifetime of steel and steel alloy systems. High temperature capability and leak-free sealing capibility make it an ideal treatment for:
- process tubing, fittings, valves, and reactors
- gas transfer and delivery systems
- nozzles
- stack gas monitors
- analytical testing equipment in harsh environments

Methods available to control industrial corrosion are limited to corrosion-resistant alloys, barrier coatings, cathodic protection, and corrosion inhibitors. When properly applied, each method can be effective in slowing corrosion, but each has limitations as well. For example, some coatings are inexpensive, but require rigorous inspection and/or frequent reapplication. Corrosion-resistant alloys can provide exceptional protection, but can be prohibitively expensive. Some alloys require significant process redesign, increase operating cost, or generate hazardous waste.

Silcolloy™1000 is a proprietary (U.S. Patent #7,070,833), multilayer silicon, chemical vapor-deposited (CVD) coating, specifically designed to improve the corrosion resistance of steel, stainless steel, alloys, glass, and ceramics. The unique non line-of-sight CVD process produces a flexible amorphous silicon layer that diffuses into the metal lattice. The layer will conform to the most intricate surface while maintaining high dimensional tolerances. Silcolloy™1000 will deform with tubing surfaces, allowing leak-free seals or radius bends.

Independent Laboratory Testing
Silcolloy™1000 offers an order of magnitude or more improvement in corrosion resistance relative to existing processes.

Corrosion testing of Silcolloy™1000 treated 316L stainless steel and untreated 316L steel according to ASTM G 48, Method B2 (72-hour ferric chloride pitting and crevice corrosion testing), shows corrosion of the treated stainless steel is reduced by an order of magnitude, as measured by weight loss (Figures 1 and 2).[1]

SilcoTek.

112 Benner Circle | Bellefonte, PA 16823
814-353-1778 | Fax 814-353-1697
www.SilcoTek.com

Figure 1 Silcolloy™1000 treated stainless steel outperforms uncoated metal by an order of magnitude (ASTM G 48, Method B). Testing courtesy of Matco Associates.

weight loss in grams per square meter
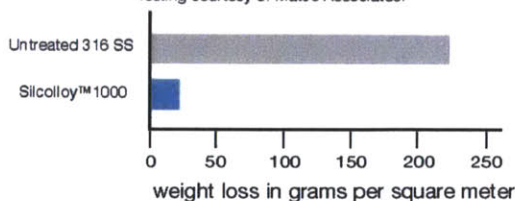
Testing of Silcolloy™1000 treated coupons in neutral, acidic, and basic chloride solutions, according to ASTM G 61,[1] shows Silcolloy™1000 treatment reduces corrosion rates by an impressive 50x, compared to untreated 316L stainless steel.

Figure 2 Silcolloy™1000 treated 316L stainless steel coupons show no crevice corrosion and only slight pitting corrosion; untreated coupons exhibit severe crevice corrosion. Testing courtesy of Matco Associates.

Silcolloy™1000 treated   untreated
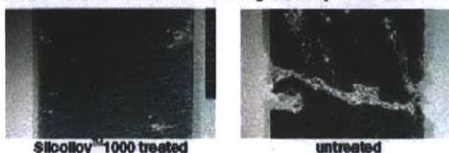
Improved Performance in Marine or Acidic Environments

Silcolloy™1000 treatment is effective in acidic or salt corrosive environments, in which the user demands extended service life for an existing process without using high-priced alloys. 4000-hour salt spray testing (salt spray accelerated weathering test ASTM B117) shows Silcolloy™1000 treated stainless steel coupons exhibit no surface corrosion, while untreated coupons show surface corrosion and accelerated corrosion at the coupon hole (Figure 4). Neither coupons developed pitting over the test period.[1]

Figure 4 Comparison of estimated lifetime costs in a typical process system, shows Silcolloy™1000 treatment can reduce the overall lifetime cost of the system by hundreds of thousands of dollars.

Silcolloy1000™ treated
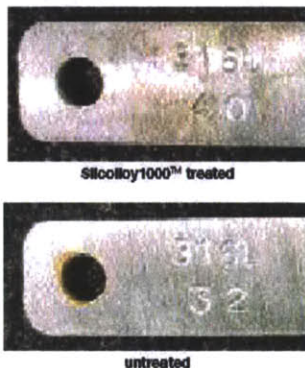
untreated

Save Thousands with Silcolloy!

Estimated lifetime cost savings of a typical process system show Silcolloy™ treated sample lines, fittings and valves will save the user hundreds of thousands of dollars. While the initial cost of an unprotected stainless steel system is lower than a comparable Silcolloy™1000 treated system, the overall lifetime cost, considering replacement cost due to corrosion is nearly double that of a Silcolloy™1000 treated system (see figure 5). Conversely, high performance alloy systems offer superlative corrosion performance, but the initial material cost can be up to six times higher than a comparable stainless steel system.

Figure 5 Silcolloy™1000 demonstrates significant cost savings, compared to untreated stainless steel or alloys (US dollars).
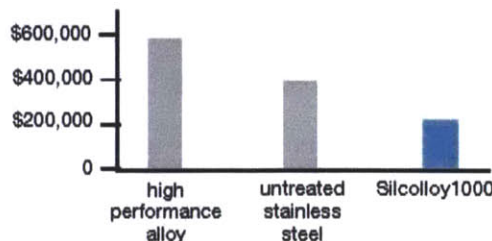
Summary

Silcolloy™1000 treatment has extended the life of process systems in oil and gas production, oil refining, petrochemical processing, aerospace equipment, food and beverage processing, and laboratory testing facilities worldwide.

Test data show that Silcolloy™1000 treatment is effective in extending the corrosion resistance of stainless steel process systems while reducing overall system maintenance cost. Because Silcolloy™1000 treatment can be applied to a majority of existing process components, process equipment life is extended without significant re-engineering.

References
1. M. Zamanzadeh; G. Bayer; G. Rhodes; D. Smith; M. Higgins; Laboratory Corrosion Testing of a Chemical Vapor Deposited Amorphous Silicon Coating; Matco Associates, Inc. Pittsburgh, PA; SilcoTek Corporation, Bellefonte, PA. 2005

112 Benner Circle | Bellefonte, PA 16823
814-353-1778 | Fax 814-353-1697
www.SilcoTek.com

Dursan

Dursan™ COATING GUIDE

PHYSICAL PROPERTIES	Dursan™	SilcoNert 2000™ (Sulfinert®)	304 Stainless Steel	
Temperature range	-210C to +450C	-210C to +450C	Per tool	
Pressure range	Limited by tool	Limited by tool	Per tool	
Minimum Coating Thickness (nm)	500	120	N/A	
Wear resistance (x10-5mm3/N m)	6.13	14.00	13.81	
Relative wear resistance vs. stainless steel	2.25	0.99	1.00	
Lubricity (coefficient of friction)	0.378	0.7	0.589	
Relative lubricity vs. stainless steel	1.56	0.84	1.00	
Ductility, flexibility	Good, flexible with steel	Good, flexible with steel	Per tool	
Durability/recommended cycles	x cycles	1 cycle	N/A	
Hydrophobicity/moisture resistance (contact angle)	104	80	36	
Relative moisture resistance vs. stainless steel	2.89	2.22	1.00	

CHEMICAL INERTNESS PROPERTIES

	Dursan™	SilcoNert 2000™ (Sulfinert®)	304 Stainless Steel	
H2S/ Sulfur and sulfur compounds (50ppm H2S, 30 day recovery)	97%	95%	0%	
Mercury and mercury compounds	Excellent	Excellent	Poor	
Ammonia	Excellent	Good	Poor	
Arsenic	Excellent	Good	Poor	
Allowable pH exposure	0-14	0-8	Weak acid-14	
Acid Exposure (50ppm MSH 12 day stability)	85%	85%	0	
Base Exposure (50ppm MSH 12 day stability)	95%	0	0	
Restricted chemical exposure	HF	Bases, HF, Sulfuric	Per tool	
Corrosion resistance ASTM G31, 6M HCl 22C, mils per year	1.86	16.31	389	
Corrosion improvement factor vs. stainless steel	209.80 (Treated)	23.90	1.00 (Un-treated)	

SilcoTek™
Driving Innovation

Curran 1000

Product Properties: Tube ID Coating

Advanced two part (100% solids) epoxy coating designed specifically for high temperature immersion service in cooling water and process streams this coating is an organic/inorganic hybrid that exhibits state of the art coating technology with exponential improvements in performance verses existing polymer technology. Can withstand multiple cycling and steam out events subjected to process equipment. Ideally suited for small diameter tubes:

- Heat exchanger tubes
- Condenser tubes
- Chiller tubes

Benefits:

- Outstanding immersion protection in water and hydrocarbons.
- Can withstand multiples of heat cycling events with no effect.
- Tolerates steam outs to + 430 F (221 C).
- Excellent foul release.
- Reduction in drag
- Coating surface remains slippery even at high temperatures.
- High Gloss finish
- More thermally stable at higher temperatures than other coatings.
- Excellent cold wall resistance (100C for 30 days)
- Zero VOC'S (100% Solids)

Technical data:

Color: White/Grey

Weight (lbs/ gal) 12.8

Volume solids: 100%

Flash Point > 200 F (93 C)

Properties

The following tests were performed on samples after full cure (96 hours @ 70F).

Abrasion Resistance: ASTM D 6040

Tabor CS-17 wheel 1000 cycles

107 mg loss

Atlas Cell Exposure (cold wall): ASTM C 868

Atlas cell exposure at 100C for 30 days. Passed

Cathodic Disbondment: ASTM G 8

Zero millimeter disbondment at 100C for 30 days.

Chemical resistant:

Contact   Curran   for   specific chemicals/temperatures/concentrations.

Recommended for: Steam, hydrocarbons, acids and caustics

Hardness Barcol: (ASTM D 2583)

50

Shore D Hardness: (ASTM D 2240)

85

Pull off Adhesion: ASTM D 4541

>3,800 PSI to substrate, superficial cohesive failure at 3,300 PSI

Temperature resistance:

Tested up to 400 F (204 C) in steam.

Contact Curran on particular service conditions.

Theoretical coverage:

Based on 1 mil (25.4 microns)

1 Gallon will cover 1604 ft² (150 m²)

* Allow a wastage factor based on application method

Mix Ratios:

- Mixing Ratio by Weight (Base : Hardener) 100 grams to 24.53 grams
- Mixing Ratio by Volume (Base : Hardener) 4:1

Dry time: To Touch 2 hours Mechanical 4 hours

Application:

Below are general guidelines for applying Curran 100 T-ID. Contact Curran International for detailed application procedures.

Surface preparation:

- SSPC- SP 10 is a minimum surface cleanliness
- Surface roughness: 1.0 Mil minimum.

- New surfaces should be degreased prior to grit blasting
- Coating should be applied immediately after surface preparation

Coating Application:

- Coating must be fully mixed before addition of solvent
- Minimum 60:1 airless spray pump
- Recommended Thickness 7- 12 mils in a single coat

Environmental:

Apply when substrate temperature is between 60 F and 100 F. Substrate must be 5 F above dew point

Thinning:

- Thinning: Acetone or MEK can be utilized for thinning and clean up. No more that 25 % of either solvent can be added to the coating. Coating must be fully mixed before addition of solvent

Holiday Inspection:

Wet sponge testing is recommended with 66 VDC

Repairs:

Should coating be mechanically damaged or a holiday is detected take the following steps to perform a repair.

1) Wash area with soap and water
2) Abrade area with grit blasting or mechanical abrasion.
3) Allow to dry and Qc

Working Times:

Will vary depending on temperature. At 70F

(21C) the usable life of mixed material is 60 min.

Storage/Shelf Life:

Store in temperatures between 50F (10C) and 90F (32C)

Separate base and hardener will have a shelf life for 2 years when in original, unopened container that is not damaged and stored at the above temperature ranges.

Health and Safety:

Prior to using this product please review the appropriate Material Safety Data Sheet (MSDS).

Note: Full cure should be confirmed by a Barcol Hardness test or a MEK rub before exposing coating to chemical service.

Cure Time:

	50F/10 C	60F/16 C	70F/21 C	90F/32 C
Tack Free	12 hrs	10 hrs	8 hrs	4 hrs
Light load	24 hrs	20 hrs	16 hrs	8 hrs
Overcoat	24 hrs	18 hrs	12 hrs	1 hr
Full Load	60 hrs	40 hrs	32 hrs	16 hrs
Full Chem	154 hrs	120 hrs	64 hrs	32 hrs

Diffusivity Data

Shot Number	Curran 1000		Curran 1000 with self healing		Curran 1000 with nano graphene		Curran 1000 with nano graphene and nano silicon carbide		Curran 1000 with PTFE		Curralon with PTFE	
	Temperature (°C)	Diffusivity (mm^2/s)	Temperature (°C)	Diffusivity (mm^2/s)	Temperature (°C)	Diffusivity (mm^2/s)	Temperature (°C)	Diffusivity (mm^2/s)	Temperature (°C)	Diffusivity (mm^2/s)	Temperature (°C)	Diffusivity (mm^2/s)
1	24.9	6.01	25.4	15.234	25	10.191	25.1	12.175	25.2	3.246	24.8	4.656
2	24.7	6.267	25.1	14.04	25.3	10	24.9	11.073	24.9	2.447	25.2	4.363
3	24.8	6.454	24.9	14.825	24.9	10.69	25	11.698	24.7	3.687	25	3.83
4	25.1	5.823	25.4	13.786	24.8	10.22	25.1	12.431	25.2	3.18	24.8	4.789
5	24.8	5.897	25	15	25.2	10.588	24.7	12.544	25	4.258	25.2	4.328
mean	24.9	6.09	25.2	14.577	25	10.338	25	11.984	25	3.364	25	4.393
st. dev.	0.2	0.264	0.2	0.63	0.2	0.29	0.2	0.604	0.2	0.669	0.2	0.37
6	29.7	5.709	29.7	13.452	30.1	8.126	29.6	12.75	30	2.273	30	2.368
7	30.4	5.889	29.8	14.241	29.8	10.613	30.1	12.204	29.7	1.968	30.4	2.423
8	29.9	5.577	30.4	12.854	29.8	10.63	30.2	11.665	30	2.234	29.9	2.907
9	29.7	5.651	29.8	13.476	30.4	10.151	29.8	11.775	30.4	2.092	29.7	2.679
10	30.4	5.663	29.7	14.067	29.8	10.046	29.8	11.893	29.8	2.348	30.4	2.642
mean	30	5.698	29.9	13.618	30	9.913	29.9	12.057	30	2.183	30.1	2.604
st. dev.	0.4	0.117	0.3	0.553	0.3	1.033	0.2	0.436	0.3	0.152	0.3	0.216
11	35.1	5.415	35.1	13.643	34.7	10.073	35.1	0.397	35.3	0.621	35.2	0.725
12	35.2	5.778	35.3	13.568	35.2	9.467	34.7	0.785	34.9	0.64	35.3	0.696
13	34.7	5.801	34.8	13.313	35.1	9.478	35.2	0.658	34.8	0.827	34.8	1.323
14	35.3	5.515	35	13.067	34.7	9.766	35.2	238.189	35.3	0.702	35.1	0.935
15	35.1	5.85	35.3	12.378	35.2	10.128	34.7	0.604	34.8	2.616	35.3	95.155
mean	35.1	5.672	35.1	13.194	35	9.782	35	48.127	35	1.081	35.1	19.767
st. dev.	0.2	0.194	0.2	0.509	0.3	0.315	0.3	106.248	0.3	0.862	0.2	42.144

Abrasion Resistance Data

Taber Abrasion Resistance Data		
Sample	ID	Weight Loss (mg)
Carbon Steel	Sample A	60
	Sample B	51.9
Curran 1000	Sample A	46.2
	Sample B	45.3
Curran 1000 with self healing	Sample A	63.5
	Sample B	58.1
Curran 1000 with nanographene	Sample A	55.1
	Sample B	58.7
Curran 1000 with nanographene and nanosilicon carbide	Sample A	93.5
	Sample B	47.9
Curran 1000 with PTFE	Sample A	49.3
	Sample B	77
Curralon with PTFE	Sample A	38.9
	Sample B	43.2

Daily Data

Starting of loop-Validation

Date	8/9/2011	8/10/2011	8/11/2011	8/12/2011	8/15/2011	8/15/2011	8/16/2011	8/17/2011
Time	3:30 PM	1:56 PM	11:34 AM	12:25 PM	12:27 PM	3:21 PM	11:40 AM	2:36 PM
Tank Thermocouple (°C)	34.4	33.5	36.6	34.4	34.8	36.8	37	36
Pre-heat Exchanger Thermocouple (°C)	34	33.3	36.6	33.9	34.6	36.7	36.6	35.2
Post-heat Exchanger Thermocouple (°C)	24.9	23.9	25.2	23.6	22	22.3	27.1	29.8
Sample 1 Inlet Thermocouple (°C)								
Sample 2 Inlet Thermocouple (°C)								
Sample 3 Inlet Thermocouple (°C)								
Sample 4 Inlet Thermocouple (°C)								
Sample 1 Outlet Thermocouple (°C)								
Sample 2 Outlet Thermocouple (°C)								
Sample 3 Outlet Thermocouple (°C)								
Sample 4 Outlet Thermocouple (°C)								
Sample 4 Rotameter (gpm)	0.15	0.13	0.12	0.13	0.1	0.15	0.2	0.36
Sample 3 Rotameter (gpm)	0.15	0.12	0.13	0.12	0.09	0.15	0.14	0.3
Sample 2 Rotameter (gpm)	0.15	0.09	0.12	0.1	0.08	0.15	0.19	0.25
Sample 1 Rotameter (gpm)	0.14	0.12	0.15	0.1	0.08	0.15	0.2	0.4
Chilled Water Rotameter (gpm)	<1	<1	<1	<1	<1	<1	<1	<1
Sparging Rotameter (scfh)	-	-	-	-	-	-	-	-
Gas Exit Rotameter (scfh)								
Sample 1 Pressure Drop Gauge (in H20)								
Sample 2 Pressure Drop Gauge (in H20)								
Sample 3 Pressure Drop Gauge (in H20)								
Sample 4 Pressure Drop Gauge (in H20)								
Sample 1 Inlet Pressure Gauge (psig)								
Water in tank (gal)	43	43	43	43	43	43	43	42
H2S High Cylinder Pressure (psi)	0	0	0	0	0	0	0	1620
Pressure change	N/A	0	0	0	0	0	0	1620
H2S Low Cylinder Pressure (psi)	0	0	0	0	0	0	0	3
Pressure change	N/A	0	0	0	0	0	0	3
8 oz sample aquired (Y/N)	Y	Y	Y	Y	Y	Y	Y	Y
H2S concentration (approx. ppm)	0.2	0.24	0.11	0.27	<0.02	0.15	0.69	0.36
pH (5.5-7)	6.52	6.61	6.50	6.45	6.48	6.45	6.21	6.48
H2S sparging (Y/N)	N	N	N	N	N	N	N	Y
Fume hood/exhaust working? (Y/N)	Y	Y	Y	Y	Y	Y	Y	Y
Water on floor? (Y/N)	N	N	N	N	N	N	N	N
Smell of sulfur? (Y/N)	N	N	N	N	N	N	N	N
Ammonium added (mL)								

8/18/2011	8/18/2011	8/19/2011	8/23/2011	8/25/2011	8/26/2011	8/26/2011	8/26/2011	8/29/2011	8/31/2011	9/1/2011	9/2/2011
10:32 AM	3:22 PM	10:00 AM	1:20 PM	1:00 PM	6:15AM	7:40 AM	10:00 AM	7:00 AM	12:32 PM	12:30 PM	10:35 AM
36.6	34.3	34.8	33.8	33.7	33.1	not taken	not taken	34.4	36.5	35	37
36.2	33.7	34.5	33.3	34.2	33.2	not taken	not taken	34.9	36.1	20.7	36.5
30.5	28	26.8	24.9	25.5	25.7	not taken	not taken	27	28.3	20.5	28.9
			.								
0.37	0.3	0.16	0.18	0.18	0.16	0.16	0.28	0.28	0.2	0	0.22
0.27	0.36	0.35	0.15	0.18	0.16	0.18	0.24	0.22	0.2	0	0.21
0.18	0.28	0.08	0.2	0.2	0.19	0.2	0.2	0.16	0.22	0	0.13
0.42	0.18	0.09	0.2	0.18	0.14	0.14	0.24	0.18	0.18	0	0.21
<1	<1	<1	<1	<1	<1	not taken	not taken	<1	<1	<1	<1
-	3	<2	-	-	4	-	not taken	4	<1	0	<1
42	42	42	42	42	42		not taken	42	42	42	42
1600	1450	1250	1190	1000	990	900	not taken	900	855	845	825
-20	-150	-200	-60	-190	-10	-90	not taken	0	-45	-10	-20
3	5	3	3.9	3.9	6.1	4.2	not taken	8	6	6	6
0	2	-2	0.9	0	2.2	-1.9	not taken	3.8	-2	0	0
Y	Y	Y	Y	Y	N	N	not taken	Y	Y	Y	Y
0.3	1.11	1.1	0.37	0.41	not taken	not taken	0.75	0.26	0.27	0.25	0.25
6.08	5.95	6.05	6.39	7.01	not taken	not taken	5.96	5.9	5.93	6.08	6.04
Y	Y	Y	Y	y	y	Y	not taken	Y	Y	Y	Y
Y	Y	Y	Y	y	y	Y	not taken	Y	Y	Y	Y
N	N	N	N	n	n	N	not taken	N	N	N	N
N	N	N	N	n	n	N	not taken	N	N	N	N

9/5/2011	9/6/2011	9/8/2011	9/9/2011	9/16/2011	9/21/2011	9/23/2011		11/29/2011	11/30/2011	12/1/2011
10:38 AM	10:50 AM	10:10 AM	3:45 PM	2:28 PM	2:41 PM	1:15 PM		5:26 PM	12:08 PM	11:54 AM
33.6	33.3	35.3	36.7	36.5	34	36.6		34	34.8	42
33.1	33.1	35	36.6	36	33.9	36.3		40.9	35.6	41.8
25.5	25.2	25.3	27.3	26.7	24.9	27.2		27	29.9	35
								41.8	37.7	43.8
								40.5	37.5	42
								40.1	34	43.2
								40.7	34.5	43.6
								31.7	31.4	34.6
								31.9	32.2	36
								32.3	30.7	32.6
								34.5	31.6	32.1
0.2	0.19	0.18	0.18	0.16	0.16	0.17		0.19	0.19	0.18
0.18	0.17	0.16	0.15	0.15	0.13	0.13		0.2	0.15	0.13
0.08	0.2	0.21	0.2	0.2	0.2	0.2		0.19	0.19	0.2
0.18	0.17	0.16	0.16	0.16	0.16	0.16		0.21	0.19	0.2
<1	<1	1	<1	<1	<1	<1		<1	<1	<1
<1	<1	<1	<1	<1	<1	<1		<2	<2	<2
								16.5	17	19
								8	11	11
								11.5	8	4
								0	1	<0
								<1	<1	<1
42	42	42	42	41	41	41		44	44	44
800	800	750	750	750	750	725		675	375	250
-25	0	-50	0	0	0	-25		-	-300	-125
6	6	7	6	6	6	6		3	5	8
0	0	1	-1	0	0	0		-	2	3
Y	Y	Y	Y	Y	Y	Y		Y	Y	Y
0.25	0	0.02	0.01	0.05	0.05	0.05		0.159	0.4452	0.1378
6.09	5.95	5.72	5.72	6.05	6.17	5.83		6.19	6.72	6.1
Y	Y	Y	Y	Y	Y	Y		Y	Y	Y
Y	Y	Y	Y	Y	Y	Y		Y	Y	Y
N	N	N	N	N	N	N		N	N	N
N	N	N	N	N	N	N		N	N	N

173

12/7/2011	12/8/2011	12/9/2011	12/12/2011	12/13/2011	12/14/2011	12/15/2011	12/22/2011	12/26/2011	1/5/2012	1/6/2012
7:50 PM	12:15 PM	3:15 PM	3:42 PM	11:24 AM	6:19 PM	3:13 PM	3:33 PM	3:30 PM	12:47 PM	4:21 PM
33.4	30.4	30.8	32.5	32.6	32.4	31.6	34.2		33.6	35
32.9	30	29.8	32.1	30.7	31.8	31.4	33.7		32.1	34.6
26.2	25	25.5	25.9	24.4	25.8	24.3	25.7		25.9	26.1
34.4	31.5	31.6	33.6	32.4	33.4	33.1	35		33.4	35.6
32.8	29.8	29.9	32	30.8	31.7	31.2	33.3		31.8	34
32.8	29.9	29.8	31.9	31.1	31.6	31.3	33.5		32.1	34.1
32.7	29.8	29.8	31.9	31	31.7	31.1	33.2		31.7	34
26	24.6	25.3	25.6	25	25.8	24.1	26.3		26	25.7
25.8	24.6	25.3	25.3	24.8	25.6	23.3	25.6		25.3	25.6
25.9	24.5	25.2	24.8	24.1	24.7	23.3	25.5		25	25.2
27.8	26.3	27.1	26.9	26.4	27	25.8	27		27	27.5
0.23	0.23	0.23	0.22	0.22	0.21	0.2	0.2	0.17	0.19	0.2
0.19	0.18	0.18	0.18	0.17	0.17	0.16	0.2	0.16	0.16	0.17
0.2	0.2	0.2	0.2	0.2	0.2	0.15	0.2	0.17	0.17	0.22
0.18	0.18	0.18	0.18	0.18	0.18	0.16	0.2	0.18	0.17	0.19
<1	<1	<1	<1	<1	<1	<1	<1		<1	<1
<2	<2	<2	<2	<2	<2	<2	<2		<2	<2
19	16	16	16	16.5	17	14	22		20	16
6	9	9	9	9	9	1	8		3	3
16	14	13	14	15	16	13	>30		>30	>30
6	9.5	11	21	24	30	25	>30		>30	>30
<1	<1	<1	<1	<1	<1	<1	<1		<1	<1
43	43	43	43	43	43	43	43		43	42
2000*	2000	1975	1900	1900	1875	1700	950	0	0	0
-	-	-25	-75	0	-25	-175	-750		-950	0
4	4	4	4	4	4	5	8	3	0	0
-4	0	0	0	0	0	1	3		-8	0
Y	Y	Y	Y	Y	Y	Y	Y		Y	Y
0.159	0.212	0.212	0.265	0.265	0.265	1.325	0.08		0	0
5.98	5.96	5.94	5.76	5.55	5.62	5.4	4.6		4.64	4.67
Y	Y	Y	Y	Y	Y	Y	Y		N	N
Y	Y	Y	Y	Y	Y	Y	Y		Y	Y
N	N	N	N	N	N	N	N		N	N
N	N	N	N	N	N	N	N		N	N

Restart of
loop-Trial #2

1/9/2012	1/10/2012		1/27/2012	1/28/2012	1/29/2012	1/30/2012	1/31/2012	2/1/2012	2/2/2012	2/3/2012	2/6/2012
11:55 AM	12:48 PM		3:30 PM	3:34 PM	4:38 PM	12:40 PM	11:10 AM	1:50 PM	1:40 PM	12:50 PM	12:53 PM
35.7	33.7			35.8	32	31.8	33.5	32.7	31.8	34.5	32.7
34.7	33.1			34.3	32	31.5	33	31.1	31.5	32.7	32.5
27.1	25.8			28.3	25.3	25.4	26.6	25.5	25.7	26.6	26.7
35.5	33.3			34.1	31.4	31.4	32.6	30.7	31.4	32.2	32.2
34	32.4			33.9	30.7	31.6	32.2	27.8	24.5	24.1	23.6
34.1	32.5			34.2	31.6	31.5	32.7	30.8	31.3	32.5	32.3
34.1	32.5			34.1	31.3	31.5	32.7	30.8	31.5	32.3	32.3
26.9	25.5			27.4	23.7	24.1	25.1	24.2	24.8	26	26.4
26.9	25.6			27.4	21.1	24.7	24	14	24.2	23.7	21.6
26.3	24.8			30.7	27.7	27.2	28.3	27	26.8	27.7	27.2
28.7	27			28.3	24.7	25.3	26.2	25.1	25.4	26.3	27
0.2	0.19			0.2	0.15	0.18	0.18	0.16	0.18	0.18	0.22
0.17	0.17			0.19	0.18	0.17	0.16	0.16	0.15	0.15	0.14
0.22	0.22			0.22	0.1	0.14	0.1	<.1	<.1	<.1	<.1
0.19	0.18			0.2	0.14	0.17	0.16	0.15	0.18	0.18	0.2
<1	<1			0.65	0.75	0.8	0.75	0.65	0.75	0.75	0.65
<2	<2			<.4	<.4	-	0.15	0.125	0.125	0.15	0.15
				0.75	0.75	-	<.4	<.4	<.4	<.4	<.4
17	17			6	2	2	2	2	4	7	12
5	3			13	>30	>30	>30	>30	>30	>30	>30
>30	>30			>30	>30	>30	>30	>30	23	22	22
>30	>30			9	5	5	7	3	3	1	16
<1	<1			-	-	-	-	-	-	-	1.61
42	42			44	44	44	44	44	44	44	44
0	0		2025	2000	1950	1950	1925	1925	1900	1850	1750
0	0			-25	-50	0	-25	0	-25	-50	-100
0	0		10	8	8	30	6	6	6	6	8
0	0			-2	0	22	-24	0	0	0	2
Y	Y			Y	Y	Y	Y	Y	Y	Y	Y
0	0			1.59	5.3	0.5	1.6	1.6	1.4	0.5	1.7
4.66	4.75			5.74	5.02	5	4.65	4.52	4.9	5.3	4.85
Y	Y			Y	Y	Y	Y	Y	Y	Y	Y
Y	Y			Y	Y	Y	Y	Y	Y	Y	Y
N	N			N	N	N	N	N	N	N	N
N	N			N	N	N	N	N	N	N	N

2/7/2012	2/8/2012	2/9/2012	2/10/2012	2/13/2012	2/14/2012	2/15/2012	2/16/2012	2/17/2012	2/20/2012	2/21/2012
1:00 PM	12:30 PM	3:30 PM	3:30 PM	2:05 PM	5:40 PM	6:00 PM	5:43 PM	4:35 PM	7:41 PM	5:25 PM
32.6	32.8	33.6	33.6	35	32.3	37.4	34.4	33.5	33.6	34.8
32.2	31.8	31.6	32.5	34.7	32	38.4	31.4	33.1	32.6	34.2
24.3	24.5	24.9	24.2	25.1	23.6	28.1	25.2	23.5	20.9	21.2
31.6	31.5	31.3	31.9	34.3	31.4	34.1	37.7	32.6	31.7	33.5
24.2	31.6	31.5	31.9	34.1	30.9	31.3	35.9	32.1	30	30.6
31.7	31.6	31.5	31.6	34.1	31.4	33.2	33.8	32.7	32	33.6
31.8	31.3	31.5	31.7	33.8	31.5	33	33.5	32.5	30.9	32.7
24.5	23.5	23.9	22.3	24.3	23.4	25.7	25.5	24	21.7	20.7
23.3	25.7	26.2	25.3	26.8	21.9	17.5	24.7	22.9	15.1	12.3
25.1	24.9	25.2	24.3	25.6	23.2	25.6	25.3	23.8	18.6	19.5
24.6	23.6	24.8	23.6	24.3	23.8	26	26	24.2	19.5	19.7
0.18	0.14	0.14	0.14	0.1	*	*	*	*	*	*
0.16	0.12	0.12	0.13	0.1	*	*	*	*	*	*
<.1	0.14	0.12	0.12	0.1	*	*	*	*	*	*
0.15	0.15	0.14	0.14	0.1	*	*	*	*	*	*
0.75	0.8	0.7	0.8	0.7	0.75	0.7	0.65	0.7	0.75	0.95
0.15	0.15	0.15	0.15	0.2	0.2	0.2	0.2	0.2	0.2	0.2
<.4	<.4	<.4	<.4	<.4	<.4	<.4	<.4	<.4	<.4	<.4
1	4	6	5	1	22	25	19	18	9	11
>30	18	26	30	>30	>30	>30	>30	>30	>30	>30
22	22	22	22	22	23	22	23	22	22	23
2	1	1	1	0	1	1	1	1	0	1
0.19	0.63	0.75	0.89	1.33	2.2	1.9	2.03	2	1.64	1.2
44	44	44	43	43	43	43	43	43	42	42
1700	1650	1600	1550	1400	1325	1300	1200	1150	925	850
-50	-50	-50	-50	-150	-75	-25	-100	-50	-225	-75
8	9	9	9	10	10	10	10	10	11	12
0	1	0	0	0	0	0	0	0	1	1
Y	Y	Y	Y	Y	Y	Y	Y	Y	Y	Y
2.014	1.325	1.325	1.325	0.795	**	**	**	**	**	**
4.83	5.09	5.14	5.45	5.17	6.2	5.75	5.37	5.45	5.33	5.25
N	Y	Y	Y	Y	N	N	N	N	N	N
Y	Y	Y	Y	Y	Y	Y	Y	Y	Y	Y
N	N	N	N	N	N	N	N	N	N	N
N	N	N	N	N	N	N	N	N	N	N

3/2/2012	3/4/2012	3/5/2012	3/6/2012	3/7/2012	3/8/2012	3/9/2012	3/12/2012	3/13/2012	3/14/2012	3/15/2012	3/16/2012
12:45 PM	8:34 AM	1:20 PM	1:00 PM	12:20 PM	12:00 PM	9:20 PM	1:45 PM	1:15 PM	7:12 PM	2:10 PM	2:15 PM
	34.2	32.9	32.8	33.9	34.8	33.2	33.7	31.5	31.6	33.2	33.6
	33.7	32.5	32.5	33.7	34.6	32.2	33.4	31.1	31.5	33	33.3
	28.5	26.7	27.2	27.6	27.7	26.6	23.6	25.3	24.1	24.4	24.1
	33.4	32	32	33.2	34.1	32.4	32.8	31	30.8	31.9	32
	33.6	32.1	32	33.3	33.9	32.3	32.9	31.2	31.2	32.2	32.8
	33.7	32.2	32	33.4	34.1	32.2	32.9	31.5	31.4	32.4	32.9
	33.5	31.9	31.9	33.3	33.8	32.4	32.7	31.3	31.1	32.1	32.7
	27.7	27.3	26.8	26.4	29.2	27.5	26.2	25.5	23.7	23.2	22.1
	27.3	24.4	*	*	28	26.6	23.2	26.9	23	22.2	21.3
	33.5	31.7	30	32.2	26.9	27.1	20.9	25.2	24.2	23	23
	26.4	25.8	25.3	25.5	26.6	27.2	23.1	25.3	24.1	24.1	24.2
	0.22	0.21	0.2	0.19	0.22	0.21	0.11	0.23	0.15	0.11	0.14
	0.24	0.23	0.22	0.2	0.23	0.2	0.1	0.24	0.16	0.12	0.14
	0.23	0.22	0.2	0.19	0.24	0.2	0.11	0.28	0.16	0.14	0.15
	0.21	0.18	0.16	0.14	0.18	0.15	0.1	0.12	<.1	<.1	<.1
	0.8	0.7	0.7	0.75	0.7	0.7	0.75	0.7	0.65	0.6	0.7
0.2	0.1	0.1	0.1	0.1	0.1	0.1	0.1	0.1	0.1	0.1	0.1
0	<.4	<.4	<.4	<.4	<.4	<.4	<.4	<.4	<.4	<.4	<.4
	>30	>30	>30	>30	>30	>30	>30	>50	>50	45	33
	22	22	22	22	22	23	22	22	22	22	22
	22	22	23	22	22	22	22	22	22	22	22
	21	19	16	15	21	20	15	22	8	3	4
	2.04	2.05	2.07	1.98	5.75	6.17	3.6	6.1	2.7	1.9	1.75
40	40	40	40	40	40	39	39	39	39	39	39
725	725	675	650	600	575	550	450	425	400	375	325
-	0	-50	-25	-50	-25	-25	-100	-25	-25	-25	-50
6	6	6	6	6	6	6	7	7	8	8	8
-	0	0	0	0	0	0	1	0	1	0	0
	Y	Y	Y	Y	Y	Y	Y	Y	Y	Y	Y
	1.272	1.325	1.378	1.378	1.325	1.272	1.696	1.908	1.908	2	2
	5.14	5.02	5.14	4.62	4.8	4.81	4.4	4.4	4.45	4.2	4.35
N	N	N	N	Y	N	Y	N	N	Y	N	N
Y	Y	Y	Y	Y	Y	Y	Y	Y	Y	Y	Y
N	N	N	N	N	N	N	N	N	N	N	N
N	N	N	N	N	N	N	N	N	N	N	N

3/19/2012	3/20/2012	3/21/2012	3/22/2012	3/23/2012	3/28/2012	4/2/2012		4/13/2012	4/16/2012	4/17/2012	4/18/2012
3:45 PM		6:00 PM	4:30 PM	12:10 PM	2:30 PM	2:13 PM		.	5:45 PM	3:05 PM	4:15 PM
34.5		35.7	32.7	34.3	32.3	33.7			32.6	33.3	34
33.4		33.1	32	31.5	32.3	33.5			32.4	33.1	34.3
24		21.6	20.7	20	17.8	23			31.9	30.4	29.2
32.1		30.6	30.4	29.9	23	32.5			32.3	32.2	34.1
33		31.1	31.1	30.8	22.1	30.7			32.3	32.3	34.2
33.2		32.6	31.3	31.3	30.3	30.7			32.3	33.2	34.3
33		32.5	31.2	30.9	31.1	32.6			32.3	33.2	34.1
23		17	15.2	13	18.5	24.8			32	22.3	26
24		16.9	22.8	17.7	19.6	13.3			32.1	21.4	26.3
24.9		23.4	18.7	13.5	13.4	12.7			32.3	32.9	34
25		23.7	21.1	21.3	19.8	24.5			32.3	33.1	34.1
0.16	<.1	0.11	0.11	0.11	<.1	0.3		0.32	0.32	0.31	0.31
0.18	<.1	0.12	0.11	0.11	<.1	0.34		0.33	0.32	0.31	0.3
0.13	<.1	<.1	<.1	<.1	<.1	0.36		0.17	0.14	0.14	0.19
<.1	<.1	<.1	<.1	<.1	<.1	0.38		0.18	0.15	0.14	0.19
0.65		0.6	0.8	0.75	0.78	0.6			0	0.75	0.4
0.1		0.1	0	0	0.1	0.1			0.1	0.1	0.1
<.4		<.4	<.4	<.4	<.4	<.4			<.4	0.4	<.4
48		12	11	7	0	>50			19	14	15
22		22	22	22	22	22			22	22	22
22		22	22	22	22	22			22	22	22
8		3	3	3	2.5	15			28	28	27
1.7		0.7	1.05	1	0.83	6.4			0.9	0.75	0.95
38		38	38	38	38	38			44	43	43
200		125	100	<100	2050	1850			1725	1700	1650
-125		-75	-25	-	-	-200			-	-25	-50
8		10	4	1	10	10			8	10	6
0		2	-6	-3	-	0			-	2	-4
Y		Y	Y	Y	Y	Y			Y	Y	Y
1.75		1.8	1.5	0	1.5	1.3			1.75	1.75	0.75
4.3		4.43	4.8	4.55	4.5	4.4			4.17	4.1	3.8
N		N	N	N	Y	N			Y	Y	Y
Y		Y	Y	Y	Y	Y			Y	Y	Y
N		N	N	N	N	N			N	N	N
N		N	N	N	N	N			N	N	N

4/19/2012	4/20/2012	4/23/2012	4/24/2012	4/25/2012	4/26/2012	4/27/2012	4/30/2012	5/1/2012	5/2/2012	5/3/2012	5/4/2012
1:45 PM	5:00 PM	3:10 PM	1:15 PM	3:05 PM	2:10 PM	4:05 PM	2:30 PM	2:20 PM	2:30 PM	2:30 PM	1:00 PM
31.7	33.9	31.6	35.2	32	32.1	32.7	32.4	32.1	33.3	35.4	35.4
31.6	33.6	31.6	34.7	32.1	32.2	32.9	32.4	32	33.2	34.6	35.1
27.5	27.5	27.7	30.9	28.5	27.5	27.1	27.4	25	23.1	25.2	24.3
31.4	33.2	31.4	34	31.7	31.9	32.6	32	31.4	32.6	34	34.4
31.4	33.2	31.3	34.2	31.7	31.9	32.2	32	31.4	32.6	33.9	34.4
31.5	33.6	31.5	34.6	31.9	31.9	31.3	21	21	21	20.9	20.5
31.5	33.5	31.5	34.6	31.7	32	32.7	32	20.7	20.6	20.4	20.4
23.2	25.4	22.6	26	24.3	24.7	24.5	26.4	25.3	25.5	26.3	26.1
23.4	25.8	22.7	26.7	24	24.6	23.7	26.2	25.3	24.8	25.8	25.1
31.3	33.1	31.4	34.1	31.6	31.4	21.2	20.8	21	21	20.4	20.5
31.3	33.1	31.5	34.2	31.5	31.6	32	31.5	21	20.9	20.4	20.5
0.31	0.31	0.31	0.34	0.35	0.4	0.31	0.27	<.1	<.1	<.1	<.1
0.3	0.3	0.29	0.32	0.32	0.25	<.1	<.1	<.1	<.1	<.1	<.1
0.19	0.18	0.16	0.19	0.18	0.2	0.18	0.22	0.22	0.23	0.24	0.23
0.19	0.18	0.15	0.19	0.19	0.21	0.19	0.28	0.23	0.25	0.27	0.27
0.55	0.4	0.5	0.4	0.4	0.4	0.35	0.4	0.4	0.4	0.4	0.35
<.1	<.1	0.1	0.1	0.1	0.15	0.2	0.1	<.1	0.1	0.15	0.15
<.4	<.4	<.4	<.4	<.4	<.4	<.4	<.4	<.4	<.4	<.4	<.4
15	15	12	15	15	16	13	38	29	26	26	25
22	22	22	22	22	22	22	22	22	22	22	22
22	22	22	22	22	22	22	22	22	22	22	22
27	27	27	28	28	30	28	26	8	9	10	9
0.92	0.85	0.47	1.05	0.9	1.24	0.96	2.3	2.15	1.85	1.89	1.85
43	43	43	42	42	42	42	42	42	42	42	42
1650	1625	1525	1500	1450	1400	1350	1200	1200	1150	1100	1050
0	-25	-100	-25	-50	-50	-50	-150	0	-50	-50	-50
6	5	4	5	5	5	5	6	6	6	6	6
0	-1	-1	1	0	0	0	1	0	0	0	0
Y	Y	Y	Y	Y	Y	Y	Y	Y	Y	Y	Y
1.3	1.3	2.1	1.75	1.9	2.1	2.2	1.75	1.75	1.4	1.8	2
3.9	4.18	3.7	3.7	3.9	3.9	4.15	4.4	4.47	4.8	4.09	3.9
Y	Y	Y	Y	Y	Y	Y	Y	Y	Y	Y	Y
Y	Y	Y	Y	Y	Y	Y	Y	Y	Y	Y	Y
N	N	N	N	N	N	N	N	N	N	N	N
N	N	N	N	N	N	N	N	N	N	N	N